Tritium Control and Mitigation in Fluoride-Salt-Cooled High-Temperature Reactors

by

Xiao Wu

A dissertation submitted in partial fulfillment
of the requirements for the degree of
Doctor of Philosophy
(Nuclear Engineering and Radiological Sciences)
in The University of Michigan
2019

Doctoral Committee:

Professor Xiaodong Sun, Chair
Professor Richard Christensen
Professor John Foster
Professor Kimberlee Kearfott
Professor Larson Ronald
Dr. Piyush Sabharwall

Xiao Wu

xwunuke@umich.edu

ORCID iD: 0000-0003-1620-6313

In memory of my grandfather.

ACKNOWLEDGMENTS

Throughout writing this dissertation and life in graduate school, I have received a great deal of support and assistance that I would cherish for my entire lifetime. I would like to express my deepest gratitude to my adviser, Prof. Xiaodong Sun. It is a great honor to be your student and work with you. Your guidance has made this a thoughtful and rewarding journey. Without your support and patience, this work would not have been possible.

I would also like to extend my most sincere appreciation to Prof. Richard Christensen, for your unparalleled expertise and consistent encouragement during the past six years. I am also deeply indebted to Dr. Piyush Sabharwall, for your valuable suggestions and help with my career.

I must thank my committee members, Prof. Kimberlee Kearfott, Prof. Ronald Larson, and Prof. John Foster, for your invaluable assistance in this work. Your extensive knowledge, insightful critique, and helpful advice are most valuable to me.

In addition, I would like to express my gratitude to my parents for your warm love and endless support. I would also like to thank my lab mates, Dave Arcilesi, Minghui Chen, Chacha Lin, Qingqing Liu, Yang Liu, Qiuping Lv, Shanbin Shi, Chengqi Wang, Sheng Zhang, and Xiaoqing Zhang, for all the discussions we had and courses we completed together. Special thanks to my friends, Jinzhu Chen, Liwei Chen, Xu Kang, Jessica Lee, Xiaoyue Liu, Yigong Ma, Xun Sun, Yaxian Wang, Mouzhe Xie, and Wei Zhu. Thank you for accompanying me in adventures, pushing me through hard ascents, and feeding me with hot pots.

TABLE OF CONTENTS

LIST OF FIGURES

LIST OF TABLES

LIST OF APPENDICES

NOMENCLATURE

A	surface area, m^2
a_V	total surface area of bubbles in a unit volume, m^{-1}
C_b	fixed cost, USD
$C_{capital}$	capital cost, USD
C_E	energy cost, USD
$C_{operating}$	operating cost, USD
C_{total}	total cost, USD
c	concentration, mol/m^3
D	hydrogen gas diffusivity, m^2/s
D_i	partial variance of y^M
D_{ij}	partial variance of y^M
D_{var}	total variance of y^M
d	diameter
d_h	hydraulic diameter
F_d	fabrication cost factor
F_m	material cost factor
F_p	pressure cost factor
F_y	estimated time factor
G	molar flow flux of gas phase, $mol/(m^2\text{-}s)$
H	height, m
H_{eff}	effective release height, m
H_{mt}	Henry's constant, $mol/m^3\text{-}Pa$
$H_{operation}$	number of operation hours per year
H_s	release point height, m
h	mass transfer coefficient, m/s

h_{tower}	height of the countercurrent extraction tower, m
h_G	height equivalent to the theoretical plate of gas-phase, m
h_L	height equivalent to the theoretical plate of liquid-phase, m
K	hydrogen gas solubility, mol/m^3-Pa (nonmetal), mol/m^3-Pa$^{0.5}$ (metal)
K_{mt}	Sievert's constant, mol/m^3-Pa (nonmetal), mol/m^3-Pa$^{0.5}$ (metal)
$K_{partition}$	partition factor
k_G	diffusion coefficient, m/s
L	molar flow flux of liquid phase, mol/(m^2-s)
$\dot{m}$	mass flow rate, kg/s
P	pumping power, W
p	partial pressure, Pa
Q	mass transfer rate, mol/s
Q_p	mass of puff released, Bq
Q'	radiation release rate, Bq/s
R	reaction rate, mol/m^3-s
Re	Reynolds number
R_g	ideal gas constant, J/mol-K
r	radial position, m
Sc	Schmidt number
Sh	Sherwood number
S_i	first-order Sobol indix
S_{ij}	second-order Sobol indix
T	temperature, K
t	time, s
U	wind speed, m/s
$\bar{u}$	mean wind speed, m/s
V	volume, m^3
x	distance position, m
y	crosswind position, m
y^M	prediction
z	height position, m

Greek symbols

η	pump efficiency
θ_i	i^{th} sector
θ_w	sector width
μ	fluid viscosity, Pa-s
ρ	density, kg/m^3
σ	neutron cross section, barn
σ_y	horizontal dispersion coefficient, m
σ_z	vertical dispersion coefficient, m
σ_r	radial dispersion coefficient, assumed equal to σ_y, m
Φ	hydrogen gas permeability, mol/m-Pa-s (nonmetal), mol/m-$Pa^{0.5}$-s (metal)
χ	radiation concentration, Bq/m^3

Subscripts

1	primary side or upstream side
2	secondary side or downstream side
avg	average
b	bulk
CO_2	carbon dioxide
H	hydrogen
in	inlet
N_2	nitrogen
o	overall
out	outlet
p	puff
T_2	tritium
th	thermal neutron related
w	wall

Vectors and matrices

$\mathbf{q}$	vector of length p, each element represents an input variable
$\mathbf{q}^*$	new set of input parameters
$\mathbf{h}(\mathbf{q})$	basis function
$\boldsymbol{\beta}$	regression coefficients vector
$\hat{\boldsymbol{\beta}}$	regression coefficients estimator
$\mathbf{H}$	basis function matrix
$\mathbf{K}$	basis function matrix

ABSTRACT

Fluoride-salt-cooled high-temperature reactors (FHRs) receive wide attention because of their advantageous passive safety features and potential high thermal efficiency in power generation when compared with current commercial nuclear reactors. However, tritium generation and release are potentially significant challenges of FHRs, and tritium in the reactor need to be carefully handled and managed. This dissertation proposes a potential solution for tritium management in FHRs.

In this study, meteorological models were built to perform tritium-dispersion analyses and to evaluate the potential health impact of chronic airborne tritium release on the public and the contributions of meteorological parameters to the dose assessment, which are rarely investigated. Key meteorological and geometric parameters in favor of reducing the impact on the public were then identified. Uncertainty analysis and sensitivity study were performed for the dose assessment of three potential FHR construction sites, and daily tritium release limits were calculated.

The tritium-dispersion analyses indicated that the release of tritium to the environment must be controlled and limited in FHRs. A tritium control and mitigation system was designed both to reduce the tritium release rate from FHRs and potentially to eliminate an intermediate loop in the pre-conceptual design of the advanced high-temperature reactor (AHTR) as well as other FHR designs. The proposed system consists of four major components: redox control, a cross-flow tritium removal facility, an optional double-wall intermediate heat exchanger (IHX), and tritium-permeation-barrier coating on structural materials as necessary. Comparisons of different tritium control strategies from an economic assessment show that the proposed two-loop FHR design with the tritium control and mitigation system exhibits economic advantages over the original three-loop AHTR design.

To verify the performance of the proposed tritium control and mitigation system, a tritium transport-analysis model was developed. A novel method involving the logarithmic mean square root of partial pressure difference (LMSPD) was developed to calculate mass transfer in complex geometries and flow configurations. The method was implemented in MATLAB and validated using data from a hydrogen-permeation experiment available in the literature. The obtained calculation results agree reasonably well with the experimental data—especially in the temperature range of interest to this study.

To further validate the LMSPD code and the cross-flow configuration of the tritium removal facility, laboratory-scale experiments were designed using hydrogen as a surrogate for molecular tritium (T_2). A hydrogen-removal experiment was carried out using the reactor off-gas krypton as the carrier gas for H_2. The obtained experimental data confirm the effectiveness of the cross-flow tritium-removal design, and the code calculation results validate the LMSPD method.

In summary, the results and conclusions of this study provide significant insights for tritium management in FHRs. The atmospheric-dispersion modeling of airborne tritium identifies the major influencing factors on public dose assessment and the corresponding measures needed to help reduce health impacts. This study also contributes to future research on tritium control strategies. A cross-flow tritium removal facility was designed as the key component of a tritium-mitigation strategy. A novel LMSPD model was developed and validated for tritium extraction in the cross-flow configuration. The model can be used for future mass transfer calculations in complex geometries and flow configurations. In addition, hydrogen-removal experiments were designed to evaluate the efficiency of the cross-flow tritium removal facility, which, if carried out in a molten salt environment, will serve as valuable data for the FHR community.

Chapter 1. Introduction

The fluoride-salt-cooled high-temperature reactor (FHR) is a reactor concept that combines the advantages of the sodium fast reactor and the high-temperature gas-cooled reactor (HTGR) [1]. It has been attracting wide attention as a Generation IV reactor concept. FHR uses the graphite-matrix coated-particle fuels proposed for HTGRs and a direct reactor auxiliary cooling system (DRACS) for passive decay heat removal. The primary coolant is generally FLiBe (a mixture of LiF with highly enriched ^{7}Li and BeF_2) with a melting point of 459 °C and a boiling point of 1433 °C. FLiBe has a specific heat capacity of 2.34 kJ/(kg-K) and a thermal conductivity of 1.0 W/(m-K) at 600 °C [2]. These property values are comparable to 5.5 kJ/(kg-K) and 0.56 W/(m-K), respectively, for saturated water at 7.5 MPa. The FLiBe density (1,940 kg/m^3) is much higher than the density of water (732 kg/m^3) at 7.5 MPa (at saturation). Because of the significantly lower operating pressure (near the atmospheric pressure) and advantageous primary coolant characteristics (high density and good thermal characteristics) in FHRs, a significant reduction in reactor size and cost could be achieved compared with HTGRs and water-cooled reactors at a similar electricity output.

However, among all the advantages in FHRs, there are still several technical challenges to be addressed, one of which is tritium generation. It has been estimated that the tritium generation rate can be up to 185 TBq/day, or 518 mg/day at startup in an FHR with a rated thermal power of 2,400 MWth [3]. Given such a large tritium generation rate, it is necessary to investigate tritium transport in an FHR system, dispersion in the environment, potential health impact to the public due to inadvertent tritium release, and develop mitigation strategies to overcome tritium migration or permeation.

1.1 Background

1.1.1 Tritium generation and transport in FHRs

Tritium is of special interest among the fission products produced in FHRs. Because of the neutron activation of the FLiBe coolant, a considerable amount of tritium is produced. Lithium is a major source of tritium generation in the FHR core. Highly enriched lithium is used, so 99.995% lithium exists as ${}^{7}_{3}\mathrm{Li}$ [4]. Although the neutron absorption cross section of ${}^{7}_{3}\mathrm{Li}$, which is 20 mb, is only 1/47000 that of ${}^{6}_{3}\mathrm{Li}$, the total rate of neutron events is considerable due to the high content of lithium in the primary coolant [3]. In addition, the reaction between ${}^{7}_{4}\mathrm{Be}$ and neutron generates more ${}^{6}_{3}\mathrm{Li}$. The main tritium-producing reactions are as follows [5]:

$$ {}^{6}_{3}\mathrm{Li} + \mathrm{n} \rightarrow {}^{4}_{2}\mathrm{He} + {}^{3}_{1}\mathrm{H};\ \sigma_{th} = 940\ \mathrm{b}, \tag{1.1} $$

$$ {}^{7}_{3}\mathrm{Li} + \mathrm{n} \rightarrow {}^{4}_{2}\mathrm{He} + {}^{3}_{1}\mathrm{H} + \mathrm{n}';\ \sigma_{avg} = 20\ \mathrm{mb}, \tag{1.2} $$

$$ {}^{7}_{4}\mathrm{Be} + \mathrm{n} \rightarrow {}^{4}_{2}\mathrm{He} + {}^{6}_{3}\mathrm{Li};\ \sigma_{avg} = 36\ \mathrm{mb}, \tag{1.3} $$

$$ {}^{19}_{9}\mathrm{F} + \mathrm{n} \rightarrow {}^{17}_{8}\mathrm{O} + {}^{3}_{1}\mathrm{H};\ \sigma_{avg} = 30\ \mu\mathrm{b}, \tag{1.4} $$

where

σ represents the absorption cross section (b: barn) for the parent nuclide;

subscript th refers to thermal neutron energies;

and subscript avg refers to average neutron energies.

A comparison of the estimated tritium production rates of several nuclear-power reactor types can be found in Table 1.1 [6][7].

Table 1.1. Comparison of tritium production rates [6][7]

Reactor type	Tritium production rate [GBq/(GWth-day)]
Pressurized-water reactor	514.3
Boiling-water reactor	455.1
HTGR	684.5
Heavy-water reactor	43,512
FHR	107,781

In the natural redox condition of the primary coolant, FLiBe, the majority of tritium generated exists in the charge state T^+, and it has the tendency to combine with F^- to form TF molecules. It is estimated that more than 90% of the tritium generated in the core exists in the form of TF and that the remainder exists in the form of T_2 [8]. Because TF is corrosive to structural materials, especially at high temperatures, the generation of TF in the reactor core must be controlled or even eliminated [3].

To prevent or rather minimize corrosion to structural materials, it is necessary to adjust and maintain the reduction-oxidation (redox) condition of the coolants. A significant amount of research has been done in this area in the fusion community. The method used to maintain TF concentration at a sufficiently low level is redox control. One of the material used for the redox control is beryllium (Be), which acts as a redox agent and prevents TF from forming when dissolved physically in FLiBe [9], since the chemical bound between Be and F is much stronger than that between H and T. With the redox control, the major form of tritium in FHRs is T_2 dissolved in the primary coolant.

However, tritium in gaseous form (HT or T_2) has a considerable permeation rate through metal, especially under high operating temperatures of FHRs. The tritium produced in the primary loop, if left to accumulate, will have a very high permeation rate through the intermediate heat exchangers (IHXs) in FHRs. Through modeling of the tritium dispersion in the environment, it is found that public health may be impacted by the released tritium. For nuclear power plants to obtain operating license, the transport of emitted radioactive materials during normal operations

and under accidental events must be analyzed to demonstrate the impacts is within the regulation limits [10].

The anticipated difficulties in containing tritium justify the need of special care in FHR system design. A sound understanding of tritium generation, transport pathways, properties, and possible means to prevent it from escaping the reactor system should be an integral part of the containment design plan for FHRs. As a result, three-loop systems are currently being considered for FHRs to reduce tritium permeation to the power cycle and release to the environment. However, the intermediate loop represents additional construction and maintenance costs and therefore offsets the above-mentioned benefits of the FHRs. An alternative tritium-mitigation strategy that eliminates the necessity of the intermediate loop is therefore highly preferable.

T_2 physically dissolves in the primary coolant, FLiBe. Therefore, the mechanism of gas transport can be applied to tritium transport in FHR systems. The permeation rate of tritium through a solid material is determined by the tritium partial pressures on both sides of the material, the temperature of the material, the intrinsic properties of the material, the thickness of the material, and the solid surface condition. Permeability Φ is used to describe the ability of gas permeation through a solid, which is defined as the product of the diffusivity and solubility of the gas in the material, D and K, respectively, as:

$$\underset{\text{Permeability}}{\Phi} = \underset{\text{Diffusivity}}{D} \times \underset{\text{Solubility}}{K}. \tag{1.5}$$

The diffusivities and solubilities of hydrogen isotopes in the molten salts FLiBe and FLiNaK are listed in Table 1.2. The numerical values of the same transport coefficient of the same isotope are found to vary significantly among different research groups. Tritium permeability values in some common structural materials are also listed in Table 1.3. These values of the tritium transport coefficients are used in this study in tritium transport simulation and modeling and in the design of tritium removal and mitigation systems and facilities.

Table 1.2 Solubility values of tritium in molten salts from experiments

Gas species	Molten salt species	Solubility [mol/(m^3-Pa)]	Diffusivity [m^2/s]	References
T_2	FLiBe	$7.9\times10^{-2}\exp\left(-\frac{35000}{R_gT}\right)$	$9.3\times10^{-7}\exp\left(-\frac{42000}{R_gT}\right)$	[11]
H_2	FLiBe	1.13×10^{-3} (at 773 K) 3.17×10^{-3} (at 873 K) 3.87×10^{-3} (at 973 K)		[12]
D_2	FLiBe	3.1×10^{-4} (at 873 K) 1.0×10^{-4} (at 973 K)	8.0×10^{-10} (at 873 K) 3.0×10^{-9} (at 923 K)	[13]
H_2	FLiNaK	$3.98\times10^{-7}\exp\left(\frac{34400}{R_gT}\right)$	$8.69\times10^{-10}\exp\left(-\frac{50000}{R_gT}\right)$	[14]
H_2	FLiNaK	$7.06\times10^{-5}\exp\left(-\frac{54900}{R_gT}\right)$	$1.67\times10^{-7}\exp\left(-\frac{27000}{R_gT}\right)$	[15]

Table 1.3 Tritium permeability in structural materials [16]

Material	Permeability [mol/(m-s-Pa$^{0.5}$)]
Incoloy-800	2.4×10^{-10}–5.5×10^{-10}
Incoloy-600	6.6×10^{-10}
SS 304L	1.2×10^{-10}
Hastelloy N	4.2×10^{-10}
Nickel alloy	9.3×10^{-10}

1.1.2 Health impact of tritium

Tritium, as a weak beta emitter, can cause acute or chronic health issues if taken in by human beings via inhalation, food, or drink. Tritium released to the environment from an FHR mainly exists in the forms of HT, T_2, and HTO. The main release pathway of tritium from FHRs is airborne release, which occurs when HT, T_2, and HTO enter the atmosphere in the form of gas or water

vapor. In the process of entering the atmosphere and dispersing, HT and T_2 are highly likely to convert to HTO [17][18]. For example, tritium can undergo a beta-emission-induced reaction with oxygen or hydroxyl to form HTO or T_2O. The reaction rate is directly proportional to the concentration of tritium, as specified in the following [19]:

$$R = 1.19 \times 10^{-4} c_{T_2}, \tag{1.6}$$

where c_{T_2} is the T_2 concentration in the atmosphere. In addition to the spontaneous decay of tritium, HT and T_2 can transform to HTO at a relatively high rate in the presence of catalysts, such as metals and surfaces—especially when HT and T_2 reside on a surface for any length of time [17]. Soils and microorganisms in soils are also strong catalysts for conversion. Once in contact with soil, HT can be transformed to HTO in the top few centimeters of the soil at a high reaction rate [20].

HTO in the environment is of a higher concern than HT or T_2 because the dose factor of HTO is approximately three magnitudes higher than that of HT or T_2 on a per-unit-dose inhalation basis [21]. In addition, HTO has a greater probability to enter the hydrological cycle, thus resulting in a greater chance to enter living organisms [22]. However, this does not mean that HT and T_2 should be neglected in the evaluation of tritium health impact on the environment. Results from a previous study on tritium concentration in Fukuoka, Japan show that both tritiated water and tritium gases need to be considered when calculating the radiation effect on human beings [23]. On the other hand, comparing the two forms of tritiated water, HTO and T_2O, HTO still draws higher attention, because if HTO and T_2O are released at the same level of radioactivity, the amount of molecules of HTO would double that of T_2O, and hence HTO has the ability to disperse in a wider range.

In FHRs, the main form of tritium in the system will be T_2 due to the lack of oxygen or water in the system and the redox control in the coolants. However, once it permeates through the structure materials and enters the surrounding environment, gaseous tritium converts to HTO and the conversion rate of the process is difficult to determine [18][44]. Shortly after gaseous tritium is released to the atmosphere, the percentage of HT or T_2 converted to HTO can be anywhere up to 54% [17], and this percentage could keep increasing as the tritium disperses. Therefore, the

chemical form of the released tritium from FHRs is assumed to be a mixture of mainly gaseous tritium and tritiated water vapor. However, the ratio of these two forms is subject to change due to local conditions. In this study, for conservative considerations, tritium released from FHRs is assumed to be 100% HTO for conservative concerns.

1.1.3 Tritium release regulations in the U.S.

Because tritium in the environment can cause health issues for the public, the current regulations on tritium release, environmental topics, and radioactive materials are reviewed. This literature survey focuses on regulations and policies in the U.S. and Canada because of the extensive experience of these countries with tritium release from Canada deuterium uranium (CANDU) heavy water reactors.

ALARA, which stands for "as low as reasonably achievable," is the principle for minimizing the doses and releases of radioactive materials [24]. In addition, the U.S. Nuclear Regulation Commission has set the upper limit of radiation dose. For the general public not related to nuclear power plants, the effective dose limit is 10 mrem/y: namely, 1 mSv/y [25]. In addition, the federal government also regulates the maximum contaminant level (MCL) for tritium [26]. It is required that no more than 4 mrem/y, which equals 0.4 mSv/y, of dose equivalent should be absorbed from beta particles. This limit applies to a total body or to any internal organs. 10 CFR Part 50 [27] regulates the domestic licensing of production and the utilization of facilities, which includes nuclear power plants. According to this regulation, the dose equivalent limit of tritium for an individual is 7.5 mrem, which equals 0.75 mSv, per quarter and for any organ it is 15 mrem/y, which equals 1.5 mSv/y.

The members of the general public that live nearby an FHR power plant (within a 1-km radius) and use local drinking water and farm products will receive the highest effective dose equivalent from FHR tritium release [28]. This is because these people both breathe in gaseous tritium and take in tritium via consumption of water, plants, and animals, all of which could be potentially tritium contaminated and become tritium sources. We should pay most attention to these people when we set the tritium release limit for conservative purposes.

1.1.4 Research on the tritium release limit in Canada

Canada has the same radioactive release limit as the U.S. For a person who is not a nuclear-energy worker, the effective dose allowed is less than 1 mSv/y [29]. According to different meteorological conditions and the height of the stack from which tritium is released, the amount of tritium needed to reach the upper radioactive material limit (1 mSv) differs from one situation to another, as shown in Table 1.4.

Table 1.4 HTO Release Rate to Reach the Upper Radioactive-material-release Limit [40]

Stack height [m]	HTO release rate [TBq/day]	Meteorological condition	Reference
30	2.775	Under the most unfavorable meteorological conditions	[33]
30	7.4	Harmonic mean wind speed: 2 m/s; Frequency factor of the prevailing wind exceeds the mean wind speed: 2.5; Absolute humidity: 8.6 g/cm^3	[30]
60	37		
91.4 – 182.9	74	Not specified	[31]
100	44.4	Extremely unstable meteorological conditions; Mean wind speed: 1.3 m/s	[32]

Doury [33] has investigated the permissible level of tritium release. For gaseous tritium release, the oxidation rate of tritium is uncertain. Doury developed a model from laboratory data [34] to calculate the isotopic exchange rate. In the data used to develop the model, the tritium concentration in the air was 1.85–25.9 MBq/m^3. It is estimated that the oxidation rate of TH or T_2 to HTO is 0.2–3% per day. Because HTO has a higher tendency to be absorbed by human beings than HT or T_2, the release of gaseous tritium should be evaluated as the release of HTO, taking into consideration the tritium oxidation rate. Under the worst metrological conditions—which generally mean high humidity, minimum wind speed, low atmosphere temperature, and low

precipitation level—the maximum allowed tritium release rate is 2.775 TBq/day without exceeding the gaseous radioactive-release limit [33][40].

To understand better the effect of the gaseous tritium release rate on the annual-effective-dose equivalent received by the public, the case of Oak Ridge Reservation is reviewed. Blanco and Blomeke [35] estimate that, under the 37-GBq/s release rate of HTO from a 100-m high stack at Y-12 plant, the tritium concentration in the air at the ground level is 14.8 kBq/m^3. For the general public at the edge of Oak Ridge City, the tritium concentration in the air at ground level is 40.7 Bq/m^3. The exposure time of the workers and the public is 40 h/week and 168 h/week, respectively. The resulting annual dose equivalents for the workers and the general public are 0.4 and 0.7 mSv/y, respectively. Both values for the workers in the Y-12 plant and the general public are much lower than the annual limit of 10 mSv.

The stack height is another factor that influences the allowed maximum release rate of radioactive gases. It can be seen from the second and third rows in Table 1.4 that an increase in stack height from 30 to 60 m results in an increase of permissible release rate from 7.4 to 37 TBq/day. Therefore, if the stack height in Blanco's calculation [35] was 30 m instead of 100 m, the resulting annual dose equivalent for the public at the edge of the Oak Ridge City might be much higher than the current value.

For a pebble-bed advanced high-temperature reactor, the reactor building height is 35 m [36], which is close to 30 m. Because gaseous molecular tritium is much less dense than air, it is reasonable to assume that gaseous molecular tritium releases at the top of the reactor building. For instance, in the 3400-MWth AHTR, the tritium production rate is estimated to be 126.91 TBq/day [37]. Under this proposed 2.775 TBq/day tritium-release upper limit, 97.8% of the tritium produced will need to be removed, assuming the rest would be released to the environment.

The above-mentioned tritium release limit is proposed under the assumption that the tritium released is 100% HTO. In the actual operation of FHRs, tritium emission consists of a mixture of T_2 and HTO, as stated previously. Therefore, the tritium release limit could be considerably higher than the proposed 2.775 TBq/day. The key parameter to be determined is the percentage of HTO

in the tritium emission. A previous field study shows that the amount of HT converting to HTO is around 2.4%, with 0.5% uncertainty [38]. However, the report from Lawrence Livermore National Laboratory shows that the historically highest HTO concentration was 54% [17]. In general, the lower the HTO concentration in the tritium released, the higher the tritium release limit. In the case of a 2.9% concentration of HTO in the tritium released, the tritium release limit could be as high as 111 TBq/day instead of the proposed 2.775 TBq/day. Therefore, 2.775 TBq/day could serve as a lower bound for the tritium release rate limit for FHRs.

1.1.5 Previous studies on tritium-dispersion modeling in the environment

The dispersion of tritium depends largely on local topography and meteorology. Gaseous tritium may enter the soil, surface water, and groundwater via the hydrological cycle. Common physical factors that affect tritium transport in the environment include atmospheric temperature, pressure, relative humidity, wind, and the presence and size of the concentration gradient. In addition to these environmental factors, features of the facilities that release tritium also have an effect on tritium dispersion. These include the number and heights of the stacks, the gaseous tritium exit temperature, the velocity at which gaseous tritium is released, and the size and locations of surrounding buildings and local topography. In general, high temperature, high pressure, high turbulence, and low humidity favor tritium dispersion. Some of the above factors are shown in Figure 1.1 [39].

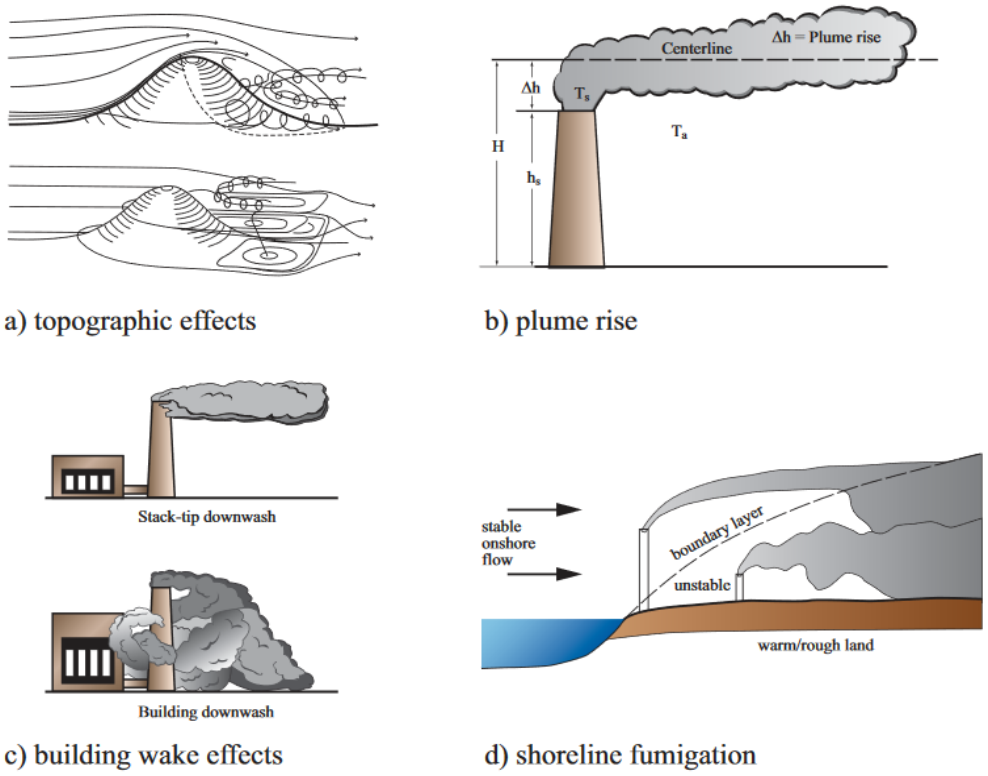

Figure 1.1 Factors that influence tritium dispersion [39]

Figure 1.1 (a) shows that, when the released tritium encounters a hill or other obstacle, it might go around it or up it first and then down the other side. Figure 1.1(b) indicates that the height of the release location of the radioactive material influences its dispersion. Figure 1.1(c) shows building wake effects. Aerodynamic effects of the stack itself and its surroundings could affect the dispersion pattern: i.e., whether the radioactive gases will rise upwards or go downwards around the stack. Figure 1.1(d) shows that, if the release location is on a shoreline, the radioactive gases tend to be drawn to the ground. However, the shoreline effect is short-termed; it does not have an influence over a long period of time.

The chemical form of tritium also affects the dispersion process. Compared with HTO, T_2 has a molecular weight that is about 1/3 of that of HTO. T_2 has the tendency to rise and leave the troposphere, while HTO is comparable to the surrounding air in molecular weight and has a longer residence time in the troposphere. T_2 released to the troposphere has a residence time of only a few

weeks and then resides in the stratosphere for months or even years. Although lateral mixing of T_2 in the troposphere could happen, the most significant concern of T_2 release to the troposphere is in the local areas of the release sites [40].

The dispersion of radioactive materials in the atmosphere and water has been widely studied for decades. Several investigations have been carried out on the dispersion of tritium generated from nuclear power plants or tritium production factories. Meneghetti et al. [41] modeled the tritium dispersion around the Angra dos Reis nuclear power plant and adopted a plane parallel boundary simplification. This technique helps to increase the accuracy of applying popular gas-dispersion models to mountainous or other complex orography.

The health impact caused by the radioactivity of tritium released has also been widely investigated. Matsuura et al. [42] and Fujita et al. [43] measured the environmental HTO levels in air and water and compared them to regulatory limits. The results confirm that the tritium levels to which the public is exposed are well within safe ranges. The Tritium Working Group from the IAEA Programme on Biosphere Modelling and Assessment (BIOMASS) modeled six scenarios to study long-term environmental tritium dispersion and tritium migration, accumulation, and uptake in plant ecosystems [44]. Through the modeling, it was discovered that the determination of HTO concentration in the environment is relatively challenging compared with other radionuclides. In the case of HT or T_2 release, estimation of HTO concentration in the air could involve even larger uncertainty because the impact of gaseous tritium release could be modeled by various methods that lead to dispersed results. Varakhedkar et al. modeled atmospheric tritium transport near the Tarapur Atomic Power Station 3 and Station 4 to determine the tritium levels in the environment [45]. The code used in the study is Risø Mesoscale Puff (RIMPUFF), which is a Lagrangian mesoscale puff model. The onsite meteorological data were used for the accurate calculation of tritium dispersion. The results matched well with the measured tritium concentrations near the power plant; therefore, the Lagrangian puff model is validated. Kock and Hamby simulated tritium doses for the public near the Savannah River site (SRS) by using five-year-averaged meteorological data [46]. In their study, the percentage of HTO of the total tritium release was assumed to be 10%. Through the simulation, it was discovered that using long-term-averaged

meteorological data leads to no more than a 6% increase in the total individual doses compared with the monthly dose estimation.

1.1.6 Tritium mitigation in fusion reactors

In the fusion community, two strategies have been investigated to remove T_2 from the primary loop, which is a process of extracting a gas solvent from a liquid solvent. The first strategy is a countercurrent gas-bubbling extraction tower, which is depicted in Figure 1.2.

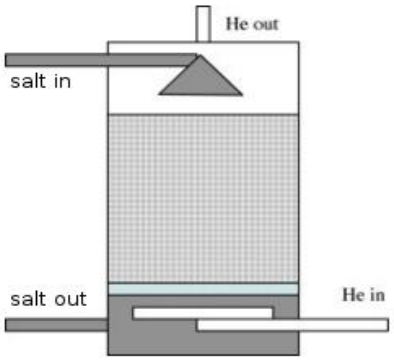

Figure 1.2 Scheme of a countercurrent flow extraction tower [47]

In the countercurrent extraction tower, a sweep gas, such as helium, is bubbled from the bottom of the facility and through the molten salt FLiBe, which flows downward in the tower. Under the influence of helium gas bubbles, T_2 dissolved in FLiBe will transport into the gas bubbles and be carried out of the system. The required size of the countercurrent extraction tower can be estimated using the model developed by Fukada et al. [47], as specified in the following:

$$h_G = 3.07 \frac{G^{0.32}}{L^{0.51}} \left(\frac{\mu_G}{\rho_G D_G} \right)^{2/3}, \tag{1.7}$$

$$h_L = \frac{1}{430} \left(\frac{L}{\mu_L} \right)^{0.22} \left(\frac{\mu_L}{\rho_L D_L} \right)^{0.5}, \tag{1.8}$$

$$h_{tower} = \frac{GR_gT}{k_G a_V p_T} \int_{p_{T_2,in}}^{p_{T_2,out}} \frac{\mathrm{d}p_{T_2}}{p_{T_2,i} - p_{T_2}} \ , \tag{1.9}$$

where

h_L and h_G are called the heights equivalent to the theoretical plate of liquid-phase and gas-phase mass transfer, respectively, m [48];

h_{tower} is the height of the countercurrent extraction tower, m;

k_G is the diffusion coefficient, m/s;

and a_V is the total surface area of the bubbles in a unit volume, m^{-1}. The diffusion rate through the gaseous boundary layer of the He–D_2 mixture is controlled by $k_G a_V$, which has the unit of s^{-1};

p_{T_2} is the T_2 partial pressure in the gaseous phase, Pa;

G and L are the molar flow rates of the gas and liquid phase, respectively, mol/(m^2-s);

μ is the fluid viscosity, P;

ρ is the density, g/cm^3;

R_g is the ideal gas constant;

T is the temperature, K;

and subscript G and L represent the gas and liquid phases, respectively.

The second strategy to remove tritium is to use a permeation-window extraction facility. The basic scheme of the permeation-window extraction facility is shown in Figure 1.3. This type of equipment is designed based on the selective permeability of metal to tritium. The permeable tube is made of a highly tritium-permeable metal material. Between the permeable tube and the nonpermeable tube, a sweep gas, such as helium, helps maintain a low tritium concentration on the downstream side of the window, i.e., on the helium side. While tritium can permeate the inner tube and be carried away by the sweep gas, other contents in the primary coolant are left inside the permeable tube [49][50]. As a result, tritium is extracted from the primary loop.

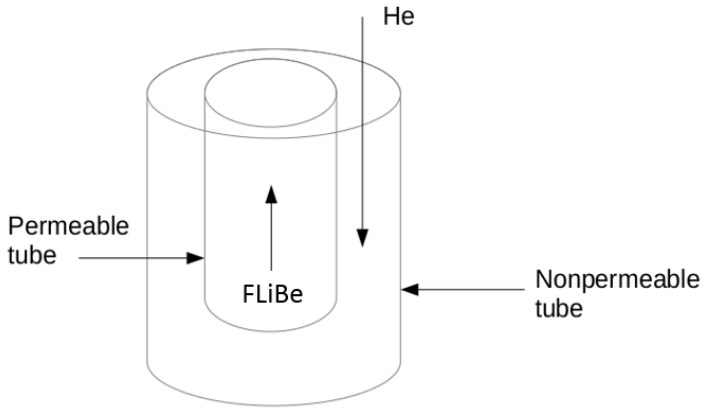

Figure 1.3 Basic scheme of a permeation-window extraction facility

The total surface area needed for the permeation window can be calculated using the following equation:

$$A = \frac{Q}{h_o} \frac{\ln\left(\frac{c_{in} - H_{T_2} p_2}{c_{out} - H_{T_2} p_2}\right)}{\left(c_{in} - H_{T_2} p_2\right) - \left(c_{out} - H_{T_2} p_2\right)} \ , \tag{1.10}$$

where

h_o is the overall mass transfer coefficient derived from tritium diffusivities and solubilities in FLiBe, tube wall, and helium;

p_2 is the partial pressure of T_2 in the downstream of the window on the helium flow side; and c_{in} and c_{out} are, respectively, the inlet and outlet T_2 concentrations in the upstream of the window on the liquid molten salt side, as shown in Figure 1.3.

1.2 Dissertation motivation

It is generally considered that the tritium challenge in FHRs needs to be adequately resolved prior to any licensing application submission to the U.S. Nuclear Regulatory Commission for FHR design certification. To address this challenge, the potential impact of the tritium released into the

environment needs to be investigated to determine the maximum-allowable tritium-release rate from an FHR plant before proposing tritium management strategies for FHRs. However, in addition to the studies reviewed in the previous sections, very few studies have been performed directly on the radiation doses that the public may receive from chronic tritium releases, especially airborne tritium.

The results of tritium-dispersion studies can help determine the required level of tritium control in FHR systems and the corresponding required tritium removal rate. Tritium-control strategies in FHRs have been studied by several researchers. Forsberg et al. proposed a tritium absorption approach using carbon [51]. This strategy takes advantage of the high tritium solubility in carbon and the abundance of graphite moderators in an FHR reactor core. Experience in the fusion community could also be adapted to FHR conditions. Similar to the permeation-window-type tritium-extraction facility, a double-wall intermediate heat exchanger with tritium removal in the wall gap was proposed [52]. This integrated heat exchanger fulfills the objective of tritium removal in addition to heat transfer. In addition, based on the permeation window concept, a tritium control and mitigation system employing a cross-flow tritium removal facility was proposed in an early study by the author [53], but the effectiveness and efficiency of the tritium removal rate from the reactor system in the designed cross-flow tritium removal facility have not been carefully validated, although the facility design has been modeled using FAE simulation software. Currently, most computer codes are developed to calculate the mass transfer process in cocurrent and countercurrent flow configurations. Mass transport in more complex flow configurations can be simulated only by finite element analysis (FEA) software, such as COMSOL Multiphysics. The cost of FEA computational simulation is generally high; therefore, low-cost computer code is desired for the evaluation of mass transfer in complex flow configurations.

The effectiveness and efficiency of the designed facility in the FHR system are uncertain because no experiments in flowing molten salts have been carried out to examine tritium transport in permeation-window-type facilities yet. In the Mark I pebble-bed (PB) FHR design, small graphite pebbles were proposed to serve as a tritium sink, absorbing tritium in the reactor core [54][55]. Calculation of the capacity of tritium removal by graphite pebbles in the Mark I PB FHR was carried out, but no experimental data are available yet. On the other hand, there have been various

experiments on tritium permeation through metallic materials with a flowing tritium gas [56][57], tritium ion beam [58], or dissolved tritium in stationary molten salts [59]; but no experiments have been conducted using tritium dissolved in flowing molten salts. The currently proposed tritium-management strategies are based on computational modeling and simulations with tritium transport properties in the literature, and it is necessary to validate these designs against experiments performed under relevant prototypic operating conditions.

To address the above-mentioned technical gaps, tritium dispersion in the atmosphere has been modeled with an emphasis on the radioactive dose received by residents near an FHR plant site, and a tritium analysis code has been developed using a logarithmic mean square root of partial pressure differential method. The doses to the residents were calculated using GENII, which is an environmental radiation dosimetry software system. Three potential locations for FHR construction were selected for the analysis, and actual historical meteorological and most recent census data were used to study potential health impact to the public near those locations. The tritium analysis code was preliminarily validated using a hydrogen-permeation experiment in the literature and a laboratory-scale experiment designed and carried out specifically for the cross-flow tritium removal concept. The results and conclusions of this study will help identify a tritium-release limit for FHRs and contribute to future research on tritium control strategies. Figure 1.4 demonstrates the workflow of this research work.

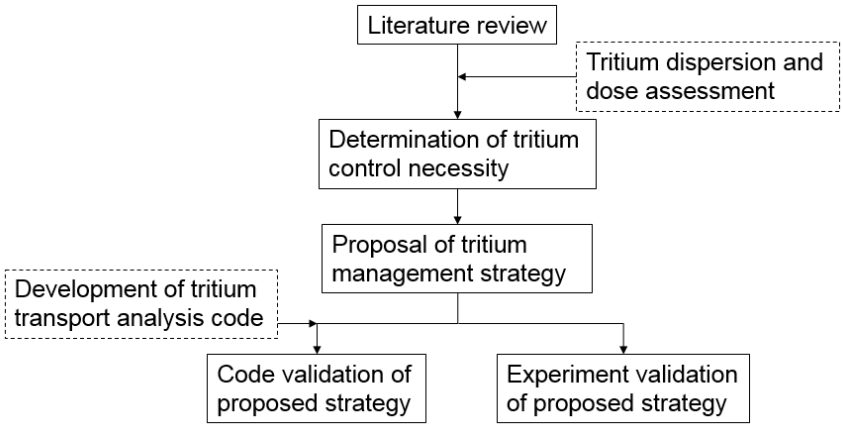

Figure 1.4 Workflow of this research

1.3 Dissertation outline

In this dissertation, a tritium control and mitigation strategy is developed with the attempt to address the tritium-management challenge in FHRs. The approach taken in the development of the strategy is to first quantify the potential impact of tritium generated from FHRs, then to propose a tritium control and mitigation system, and lastly to evaluate the effectiveness and efficiency of the tritium removal facility design. A summary for each chapter is presented as follows:

In this chapter (Chapter 1) of the dissertation, background information on tritium generation and transport in FHR systems is introduced. The tritium generation rates from different reactor systems are compared and the tritium health impact on human beings is reviewed to illustrate the significance of the challenge. The tritium transport properties of common reactor construction materials are reviewed.

Chapter 2 describes our investigation of tritium dispersion in the atmosphere. Based on the results of calculated maximum dose for the public and current regulatory policies regarding radioactive materials and tritium dispersion studies, a preliminary tritium release limit is proposed.

Chapter 3 briefly reviews previous work on the tritium control and mitigation system featuring a cross-flow tritium removal facility upon which the current study is based.

Chapter 4 introduces the development of a calculation method for mass transport: the logarithmic mean square root of partial-pressure difference (LMSPD). This method is implemented in MATLAB and Python. Two experiments are used to validate the code: one is a hydrogen-permeation experiment in the literature and the other is a gas-separation experiment which used a laboratory-scale, cross-flow tritium removal facility. The experimental data and the code calculation results are compared and discussed. The results agree well with the experimental data, confirming the correctness of the LMSPD method.

Chapter 5 presents the conclusions and a summary of the study. Suggestions for future research on this subject are also proposed.

Chapter 2. Tritium Dispersion in the Environment

This chapter discusses the atmospheric dispersion of airborne tritium and the resulting health impacts on the public. Tritium dispersion relies strongly on local meteorological and surrounding surface conditions, and a generalized prediction might not be accurate. Therefore, the effect of each parameter on the resulting doses received by the residents near the nuclear power plant site is of value. Atmospheric tritium dispersion was modeled using computer codes, and a parametric study of key meteorological variables was carried out. Three sites were selected for the modeling and are compared for suitability of FHR construction. Historical meteorological data were used for the dose assessment from FHR tritium release. An uncertainty analysis was performed to examine the reliability of the prediction of dose equivalent for the near future. The major objective of the analysis of tritium dispersion and dose assessment is to determine whether measures should be taken to reduce the tritium release rate from FHRs, and if there is such a necessity, to investigate the amount of tritium to be prevented from entering the environment.

2.1 Comparison of codes for the dispersion of radioactive materials

During the past decades, researchers have developed several computer codes for modeling and calculating tritium dispersion in the atmosphere. However, different codes have different emphases and focuses [60]. A literature search was carried out to compare the codes and select a suitable one for this study. The codes reviewed are summarized in the following.

The ETMOD (Environmental Tritium Model) is a code developed by Ontario Hydro. It calculates the radiological impact of short duration atmospheric tritium release; species include HTO and HT. The processes of tritium dispersion that ETMOD simulates include atmospheric dispersion of the plume, deposition to and reemission from soils and plants, and chemical transformation of tritium in soils. For the atmospheric-dispersion modeling, the Gaussian plume model with horizontal and

vertical parameters is adopted [61]. Doses to the public are calculated via inhalation and food and drink pathways [21].

AIRDOS-EPA is a computerized model developed by Oak Ridge National Laboratory (ORNL). It estimates environmental concentrations and doses to the public from the airborne release of radionuclides, including HTO and HT. The same as ETMOD, the Gaussian plume model is used for the atmospheric tritium dispersion. In the evaluation of doses received by human beings, two pathways are considered for HTO: inhalation and ingestion, while only inhalation is considered for HT [62].

The computer codes family RESRAD is designed by Argonne National Laboratory for evaluating the radiation doses and risks from residual radioactive materials [63]. The RESRAD codes contain several modules, each can be used under different scenarios. The codes allow users to specify the surrounding environment of the contaminated site, for instance, the distance and area of a nearby waterbody, to reflect specific conditions [64]. The radiation taken-up pathways include external exposure in addition to inhalation and ingestion, which is more comprehensive than just including the latter two.

GENII is developed as the second generation of environmental dosimetry computer code by Pacific Northwest National Laboratory [65]. It is recognized by DOE as a safety analysis toolbox code. GENII has the ability to model both chronic and acute radiological material releases to water or to air, or contamination of soils or surfaces [66][67]. In the atmospheric-dispersion modeling, both straight-line Gaussian-plume and Lagrangian-puff models are incorporated. The same as RESRAD, calculation of doses to human beings includes several pathways: inhalation, ingestion, and direct exposure.

In this study, GENII is selected for the investigation of the health impact of chronic tritium release from FHRs to the public and the effects of various meteorological parameters on the doses received by the residents.

2.2 Model setup

The model selection of the tritium dispersion and public dose calculation consist of two major parts: the selection of locations being modeled and the input parameters in GENII code. The selection of locations is mainly based on the probabilities of future FHR constructions. The input parameters include information of the tritium source, meteorological data of the selected site, population distribution around the assumed tritium release location, etc.

2.2.1 Sites selection

Because there have not been FHRs constructed in the United States, the candidate sites in the simulation are locations that have attracted interest for future molten salt reactor constructions or have histories on large tritium airborne release. Three locations are selected: the Hanford site, the Idaho Falls site and the Oak Ridge site. Hanford site was a candidate location for Thorcon Power to build their future FHR. The Idaho Falls site is a potential molten salt reactor construction location. The Oak Ridge site is selected because the molten salt reactor experiments were conducted at this location in the 1960s. In this simulation, the tritium release rate is assumed to be at constant 18.5 TBq/day and the species release is assumed to be 100% HTO for conservative purposes, as explained in section 1.1.2. This assumption models the chronic tritium release during an FHR startup. Meteorological data comes from nearby weather stations (Yakima, Pocatello, and Knoxville weather stations, respectively). For each simulated site, the maximum dose an individual living around the site receives during an operation year of an FHR is calculated.

An hourly meteorological input file is required for GENII calculation. The real meteorological data of the year 1990 is selected as the "base" case for the simulation. The meteorological files of the year 1990 can be found in Appendix A. Temperature, wind speed, and absolute humidity are varied on the base case for the investigation of their effects on the maximum dose that individuals receive. The major meteorological parameters of the three selected sites of the year 1990 are plotted in Figure 2.1 to Figure 2.9. We can observe that the shapes of temperature or humidity distributions are similar for all three sites. However, the wind speed and direction distributions vary significantly. At the Hanford site, the dominant wind direction is west, and the most common

wind speed range is 3-5 m/s, which takes up 17% of the time. At the Idaho Falls site, most of the time, wind comes from north and northeast, and its speed varies from 0 to 9 m/s. For a small fraction of time, the wind direction is southwest with a major speed range of 3-5 m/s. However, at the Oak Ridge site, the wind most commonly comes from two opposite directions, northeast and between south and southwest. And the wind speed at the Oak Ridge site is relatively lower than the other two sites, its main range being 1-3 m/s.

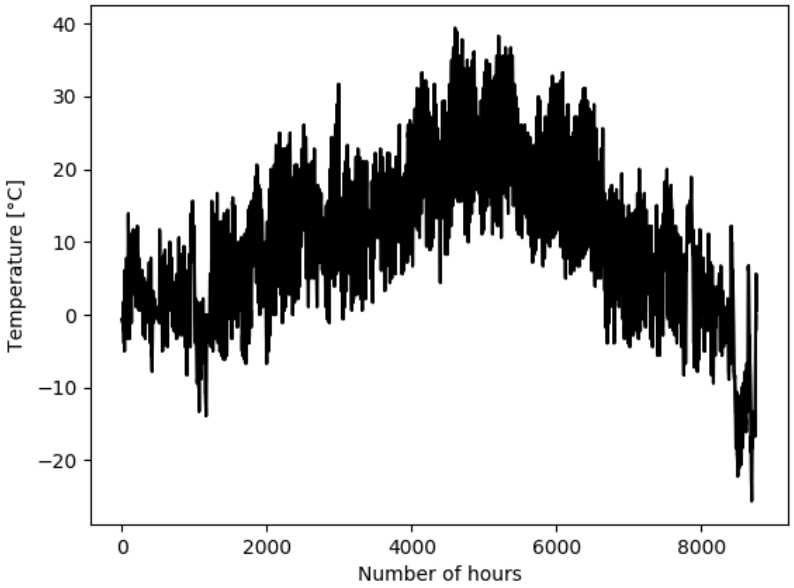

Figure 2.1 Hourly temperature at the Hanford site in 1990

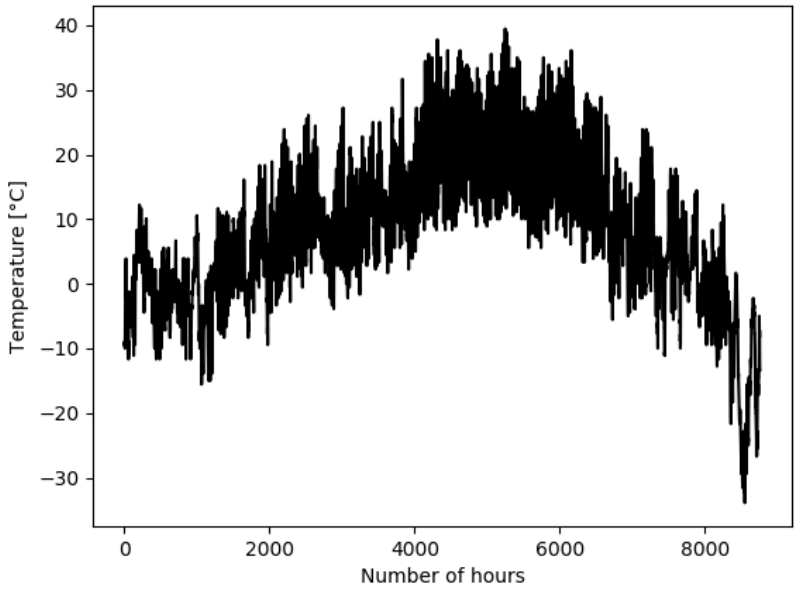

Figure 2.2 Hourly temperature at the Idaho Falls site in 1990

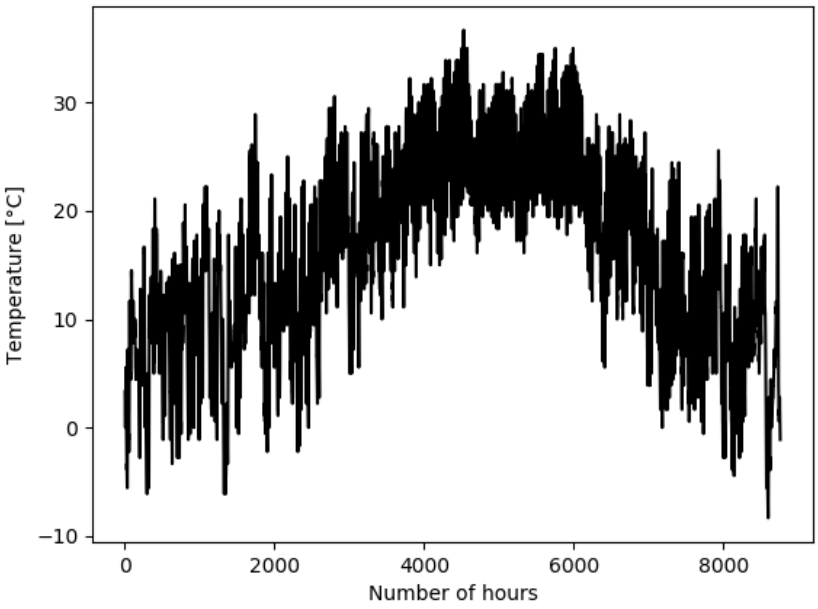

Figure 2.3 Hourly temperature at the Oak Ridge site in 1990

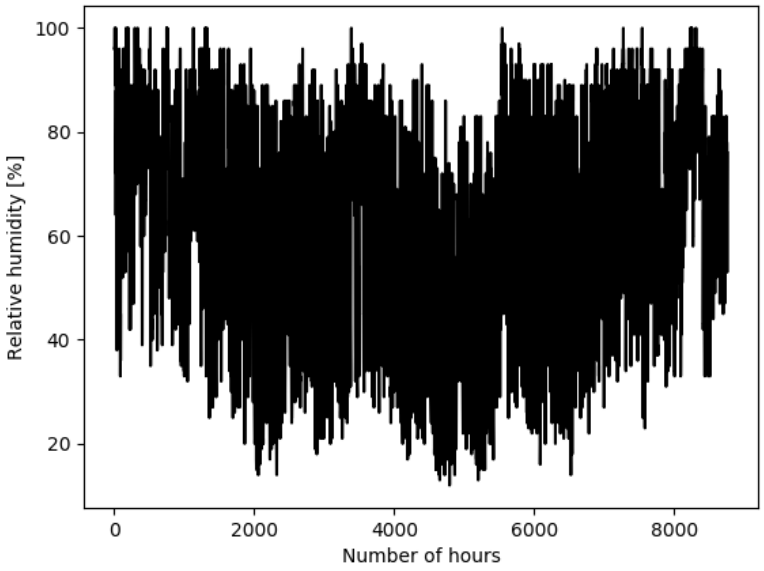

Figure 2.4 Hourly relative humidity at the Hanford site in 1990

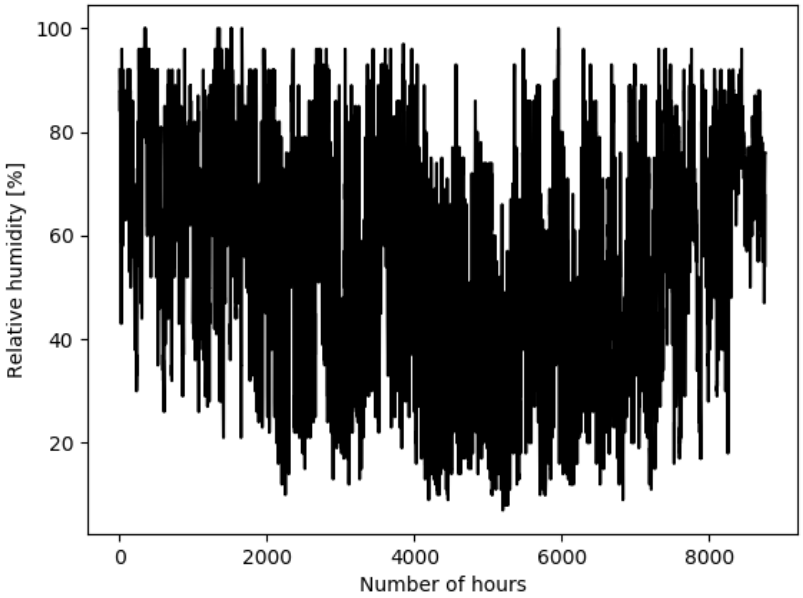

Figure 2.5 Hourly relative humidity at the Idaho Falls site in 1990

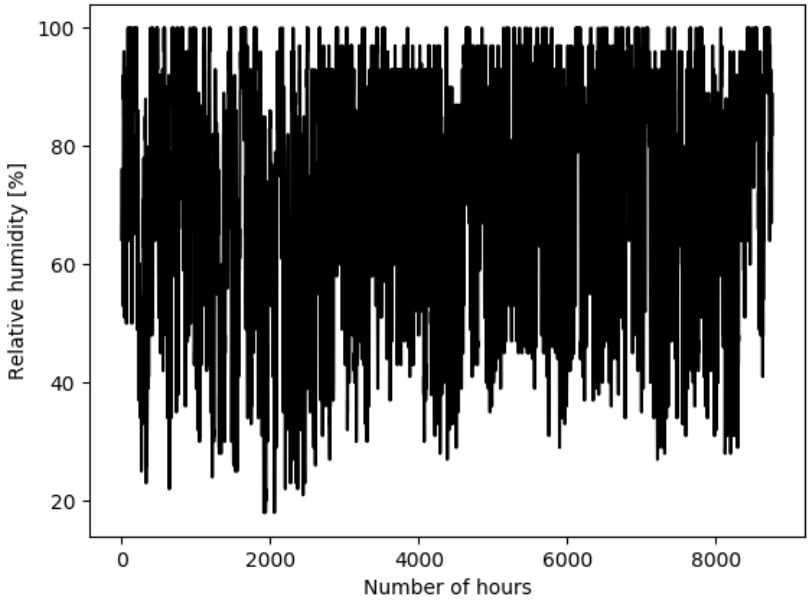

Figure 2.6 Hourly relative humidity at the Oak Ridge site in 1990

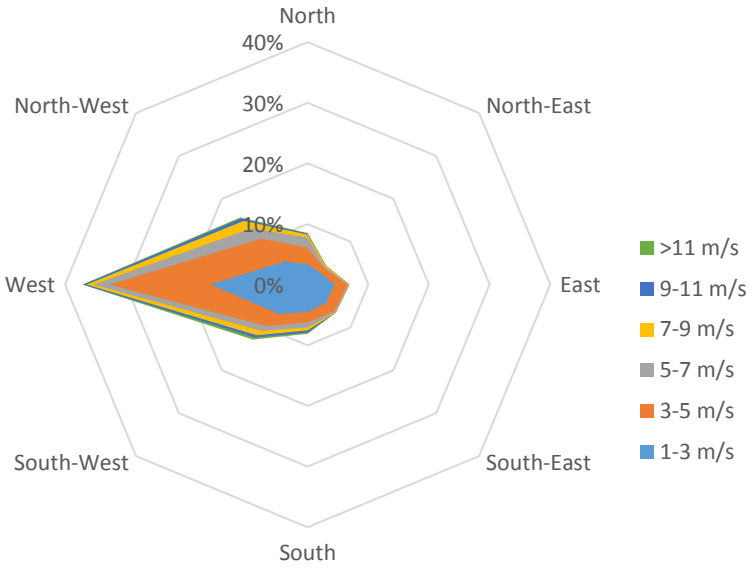

Figure 2.7 Hourly wind direction and speed at the Hanford site in 1990

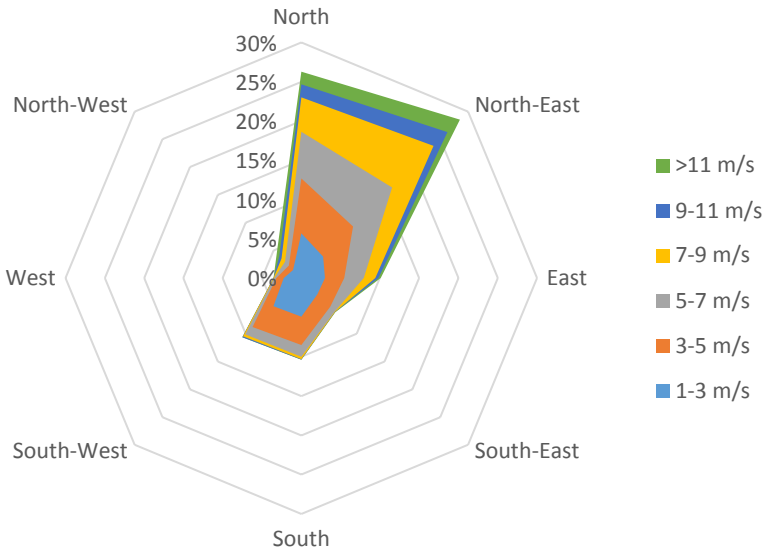

Figure 2.8 Hourly wind direction and speed at the Idaho Falls site of 1990

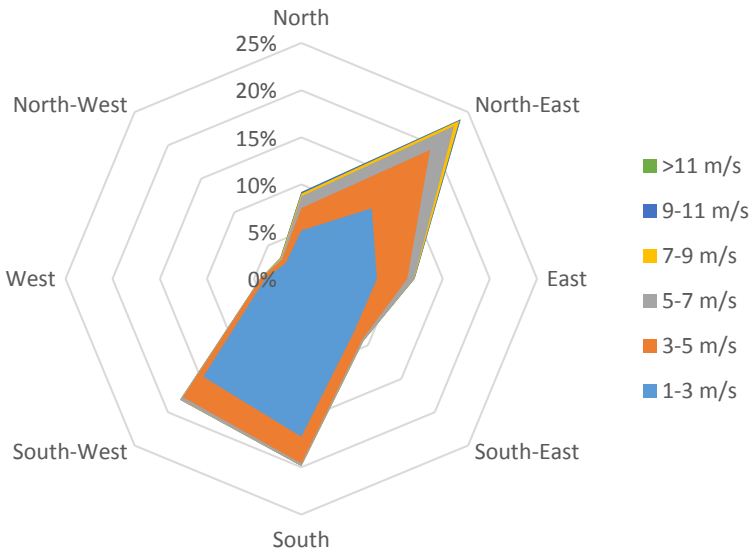

Figure 2.9 Hourly wind direction and speed at the Oak Ridge site of 1990

2.2.2 Dispersion model selection

Two models are usually adopted in the calculation of the atmospheric dispersion and transport of the radioactive materials: the Gaussian plume model and the Lagrangian puff model. The basic equation of the Gaussian plume model is:

$$\frac{\chi\left(x,y,z,H,H_{eff}\right)}{Q'(x)}=\frac{1}{2\pi U\left(H_s\right)\sigma_y\sigma_z}\exp\left(-\frac{y^2}{2\sigma_y^2}\right)G(z), \tag{2.1}$$

where

χ is the concentration at a distance x, crosswind position y, and height z, in a plume with the axis at height H_{eff}, [Bq/m^3];

$Q'(x)$ is the release rate of the radioactive material (tritium in this study), [Bq/s];

$U\left(H_s\right)$ is the wind speed at the release height H_s, [m/s];

σ_y and σ_z are the horizontal and vertical dispersion coefficients of the released radioactive material, respectively, [m];

and $G(z)$ is the vertical dispersion factor, defined as the following:

$$G(z)=\sum_{n=-\infty}^{\infty}\exp\left(-\frac{\left(2nH-\left(z-H_{eff}\right)\right)^2}{2\sigma_z^2}\right)+\exp\left(-\frac{\left(2nH-\left(z+H_{eff}\right)\right)^2}{2\sigma_z^2}\right), \tag{2.2}$$

where H_{eff} is the effective release height, [m], and H is the thickness of the mixing layer, [m].

The basic equation of the Lagrangian puff model is:

$$\chi_p\left(r,z,t\right)=\frac{Q_p\left(t_0,t\right)}{\left(2\pi\right)^{\frac{3}{2}}\sigma_r^2\sigma_z}\exp\left(-\frac{r^2}{2\sigma_r^2}\right)G(z), \tag{2.3}$$

where

$\chi_p(r,z,t)$ is the concentration of the puff at the distance r, height z, and at time t, [Bq/m^3];

$Q_p(t_0,t)$ is the mass of the puff released at time t_0, [Bq];

σ_r is the radial dispersion coefficient, and is assumed to be equal to σ_y, [m];

and $G(z)$ is the vertical factor defined in Eq. (2.2).

In this study, the dispersion model selected was the chronic plume model in the air module of GENII. For chronic releasing cases such as the tritium release in this study, the entire area investigated is divided into a grid. The basic Gaussian plume model shown in Eq. (2.1) is integrated and then divided by the width of the sector in the grid, so that the model is averaged for each sector [67]. The resulting model equation is:

$$\frac{\chi(\theta_i,r,z)}{Q'(r)} = \frac{1}{\sqrt{2\pi}U\sigma_z\theta_w}G(z), \tag{2.4}$$

where θ_i denotes the i-th sector and θ_w is the sector width.

2.2.3 Methodology of dose equivalent prediction and uncertainty analysis

Evaluation of uncertainties in dose assessment is a complex process. The conventional sources of uncertainty can be grouped into three main categories: uncertainties in the parameters and models developed for biokinetic and dosimetric for internal dosimetry evaluation, uncertainties in bioassay and environmental measurements for determination of human body radioactive material intake, and uncertainties in the quantities and aspects for intake characterization. However, these are based on the usual assessment methods that rely on measuring monitoring, bioassay or radiation imaging techniques [68]. In this study, an uncertainty source comes from the values of meteorological parameters is not negligible. To quantify the uncertainty of the dose calculation, an uncertainty analysis was conducted. A prediction of the maximum dose that an individual of the public could

possibly receive from chronic tritium release was calculated. A variance-based global sensitivity analysis was carried out to show the cause of the variance in the dose equivalent prediction.

We employed the Gaussian Processes (GPs) to construct a surrogate model so that the uncertainties of meteorological parameters can be efficiently propagated through the surrogate model to obtain the uncertainty of the dosage. Furthermore, based on the surrogate model, we performed a quantitative global uncertainty analysis to evaluate the individual influence of these meteorological parameters toward the tritium release prediction at each site. The workflow is demonstrated in Figure 2.10.

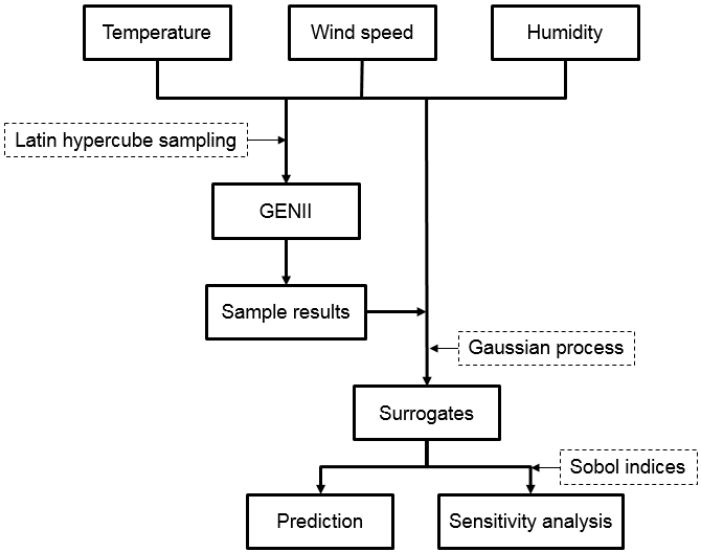

Figure 2.10 Workflow of the dose equivalent prediction process

2.4.1.1 Methodology of uncertainty analysis

The prediction value y^M can be obtained using the following model:

$$y^M(\mathbf{q},\boldsymbol{\beta}) = \sum_{i=1}^{m} h_i(\mathbf{q})^T \beta_i + \mathbf{f}(\mathbf{q}) = \mathbf{h}(\mathbf{q})^T \boldsymbol{\beta} + Z(\mathbf{q}), \tag{2.5}$$

where

$\mathbf{q}$ is a vector of length p, each element represents an input variable;

$\boldsymbol{\beta}$ is the regression coefficients vector of length m;

$\mathbf{h}(\mathbf{q})$ is the basis function of a known form, usually a polynomial function;

and $Z(\mathbf{q})$ is the Gaussian process error model, which, has a mean of 0, a variance of σ^2, and a nonzero covariance $Cov\left[Z\left(\mathbf{q}^{(i)}\right), Z\left(\mathbf{q}^{(j)}\right)\right] = \sigma^2 K\left(\mathbf{q}^{(i)}, \mathbf{q}^{(j)}\right)$ where $K\left(\mathbf{q}^{(i)}, \mathbf{q}^{(j)}\right)$ represents the kernel function.

The kernel function is a function of the distances between two input vectors and hyperparameters, which are independent of the physical process modeled. The hyperparameters are usually obtained from point estimate methods, one of the most popular methods being the Maximum Likelihood Estimate [69].

The parameters of the Gaussian process model can be obtained by training the model using a large number of known inputs and corresponding outputs from the physical process being modeled. After training with N pairs of inputs and outputs, the functions in Eq. (2.5)can be expressed in the form of matrices, shown as follows:

$$\mathbf{H} = \left[\mathbf{h}\left(\mathbf{q}^{1}\right), \mathbf{h}\left(\mathbf{q}^{2}\right), \cdots, \mathbf{h}\left(\mathbf{q}^{\mathbf{N}}\right)\right] = \begin{pmatrix} h_1\left(\mathbf{q}^1\right) & \cdots & h_1\left(\mathbf{q}^N\right) \\ \vdots & \ddots & \vdots \\ h_m\left(\mathbf{q}^1\right) & \cdots & h_m\left(\mathbf{q}^N\right) \end{pmatrix}, \tag{2.6}$$

$$\mathbf{K} = \begin{pmatrix} K\left(\mathbf{q}^{(1)}, \mathbf{q}^{(1)}\right) & \cdots & K\left(\mathbf{q}^{(1)}, \mathbf{q}^{(N)}\right) \\ \vdots & \ddots & \vdots \\ K\left(\mathbf{q}^{(N)}, \mathbf{q}^{(1)}\right) & \cdots & K\left(\mathbf{q}^{(N)}, \mathbf{q}^{(N)}\right) \end{pmatrix}, \tag{2.7}$$

$$\mathbf{y}^M = \left[y^M\left(\mathbf{q}^{(1)}\right), y^M\left(\mathbf{q}^{(2)}\right), \cdots, y^M\left(\mathbf{q}^{(N)}\right)\right]. \tag{2.8}$$

With the known functions, given a new set of input parameters, the corresponding prediction $\hat{y}^M\left(\mathbf{q}^*\right)$ can be obtained by the following expression of the Gaussian process model:

$$\hat{y}^M\left(\mathbf{q}^*\right)=\mathbf{h}\left(\mathbf{q}^*\right)^T\hat{\boldsymbol{\beta}}+K^{*T}\mathbf{K}^{-1}\left(\mathbf{y}^M-\mathbf{H}\hat{\boldsymbol{\beta}}\right), \tag{2.9}$$

where

$\mathbf{q}^*$ is the new set of input parameters;

the regression coefficients estimator $\hat{\boldsymbol{\beta}}=\left(\mathbf{H}^T\mathbf{R}^{-1}\mathbf{H}\right)^{-1}\mathbf{H}^T\mathbf{K}^{-1}\mathbf{y}^M$;

and $K^*=\sigma^2\left[K\left(\mathbf{q}^*,\mathbf{q}^{(1)}\right),K\left(\mathbf{q}^*,\mathbf{q}^{(2)}\right),\cdots,K\left(\mathbf{q}^*,\mathbf{q}^{(N)}\right)\right]$ represents the kernel function with the new input parameters.

The variance of the predictor from the Gaussian process model can be obtained by

$$Var\left(\hat{y}^M\right)=\sigma^2\left[1-\left(\mathbf{h}^T\left(\mathbf{q}^*\right)\quad K^{*T}\right)\begin{pmatrix}0 & \mathbf{H}^T\\ \mathbf{H} & \mathbf{R}\end{pmatrix}\begin{pmatrix}\mathbf{h}^T\left(\mathbf{q}^*\right)\\ K^{*T}\end{pmatrix}\right]. \tag{2.10}$$

2.4.1.2 Methodology of global sensitivity analysis

Besides the prediction of the dose equivalent to individuals in the near future, the contribution of each input parameter is quantitatively evaluated using the Sobol method [70]. The Sobol method assumes independence and uniform distribution on [0, 1] of the parameters. The general model of the Sobol method used in the computational analysis is expressed as the following:

$$y^M\left(\mathbf{q}\right)=f_0+\sum_{i=1}^{p}f_i\left(q_i\right)+\sum_{1\le i<j\le p}f_{ij}\left(q_i,q_j\right), \tag{2.11}$$

where,

$f_0 = \int_{\Gamma^p} y^M(\mathbf{q})\, d\mathbf{q}$ is the zeroth-order term;

$f_i(q_i) = \int_{\Gamma^{p-1}} y^M(\mathbf{q})\, d\mathbf{q}_{\sim \mathbf{i}} - f_0$ is the first-order term;

and $f_{ij}(q_i, q_j) = \int_{\Gamma^{p-2}} y^M(\mathbf{q})\, d\mathbf{q}_{\sim \mathbf{i}} - f_i(q_i) - f_j(q_j) - f_0$ is the second-order term, with $\Gamma^p = [0,1]^p$, $\mathbf{q}_{\sim \mathbf{i}}$ represents a vector having all elements except the i-th of $\mathbf{q}$.

Let D_{var} denote the total variance of y^M, the model prediction, then the expression of D_{var} is shown in the following equation:

$$D_{\text{var}} = \int_{\Gamma^p} y^{M^2}(\mathbf{q})\, d\mathbf{q} - f_0^2 = \sum_i D_i + \sum_{1 \le i < j \le p} D_{ij}\,, \tag{2.12}$$

where D_i and D_{ij} are partial variances with the expressions of

$$D_i = \int_0^1 f_i^2(q_i)\, dq_i\,, \tag{2.13}$$

$$D_{ij} = \int_0^1 f_{ij}^2(q_i, q_j)\, dq_i\,. \tag{2.14}$$

The ratios of partial variances to the total variance are the Sobol indices shown as follows:

$$\begin{aligned} S_i &= \frac{D_i}{D}, \\ S_{ij} &= \frac{D_{ij}}{D}, \end{aligned} \tag{2.15}$$

where $i, j = 1, 2, \cdots, p$.

Sobol indices shows the influence of a parameter on the prediction. A strong influence of parameter i on the prediction would result in a high first-order Solol index S_i, while a strong interaction between two parameters i and j would results in a high second-order Sobol index S_{ij}. In this study, it is assumed that no interactions exist between the meteorological parameters, and therefore, only the first-order Sobol indices are calculated. By definition, the Sobol indices of all the parameters sum up to 1.

2.4.2 Inputs and outputs from GENII model

In this modeling, the tritium source was set as a single point release source. The form of tritium released was assumed to be 100% HTO, i.e., tritiated water vapor. Organic bonded tritium is included automatically in GENII because it is generated during the dispersion process, but the initial release level is set as 0. The release exit was set as a point 60-meter stack. The temperature of the released puffs was assumed to be room temperature, i.e., 25 °C. The exit area of the source was assumed to be 2 m^2. The topography parameter, or height of adjacent structures, was set as 10 m.

The radial grid of the calculation used was divided evenly into 16 sectors, and the distances were from 5 to 50 km, with 5 km intervals. As a demonstration of this dividing method, the map of the Hanford site is shown in Figure 2.11. Briggs' open country scheme was selected, which applies to sites where the surrounding area within 10-stack heights or building heights of the source is not mostly built-up. This description is in agreement with the three sites selected in this modeling. The curves of the dispersion coefficients are described in Briggs' work [71]. The expressions of the diffusion coefficients in the y and z directions are also listed in Table 2.1, where x is in the unit of meter. The diffusion coefficients are functions of the Pasquill stability classification, which indicates the level atmosphere stability. Class A represents highly unstable, and class F represents high stable. The population data were obtained from the newest statistical data of the Census Bureau at the level of counties. It was assumed that inside each county, the population distribution

is even. In the grid, each area may cover several counties. In this case, inside each area, the population is assumed to distribute evenly. In Figure 2.11, the total population of each area is demonstrated by color. We can observe that most population resident to the south and southeast of the Hanford site.

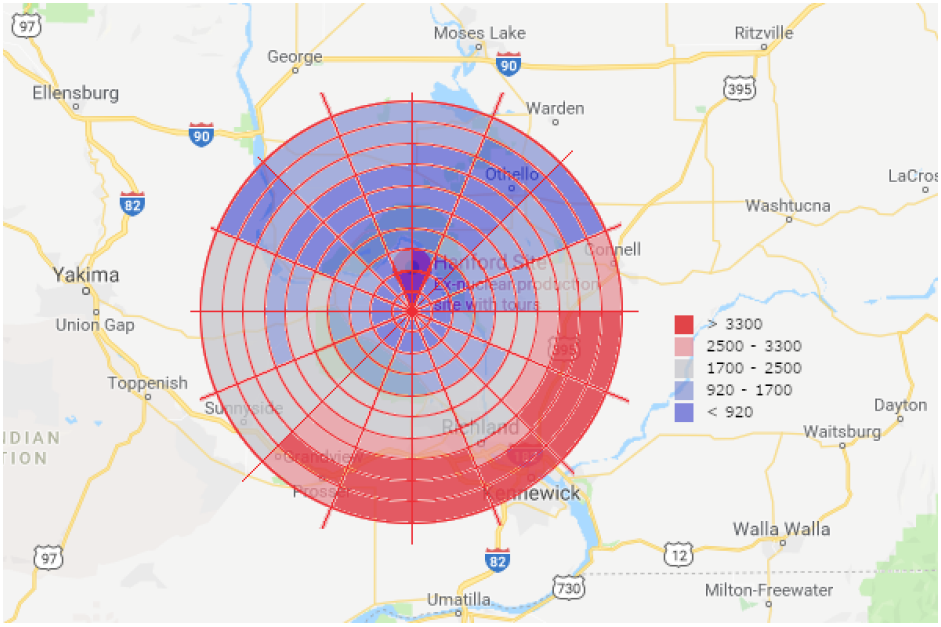

Figure 2.11. Grid of calculation for the Hanford site

Table 2.1. Diffusion coefficients of the Brigg's open country scheme

Pasquill stability classification	σ_y	σ_z
A	$0.22x(1+0.0001x)^{-0.5}$	$0.20x$
B	$0.16x(1+0.0001x)^{-0.5}$	$0.12x$
C	$0.11x(1+0.0001x)^{-0.5}$	$0.08x(1+0.0002x)^{-0.5}$
D	$0.08x(1+0.0001x)^{-0.5}$	$0.06x(1+0.0015x)^{-0.5}$
E	$0.06x(1+0.0001x)^{-0.5}$	$0.03x(1+0.0003x)^{-1}$
F	$0.04x(1+0.0001x)^{-0.5}$	$0.016(1+0.0003x)^{-1}$

The population was divided into six age groups. The age ranges of the groups are 0–9, 10–24, 25–44, 45–59, 60–84, and above 85 years. Individuals were assumed to be exposed to the radiation for 24 hours per day and 365 days per year. All the radiation dose take-up pathways that are applicable to airborne radioactive material release are incorporated, including meat, milk, plant-sourced food, drinks, air, and soil contact.

The output of from GENII is the maximum dose equivalent that an individual receives if the individual resides near the modeled tritium release point. This value represents the highest health risk that the public is exposed to at the modeled level of chronic tritium release.

2.3 Parametric study of key meteorological parameters

In total, for the three tritium release sites modeled, five parameters were investigated, three of which are meteorological parameters, one geometric parameter, and the other the tritium release rate. All five parameters were varied individually. The real meteorological data of the year 1990 was used as the "base" meteorological file for the parametric study, and while each parameter was studied, the other parameters were fixed at the 1990 values. The three meteorological parameters studied are the atmosphere temperature, humidity, and wind speed. The geometric parameter studied is the height of the tritium release point, which is part of the tritium source modeling.

2.3.1 Effect of the atmosphere temperature on dose assessment

The temperature was the first parameter investigated in the study. Although the tritium concentration in the rain is not affected by temperature, the dispersion of tritium in the environment is highly affected by temperature in other aspects [28]. The range of temperature variation is from –10 to 10 degrees different from the 1990 values in Celsius. The points in the plots represents the historical annual average temperature of the three sites. For every hourly temperature, the value is adjusted by increasing or decreasing 1 degree at a time. This method preserves the shape of the hourly temperature distribution throughout the year. Figure 2.12 shows the maximum dose received by individuals caused by tritium release during a one-year startup operation of the FHR at each site, and how the dose changes with the change in temperature.

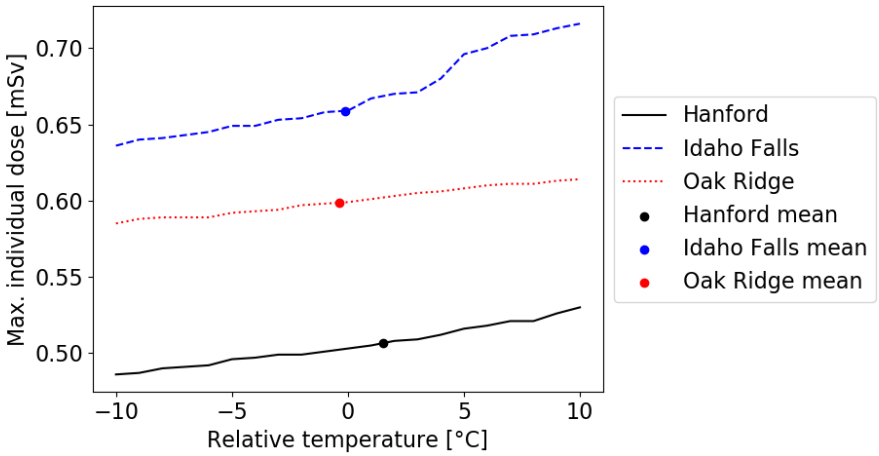

Figure 2.12. Effect of temperature on maximum individual dose

Climate change has received wide attention recently. Studies show that meteorological parameters have the potential to change significantly in the 21st century [72][73]. From the meteorological data of the year 1960 to 2017, more peaks in the parameters such as temperature, and precipitation rate, can be observed in the most recent years, which means the increase of the frequency and severity of extreme climate events. As an example, the annual average daily temperature, maximum and minimum daily temperature at the Hanford site are plotted in Figure 2.13. A slight increase in the average daily temperature can be observed clearly. Since 2010, the averaged minimum temperature has never dropped below –15 °C, which appeared frequently before 2010. In addition, from 2010 to 2017 there were a few sharp peaks in the maximum temperature, the highest value exceeded the historical high by almost 6 °C.

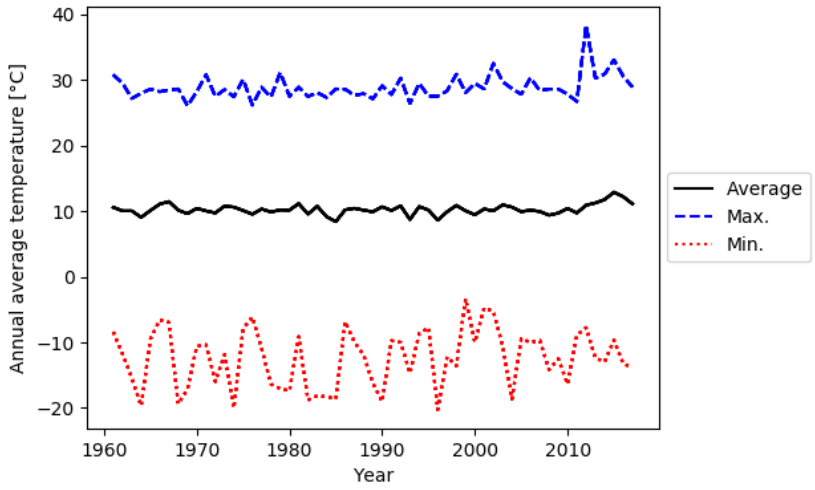

Figure 2.13. Annual average temperatures at the Hanford site

As the temperature increases, the maximum individual dose from tritium release also increases. From the three sites simulated, a 1-°C increase would result in 0.33 – 1.21% increase in the radiation dose. If the temperature increases by 5 °C, an increase of 1.50 – 5.61% in the maximum individual dose is expected. There have been studies showing that by 2100 the surface temperature might rise to 4.8 – 5.8 °C higher than that at the beginning of the 20th century [74]. Therefore, when considering tritium release from FHRs, it is necessary to include the effects of potentially higher temperatures in the upcoming decades.

2.3.2 Effect of wind direction and speed on dose assessment

Wind direction affects the health impact of radioactive materials on the public mainly in the aspect of dose distribution. People living in the downwind areas receive higher doses because of the atmospheric dispersion of tritium. The effect of wind direction on the dose distribution can be observed clearly from Figure 2.14. For the Hanford site, the dominant wind direction is from the west, resulting in the highest individual doses in areas east of the tritium release location. From the plot, it can also be observed that the nearer residents locate toward the release point, the higher dose they receive. Therefore, to avoid taking in excessive radioactive materials, the public can reside at a distance from the tritium release facility and stay clear from the dominant downwind direction.

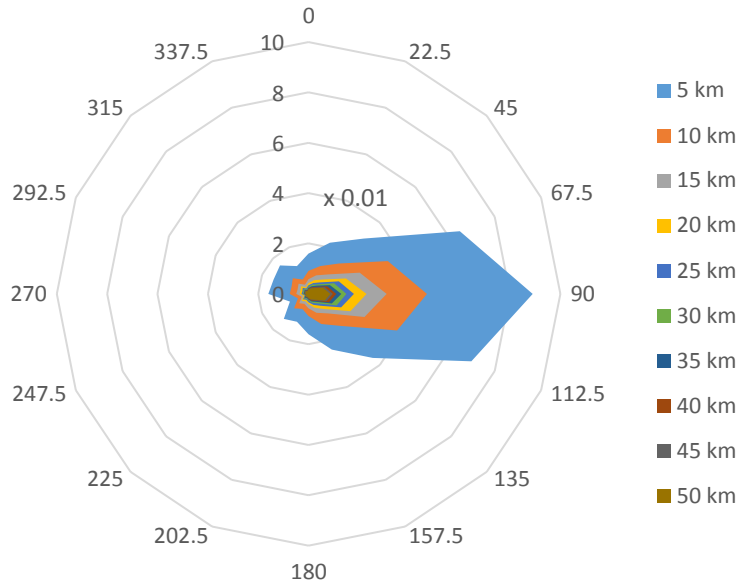

Figure 2.14 Distribution of individual dose received from tritium release at the Hanford site

Wind speed is another major factor that affects the dispersion of radioactive materials [75]. In this calculation, wind speed is varied from 0 to twice the 1990 wind speed values. Figure 2.15 shows the effect of changing the wind speed on the maximum dose individuals receive. The horizontal axis represents the ratio of adjusted wind speed to the 1990 values. The points in the plot represents the historical mean wind speed for the three sites.

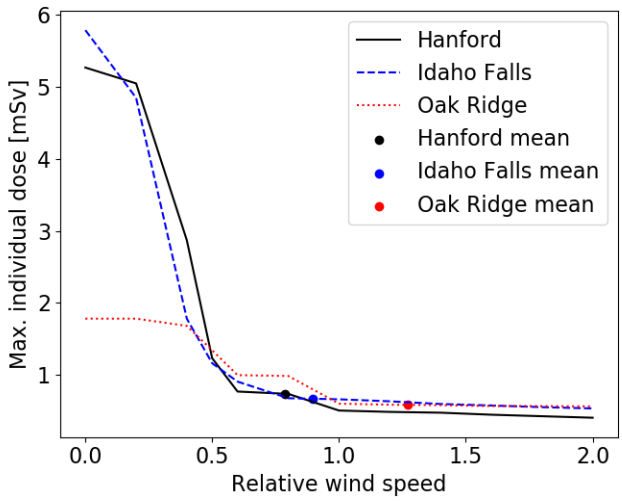

Figure 2.15. Effect of wind speed on maximum individual dose

At lower wind speeds, the maximum dose that an individual receives is obviously higher than at higher wind speeds. As the wind speed increase, the negative impact on public health decreases quickly at first, and then the decrease slows down after about 1 m/s. Comparing the maximum individual dose under no wind conditions and when the wind speed is 1 m/s, for the Hanford site, the former is 10.48 times that of the latter. For the Idaho Falls site, the ratio is 8.79 and for the Oak Ridge site, the ratio is 2.97. Comparing the ratio of maximum individual doses at 1 m/s and 2 m/s wind speeds, it is 1.25, 1.24, and 1.07, for the Hanford site, the Idaho Falls site, and the Oak Ridge site, respectively. The high dose that the public receive at lower wind speeds might come from longer residence periods of tritium because of lack of convection in the air.

2.3.3 Effect of air humidity on dose assessment

Similar to wind speed, the absolute humidity is adjusted in the same manner. The range of absolute humidity is 0.68 to 11.35 g/m^3, which corresponds to 6% to 100% relative humidity at the average temperature. Completely dry condition, i.e., 0 humidity is not modeled because of its rare occurrence. Figure 2.16 shows the change of maximum individual dose at different absolute humidity levels.

The air humidity is affected by several parameters, such as water vapor content, and temperature. All these factors determine the amount of water that unit mass of air can hold. Changes in the humidity can affect the hydrological cycle, which furthermore affects the tritium transport in the entire environment [28].

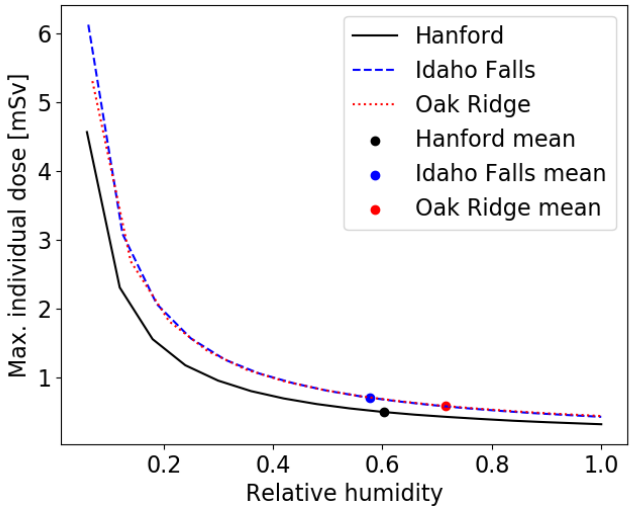

Figure 2.16. Effect of relative humidity on maximum individual dose

The effects of humidity on public health show similar trends for all three locations modeled. Drier climates are in favor of tritium being taken up by human beings. The maximum individual dose drops rapidly as the humidity content increases and then gradually levels off. At 10% relative humidity level, the maximum dose an individual receives is 9.5–10 times that at 100% relative humidity level.

Besides these three parameters investigated, precipitation amount and precipitation intensity are also of interest. However, because of the way GENII deals with precipitation, varying these two parameters does not affect the final maximum individual dose level. This is because, in GENII, the amount of tritium coming down to the ground and taken up by living creatures is estimated in a conservative way. It is assumed that the tritium concentration in leafy vegetables and pasture is 90% of the concentration in air moisture, and in fruit, root crops, other vegetables and grain the ratio is 80%. This assumption makes the dose received by individuals independent of the precipitation parameters in the meteorological input.

2.3.4 Effect of tritium release point height on dose assessment

Because tritium dispersion depends significantly on the local topography, the height of the release point is of interest. The basic equation in the Gaussian dispersion model that is used to calculate the tritium dispersion in the downwind direction is shown as the following:

$$\frac{\chi(x,y,z)}{Q}=\frac{1}{2\pi\bar{u}\sigma_y\sigma_z}\exp\left(-\frac{y^2}{2\sigma_y^2}\right)\left[\exp\left(-\frac{\left(z-H_{eff}\right)^2}{2\sigma_z^2}\right)+\exp\left(-\frac{\left(z+H_{eff}\right)^2}{2\sigma_z^2}\right)\right], \quad (2.16)$$

where

$\chi(x,y,z)$ is the time-integrated concentration at the location (x,y,z);

Q is the tritium release rate;

σ_y and σ_z are the horizontal and vertical diffusion parameters, respectively;

$\bar{u}$ is the mean wind speed;

and H_{eff} is the effective release height.

Although Eq. (2.16) shows how the tritium concentrations at different locations are affected by the release height, to what extent this affects individual doses still needs to be investigated. Under the tritium release rate during FHR normal operation, the maximum annual dose received by an individual is shown in Figure 2.17. Increasing height of the tritium release point is an effective method to lower the health impact on the public. For the Idaho Falls site or the Oak Ridge site, the maximum individual dose level shows a sharp drop when the stack height exceeds 100 m. For the Hanford site, even though the drop at 100 m is not as significant as at the other two sites, the plot still shows an obvious decrease in the maximum individual dose. This drop is considered to be caused by the change of layers of atmosphere. Close to the surface (below 100 m) the wind speed is dominated by surface-based length scales. Above this layer, other length scales can influence the wind speed as well, and the wind speed increases with height [76]. Wind speed influences the Pasqual stability class, which further affects the diffusion coefficients, as indicated in Table 2.1. Continue to raise the release point above 100 m further decreases the health impact on the public

while increases the construction cost. Economic factors need to be taken into consideration when determining the height of the tritium release point. However, it might be reasonable to set the release point higher than 100 m.

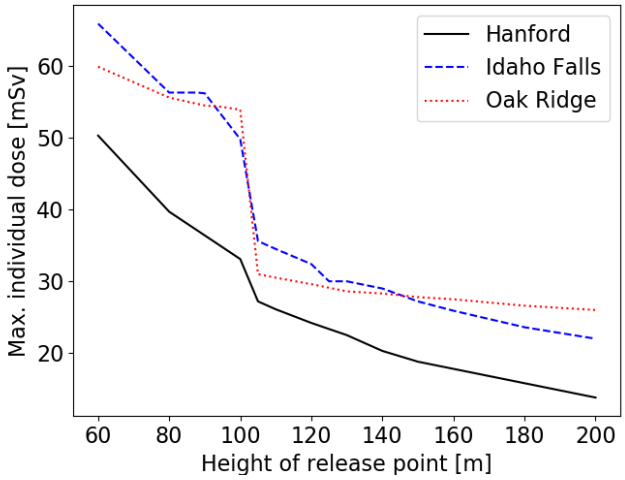

Figure 2.17. Effect of stack height on maximum individual dose

2.3.5 Effect of tritium release rate on dose assessment

It is estimated that during the startup phase of an FHR, the tritium generation rate can be as high as 10 times that during normal operation. The radiation dose an individual receives should be proportional to the tritium release amount. To verify this relationship, in this study, the effect of the length of the startup phase on the radiation dose the public receives was investigated by varying the percentage of time in a year that the reactor is in the startup phase. For the Hanford site, the calculation results are shown in Figure 2.18. The linearity of the line confirms the above statement.

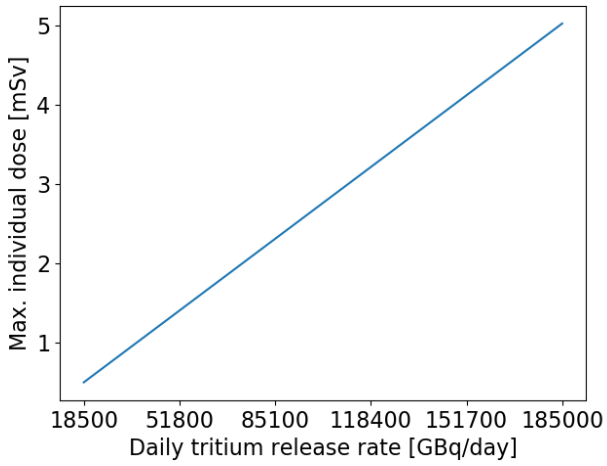

Figure 2.18. Effect of release rate on maximum individual dose

Using the linear relationship between the maximum individual dose and the tritium release rate, the maximum tritium release rate allowed under current public health protection regulations can be calculated. For the Hanford site, to limit the maximum dose an individual receives to under 0.4 mSv/y, the chronic tritium release rate should be less than 14.71 TBq/day if the height of the release point is 60 m. The release rate for the Idaho Falls site is less than 11.23 TBq/day, and for the Oak Ridge site 12.35 TBq/day. If the reactor experiences a startup phase within the calculated year, and the tritium release rate during the startup exceeds the above-calculated value, to make sure the radiation dose to the public stays within the regulatory limit, the tritium release rate during the normal operation will need to be further lowered.

Because the calculated tritium release rate limit is well below the generated rate during normal operation (18.5 TBq/day), a tritium control and mitigation strategy is necessary. Several strategies have been proposed: tritium absorption using graphite [77], double-wall intermediate heat exchanger with tritium removal in the wall gap [52], cross-flow tritium removal facility [78], etc. One or more strategies can be adopted based on the specific conditions of the reactor.

2.3.6 Comparison of three candidate sites

A comparison of the key meteorological parameters and the calculation results of the three modeled locations are shown in Table 2.2. Among the three candidate sites for FHR construction,

the Idaho Falls site has the lowest annual average temperature and the highest wind speed, which help lower the radioactive dose that the public may receive. On the other hand, the Idaho Falls site has the lowest relative humidity, which leads to a higher individual dose. As a result of the combined effects of these key meteorological parameters and other factors, the Idaho Falls site has the highest maximum individual dose among these three sites, with the 60-m stack or 110-m stack alike. While the Hanford site has the lowest wind speed, medium temperature and relative humidity, the maximum individual dose at this location is the lowest among the three. The calculation results show that although the key parameters significantly affect the health impact of tritium release on the public, for a specific site, to evaluate the impact quantitatively, detailed calculation is necessary.

Table 2.2 Comparison of the three candidate sites

Site		Hanford	Idaho Falls	Oak Ridge
Annual average temperature [°C]		10.4	8.9	15.9
Annual average relative humidity [%]		60.3	55.0	71.0
Annual average wind speed [m/s]		3.5	5.1	4.9
Max. individual dose [mSv/y]	60-m stack	5.03	6.59	5.99
	110-m stack	2.61	2.90	2.83
Reduction due to stack height increase [%]		48.1	56.0	52.8

2.4 Results of dose equivalent prediction based on forward uncertainty propagation

In this study, it is assumed that the meteorological parameter temperature is a random variable following a uniform distribution, while wind speed and humidity are random variables following normal distributions. The distributions are determined by observing the historical meteorological data of the three sites. Take the Oak Ridge site as an example to illustrate the process. The historical annual average temperature of the Hanford site is plotted in Figure 2.19. It can be observed clearly that the temperature has been rising from the year 1960. Therefore, it is reasonable to assume the temperature would follow this trend. We picked the high and low peaks of temperature from 1990 to 2018, and drew two linear regression lines. The two bounds are extrapolated into the near future to serve as the upper and lower bounds of the temperature variation range. In addition, from the pattern of historical data, temperatures scatter uniformly in the range. Therefore, we also assume

that temperature follows a uniform distribution with the variation range bounded by the extrapolated upper and lower bounds.

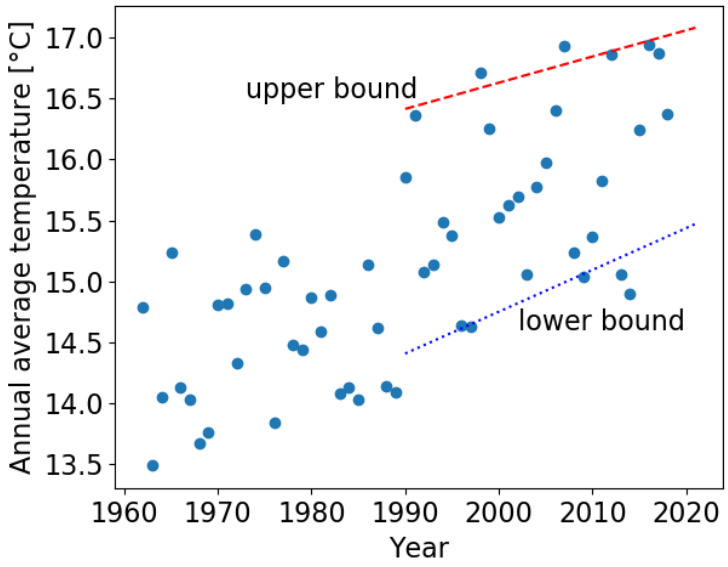

Figure 2.19 Historical temperature (Oak Ridge site)

For wind speed and humidity, the scatter plots and the histogram plots suggest normal distribution during the past decades, as indicated in Figure 2.20 to Figure 2.23. Data for the humidity is only available from 1960 to 1990. However, very little change has occurred in humidity from 1930 to 2010 [79]. Therefore, we assume the same distributions would continue into the near future.

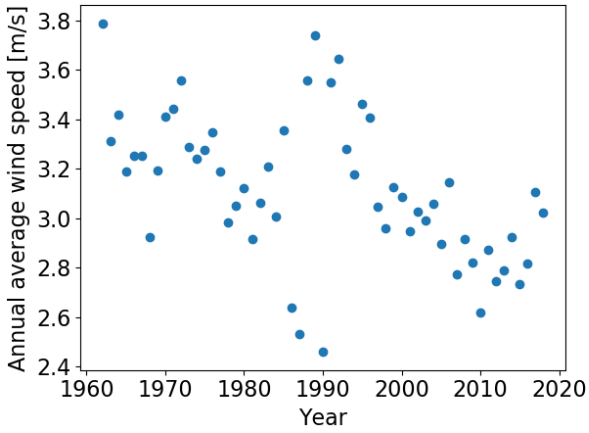

Figure 2.20 Scatter plot of historical wind speed (Oak Ridge site)

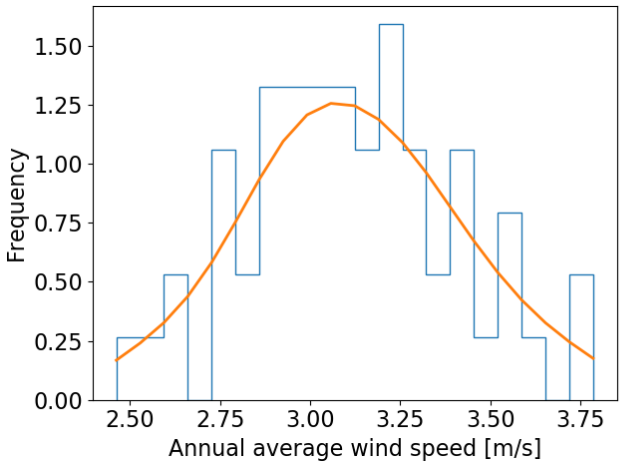

Figure 2.21 Histogram of historical wind speed (Oak Ridge site)

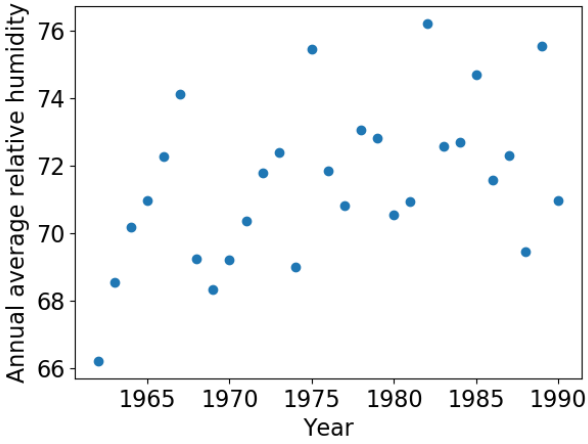

Figure 2.22 Scatter plot of historical humidity (Oak Ridge site)

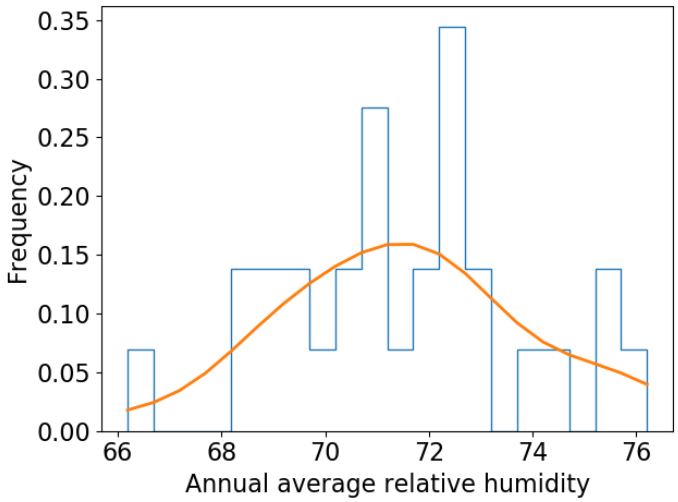

Figure 2.23 Histogram of historical humidity (Oak Ridge site)

The key parameters of the distributions are listed in Table 2.3. For each site, 125 samples are drawn from the distributions using the Latin Hypercube Sampling technique, and the corresponding maximum individual doses are calculated to be used for the training of the Gaussian process model [80]. The marginal distributions of the three variables and their pairwise joint distributions are plotted in Figure 2.24–Figure 2.26. It can be observed that no obvious correlations exit between these three parameters. The Sobol indices analysis confirms that no interaction exists between the variables because the difference between total Sobol and the first-order indices are minimal, as indicated in Table 2.4. The first-order Sobol indices are also displayed visually in Figure 2.27 for direct comparison. For different sites, the significance of a certain meteorological parameter changes dramatically.

Table 2.3 Ranges of input meteorological parameters

	Temperature [°C]	Wind speed [m/s]		Relative humidity [%]	
	Range	Mean	Standard deviation	Mean	Standard deviation
Hanford	[10.82, 13.03]	2.70	0.274	60.73	2.737
Idaho Falls	[8.49, 9.54]	4.54	0.409	57.69	3.090
Oak Ridge	[15.44, 17.06]	3.13	0.305	71.53	2.303

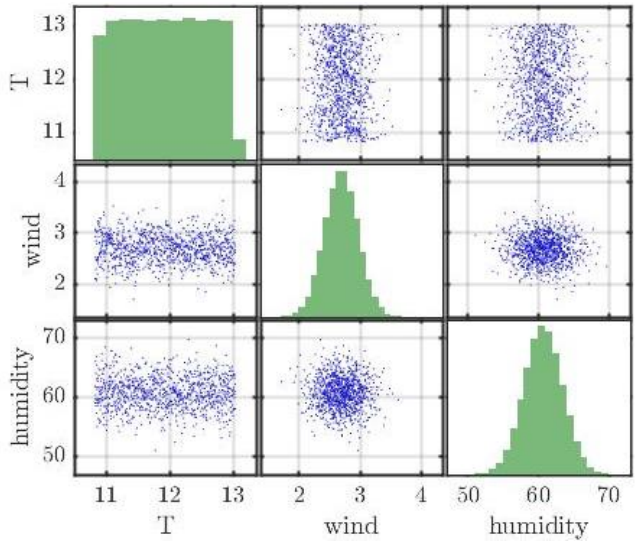

Figure 2.24 Distribution of input meteorological parameters (Hanford site)

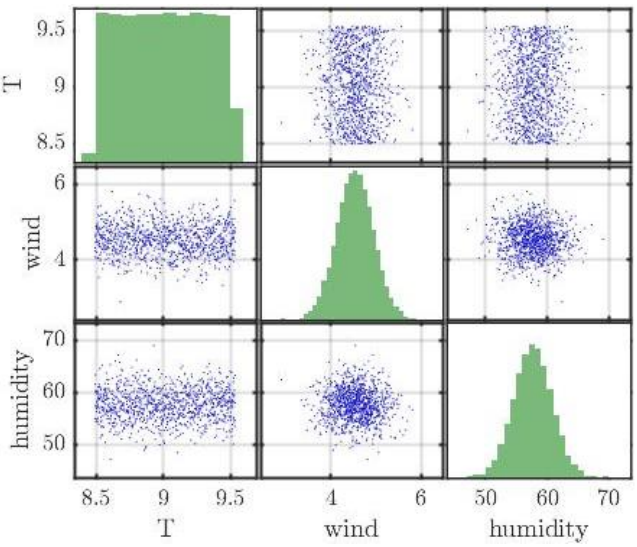

Figure 2.25 Distribution of input meteorological parameters (Idaho Falls site)

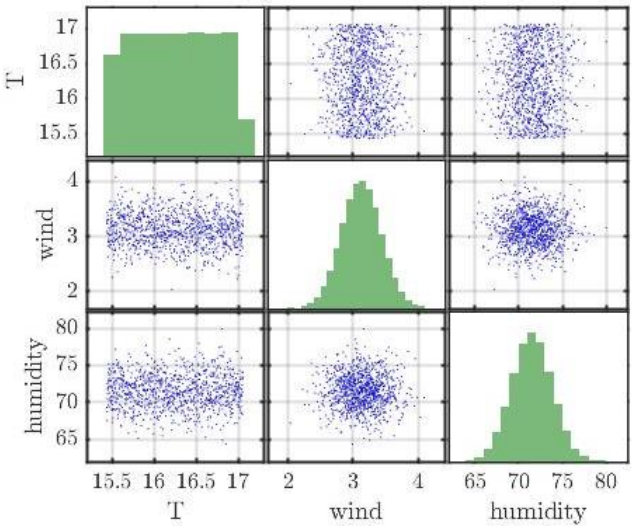

Figure 2.26 Distribution of input meteorological parameters (Oak Ridge site)

Table 2.4 Sobol indices of meteorological parameters on dose assessment

Parameter	Hanford site		Idaho Falls site		Oak Ridge site	
	First-order	Total	First-order	Total	First-order	Total
Temperature	0.0225	0.0274	0.0145	0.0148	0.3565	0.3512
Wind speed	0.9256	0.9341	0.7404	0.7559	0.1390	0.1346
Humidity	0.0426	0.0483	0.2283	0.2386	0.5156	0.5112

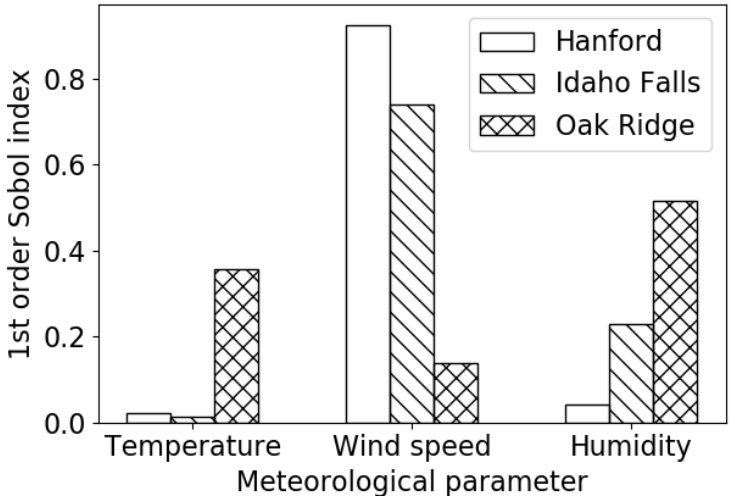

Figure 2.27 Comparison of first-order Sobol indices

As stated above, for different locations, the contributions of the meteorological parameters on the dose differ significantly. Wind speed is the dominant factor at the Hanford site and the Idaho Falls site, while it contributes less than 14% at the Oak Ridge site. The factor that dominates at the Oak Ridge site is humidity. Besides humidity, temperature also contributes more than 35% to the prediction. At the Idaho Falls site, the second significant factor that influences the dose assessment is the humidity.

For the three sites investigated, the maximum individual doses from chronic tritium release in the near future are predicted. The year 2020 is selected as the time frame of the evaluation of dose equivalent from chronic tritium release. The probability distributions of the predictions are shown in Figure 2.28–Figure 2.30. The probability distributions of the maximum individual dose at the three sites differ significantly. For the Hanford site, the most probable dose falls between 0.42 and 0.43 mSv range, while for the Idaho Falls site, the most probable range is from 0.33 to 0.35 mSv, and for the Oak Ridge site, it is from 0.26 to 0.27 mSv.

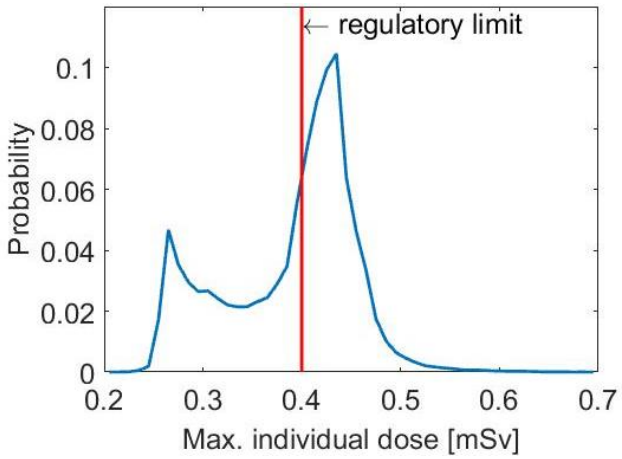

Figure 2.28 Dose equivalent prediction for 2020 (Hanford site)

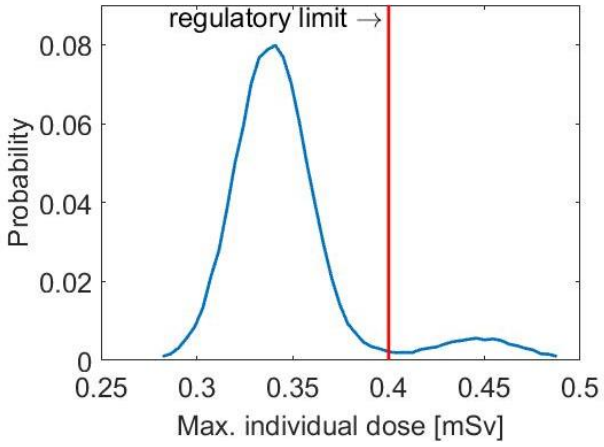

Figure 2.29 Dose equivalent prediction for 2020 (Idaho Falls site)

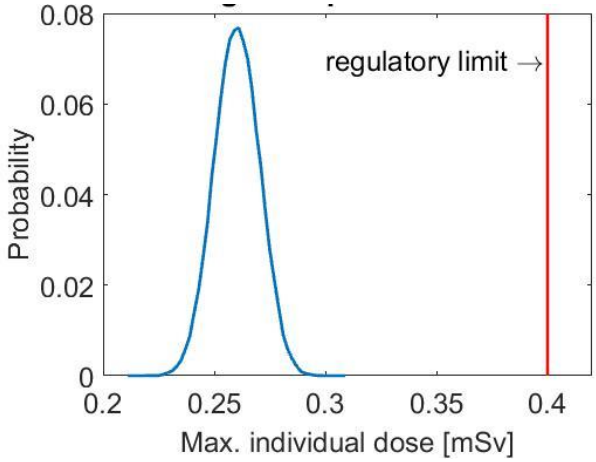

Figure 2.30 Dose equivalent prediction for 2020 (Oak Ridge site)

The probability distribution of the Hanford site shows two peaks, the major one at 0.42 mSv and the smaller one at 0.28 mSv. Taking Sobol indices into account, because the wind speed absolutely dominates, the mean value of the wind speed caused the major peak. The smaller peak on the left, however, results from accumulation of corresponding dose calculation results of wind speeds higher than the mean value. The mean value of wind speed for the Hanford site equals 79% relative wind speed in Figure 2.15. As the wind speed increases to above the mean value, the resulting maximum individual dose does not show an obvious decrease. In the uncertainty analysis, samples with wind speeds in this range lead to a similar dose assessment, causing an accumulated peak to appear. Because wind speed is of a normal distribution, the number of these samples is of a

relatively small percentage, causing the accumulated peak to be a secondary one, lower than the major peak.

In Figure 2.29, similar to what is observed in the Hanford site prediction, a small peak appears to the right-hand side of the major peak. For the Idaho Falls site, wind speed dominates with a 0.74 Sobol index. The major peak represents the mean value of the wind speed distribution, which corresponds to 90% relative wind speed in Figure 2.15. The magnitude of the smaller peak is only 1/8 of the main peak and is probably caused by the underlying correlation between wind speed and humidity, which contributes 23% to the prediction results.

The probability distribution of prediction for the Oak Ridge site follows a normal distribution. This is within expectation, because the two most significant influential parameters, humidity and temperature, are of normal distribution and uniform distribution, respectively.

From the linear relationship between tritium release rate and dose equivalent, it can easily be observed that for the Oak Ridge site, the probability that an individual receives dose higher than the regulated 0.4 mSv/y is extremely low. For the Idaho Falls site, the probability that the maximum dose that an individual receives does not exceed the limit is 91.62%, while for the Hanford site, the probability is only 44.27%. The results present some disagreement with the results obtained for the year 1990, as listed in Table 2.2, where the Hanford site would be the most suitable location for FHR construction, considering the radioactive impacts to the public. Because the meteorological parameters vary and the climate changes generally with time, the resulting appropriateness of the same candidate location could alter as well.

From the linearity of the effects of tritium release rates on the dose equivalent, and combining the probability distributions of dose equivalent prediction, we can try to propose the maximum tritium release rates required to meet the regulatory limit for the three investigated sites. With a 95% confidence interval, and the height of the tritium release point set at 110 m, the tritium release limits are listed in Table 2.5.

Table 2.5 Tritium release limit for FHRs based on prediction

Site	Max. tritium release rate [TBq/day]
Hanford	15.75
Idaho Falls	16.92
Oak Ridge	26.74

2.5 Conclusions on the tritium dispersion modeling

In this part of the study, to evaluate the potential health impact of the released tritium to the public residing near the FHR site, modeling of chronic airborne tritium release was performed for three different locations: Hanford site, Idaho Falls site, and Oak Ridge site. The maximum annual dose that an individual would receive from the tritium release was calculated. Parametric studies of crucial meteorological and geometric parameters, i.e., temperature, wind speed, humidity, and height of the release point were carried out. It is discovered that to lower the public health impact from FHR tritium release, we should choose a location that has the climate of low temperature, high wind speed, high relative humidity, and set a high release point. In addition, the calculations using various tritium release rates show that the maximum individual dose has a linear relationship with the release rate. This linearity can be applied conveniently to the startup period and situations with different tritium release rates.

From a comparison of the three calculated potential FHR construction locations, it is discovered that based on the climate of 1990, under the same tritium release rate and with the same release point height, the Hanford site has the lowest health impact on the surrounding residents among the three sites. However, a prediction of the dose equivalent of the year 2020 and the corresponding uncertainty analysis show that in the near future, residents near the Oak Ridge site will have the lowest probability to exceed the regulated annual radioactive dose limit. Therefore, dose assessment for the future should include the effects of climate change, and uncertainty analysis should be performed to address the significant uncertainties in meteorological parameters. It is also discovered that for different geological locations, the dominance of meteorological parameters differs significantly.

Measures to keep the tritium release rate within the limits include: select a location with a favorable climate (i.e., features low temperature, high wind speed or high humidity), increase the height of the tritium release point, and adopt a tritium control strategy in the reactor system.

Chapter 3. Tritium Control and Mitigation Strategies

From the calculation of the potential health impact of released tritium, control of the tritium release rate from FHRs is necessary. The upper limit of the release rate varies for each FHR construction site due to different climates and topographies. This chapter introduces a tritium control and mitigation system proposed for tritium management in FHRs. The design work of the system was completed in an earlier study by the author [53]. Therefore, in this dissertation, the system and the key component of the system, i.e., the cross-flow tritium removal facility are only concisely described without further technical details. The proposed cross-flow tritium removal facility was compared with the double-wall heat exchanger design, which is another strategy for tritium removal in FHRs. An economic analysis was performed to show the cost advantages of the proposed system with the cross-flow tritium removal facility.

In this study, the permeation window extraction facility is selected as the prototype for a tritium control system design because this strategy brings some advantages compared with the countercurrent extraction tower:

1. The permeation window extraction facility can be part of the intermediate heat exchanger. This reduces the amount of design work;
2. The sweep gas is not mixed or physically in contact with the molten salt. Separate flow is more advantageous than mixed flow in the aspect of flow control;
3. The amount of helium that dissolves in the molten salt can be reduced if the material of fabrication for the permeation wall is properly selected. The permeation window material is expected to have selective permeation properties that enable T_2 to transport while allowing a negligible amount of helium to permeate through.

3.1 Tritium control and mitigation system for FHR systems

Based on the behavior of tritium in FHR systems and the principles of the permeation window extraction facility, we designed a tritium control and mitigation system. The system consists of a redox control station, a tritium removal facility, and an optional double-wall IHX with tritium permeation barrier, as shown in Figure 3.1. In addition, the tritium removal facility has an additional loop to collect tritium in the purging gas, which extracts tritium from the primary coolant. In the redox control station, beryllium is used as the redox agent since it is an original component of the primary coolant FLiBe and it possesses favorable neutronic properties.

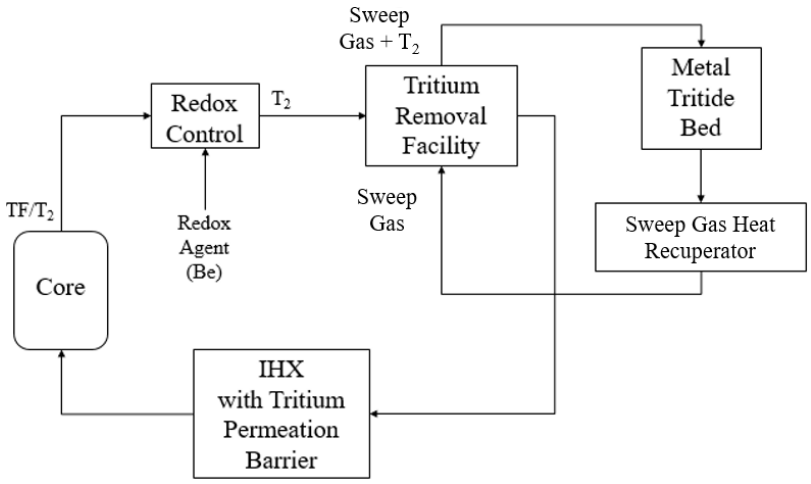

Figure 3.1 Schematic of the tritium control and mitigation system

The tritium removal facility locates downstream of the outlet of the core, and extracts T_2 out of the primary coolant. The underlying principles for designing such a tritium removal facility are:

1. To increase the mass transfer area to volume ratio;
2. To increase the turbulence of the molten salt flow, so that the gradient of T_2 concentration from the center of the flow channel to the diffusion boundary can be flattened, reducing the diffusion resistance of T_2 in the molten salt.

3.2 Design of the cross-flow tritium removal facility

The finalized cross-flow tritium removal facility is shown in Figure 3.2. In this drawing, only a quarter of the whole tube bank is presented in the front left corner, while in the real facility the tube bank occupies the entire space of the facility. It is designed with a modular concept in mind, to meet different demands of tritium removal rates in FHRs of different power levels. Multiple modules can be bolted together in a row, increasing the total active length of tritium removal area, or they can be bolted side by side to the main pipe, splitting the molten salt flow, as shown in Figure 3.3.

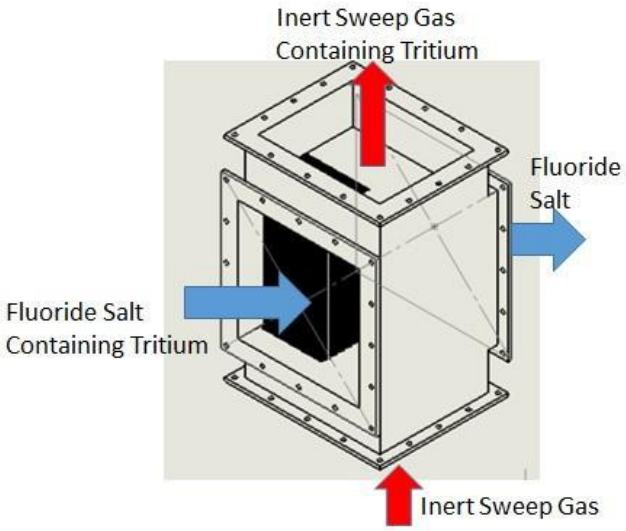

Figure 3.2 Cross-flow tritium removal facility

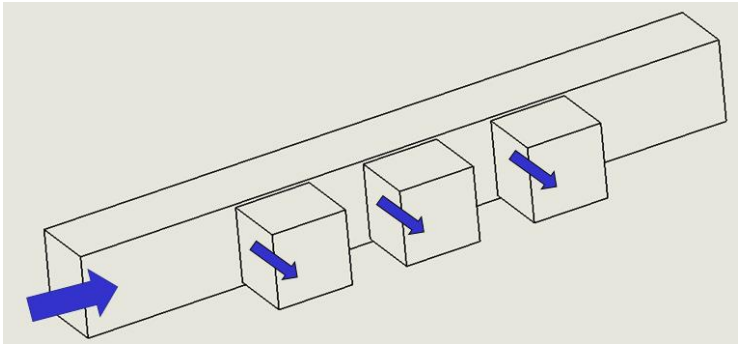

Figure 3.3 Tritium removal modular facilities connected to a main pipe

During the design process of the tritium removal facility, several design concepts were modeled using computational simulation tools, COMSOL Multiphysics and MATLAB. These concepts include but not limit to: bubble column, packed bed scrubber, printed circuit heat exchanger with fins, wavy plate heat exchanger, and cross-flow tube bank. The schematic of each design concept is demonstrated in Figure 3.4.

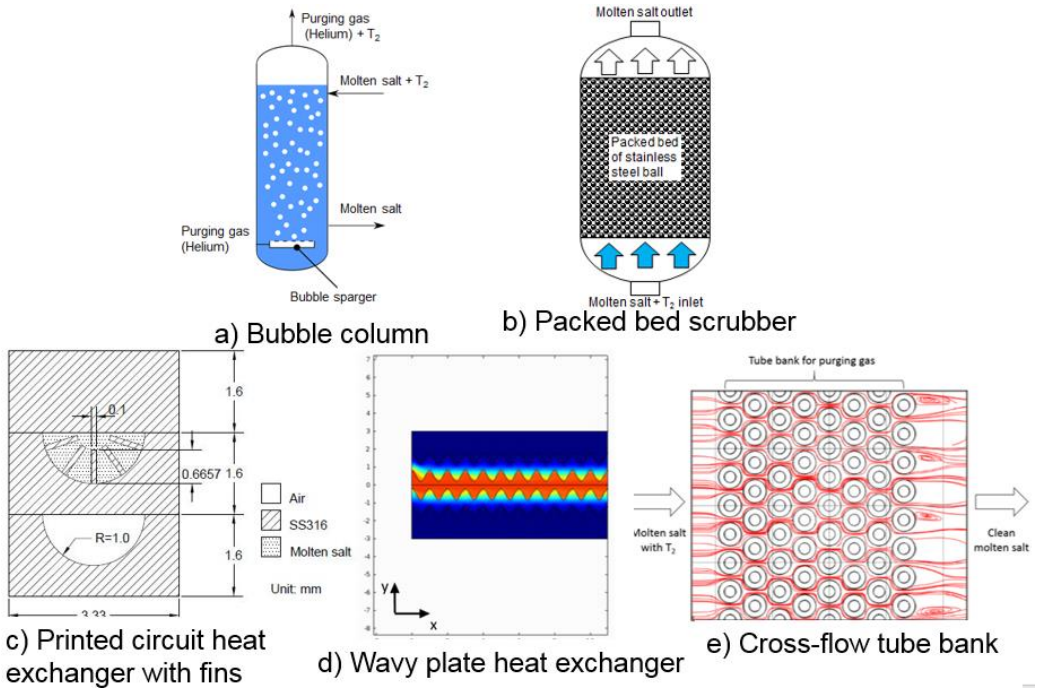

Figure 3.4 Design concepts of the tritium removal facility

The simulation results are listed in Table 3.1. The values in this table are normalized based on the values of the cross-flow tube bank for direct comparison. We discovered that the cross-flow tube bank design possessed the potential of the highest tritium removal efficiency, and therefore, we designed the tritium removal facility using this design concept.

Table 3.1 Comparison of tritium removal facility design concepts simulation results

Design concept	Mass transfer surface per unit volume	Molten salt inlet cross-section area	Molten salt frontal velocity	Total molten salt flow length	Advantages	Drawbacks
Bubble column (with helium)	0.51	0.5	2	5.88	Non-complicated post processing	Not feasible to keep a sufficiently high bubble volume fraction
Stainless steel packed bed scrubber	0.30	0.79	70	64.71	Mature industry of packed bed reactors	Low efficiency of tritium removal; Large dimensions
Finned plate heat exchanger	0.63	1	1	88.24	Mature industry of finned plate heat exchangers	Low efficiency of tritium removal; Large dimensions
Wavy plate heat exchanger	0.60	1	1	1.12	Relatively high tritium removal efficiency	Large dimensions
Cross-flow tube bank	1	1	1	1	Relatively high tritium removal efficiency	High molten salt pressure drop

A variety of dimension sets were proposed for the cross-flow tritium removal facility. Calculations were carried out to study their tritium removal performance and molten salt pressure drop. Among the total 25 models that have been calculated, two cases where the best results in both mass transfer performance and pressure drop are selected, as listed in Table 3.2. The total mass flow rate of the molten salt and the tritium inlet concentration used in the calculation are from the pre-conceptual design of the Advanced High-Temperature Reactor (AHTR) [3].

Table 3.2 Configurations of the tritium removal facility

Items	Unit	Design A	Design B
Total mass flow rate of molten salt	kg/s	11190.8	
Tritium concentration in inlet molten salt	mol/m^3	1.8×10^{-6}	
Tritium concentration in outlet molten salt	mol/m^3	1.69×10^{-6}	
Objective tritium removal rate	$mol/(m^3\text{-}s)$	7.2×10^{-8}	
Tube outer diameter	mm	26.67	33.40
Tube inner diameter	mm	20.93	26.64
Tube wall thickness	mm	2.87	3.38
Tube bank pitch	mm	33.27	41.66
Number of tubes	–	292	177
Molten salt inlet frontal velocity	m/s	1	1
Number of modules required	–	10	15

In the finalized designs, the tritium concentration in the primary coolant is intentionally raised to 10 times its production rate (1.8×10^{-7} $mol/(m^3\text{-}s)$). As a result, the tritium concentration difference between the primary coolant and the purging gas is raised, which leads to a larger mass transfer driving force. In summary, the designed cross-flow tritium removal facility characterizes a large ratio of mass transfer area over volume, a highly turbulent molten salt flow, and a large gradient of the tritium concentration.

3.3 Double-wall IHX with tritium permeation barrier

An alternative tritium removal strategy is to use a double-wall heat exchanger in the primary loop with the tritium permeation barrier filled in tube gaps [52]. This strategy combines heat transfer and tritium control into one single component, and no separate tritium control facility is needed.

Figure 3.5 shows a design of the double-wall Natural Draft Heat Exchanger (NDHX) to be used in the DRACS loops. The molten salt coolant flows on the tube side of the inner tube, air flows on the shell side of the outer tube, and in between the inner and outer tubes flows the tritium removal fluid (helium in this design). Tritium dissolved in the molten salt permeates through the inner tube wall and is carried away by the flowing helium. Four different tube configurations are proposed [81]:

1. Inner plain tube + outer plain tube;
2. Inner plain tube + outer fluted tube;
3. Inner fluted tube + outer plain tube;
4. Inner fluted tube + outer fluted tube.

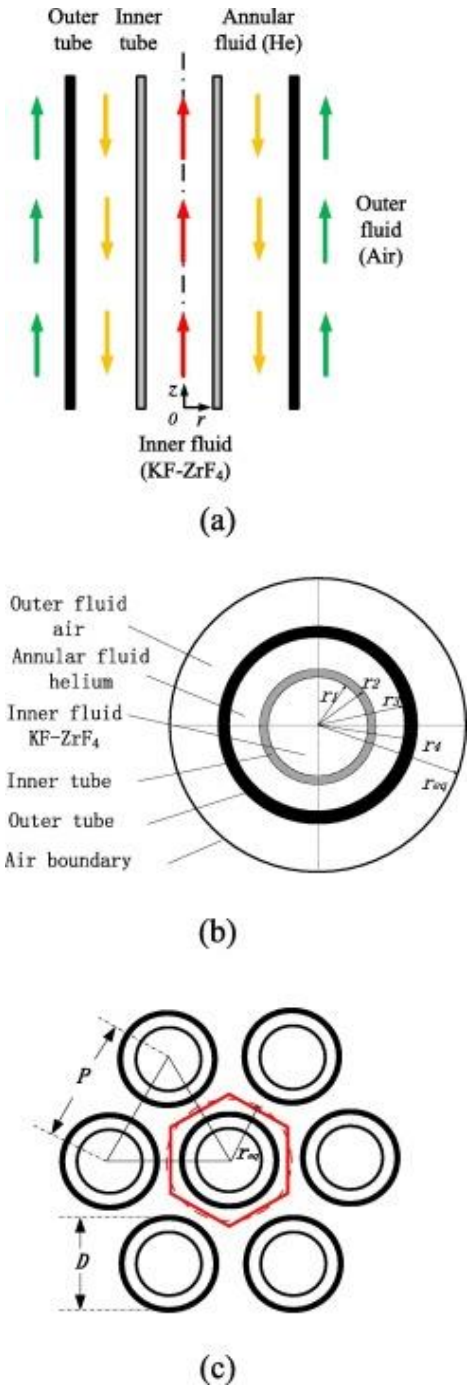

Figure 3.5 Design of the double-wall NDHX [81]

As a heat exchanger, both its heat transfer performance and tritium removal performance need to be evaluated. The NDHX is designed for 8.5 MW heat load. Optimization of the heat exchanger

design parameters is performed. The optimized design achieves 95% heat transfer and 65% tritium removal.

The tritium removal facility and the double-wall heat exchanger can also be combined in the primary loop. A double-wall IHX can be located after the tritium removal facility. Because of the high level of tritium concentration in the primary coolant, a tritium diffusion barrier might be necessary to prevent tritium from leaking into the secondary loop through the IHX tubes. The barrier must be located between the primary loop and the secondary loop, which means that the barrier would also participate in the heat transfer. Similar to the NDHX introduced above, in designing and optimizing the IHX with tritium permeation barrier, heat transfer resistance added to the IHX due to the added barrier need to be balanced with the tritium permeation reduction performance.

The tube configuration of the IHX can be the first choice, inner plain tube + outer plain tube. A single tube unit is shown in Figure 3.6. Primary coolant flows inside Tube 1. Right outside each tube, there is a concentric tube (Tube 2) which sandwiches the tritium permeation barrier between itself and the primary side tube (Tube 1). The secondary coolant flows in the gap between Tube 2 and Tube 3.

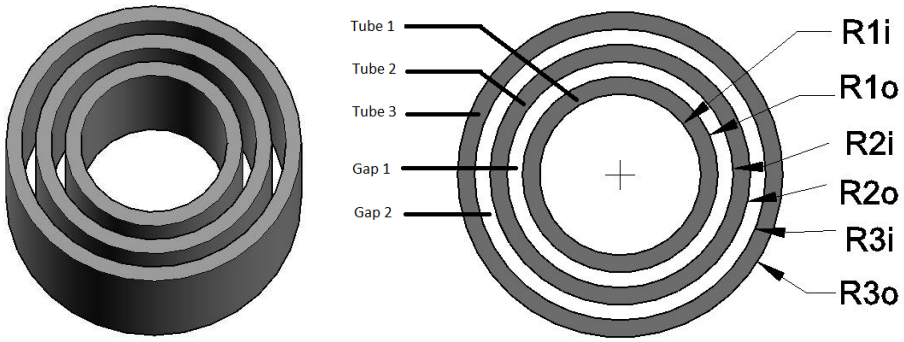

Figure 3.6 Intermediate heat exchanger with tritium permeation barrier

From the tritium transport coefficients in molten salts, it can be observed that molten salts are good tritium diffusion barriers. Therefore, FLiNaK, which has a lower tritium diffusion coefficient than

FLiBe, can be used as the tritium permeation barrier. FLiNaK is designed to flow at a very low speed, for instance, 1/10 of the FLiBe flow rate. The design parameters are listed in Table 3.3. An intermediate heat exchanger using molten salt as the tritium permeation barrier will have a similar structure as is shown in Figure 3.7.

Table 3.3 Primary parameters of the IHX with barrier

Inner radius of Tube 1 (R1i) [mm]	12.7	Outer radius of Tube 1 (R1o) [mm]	13.4
Tube wall thickness [mm]	0.737	Gap 2 thickness [mm]	6.35
Barrier thickness [mm]	~ 1	FLiNaK barrier flow rate [m/s]	0.05
Primary coolant flow rate [m/s]	0.5	Secondary coolant flow rate [m/s]	0.5

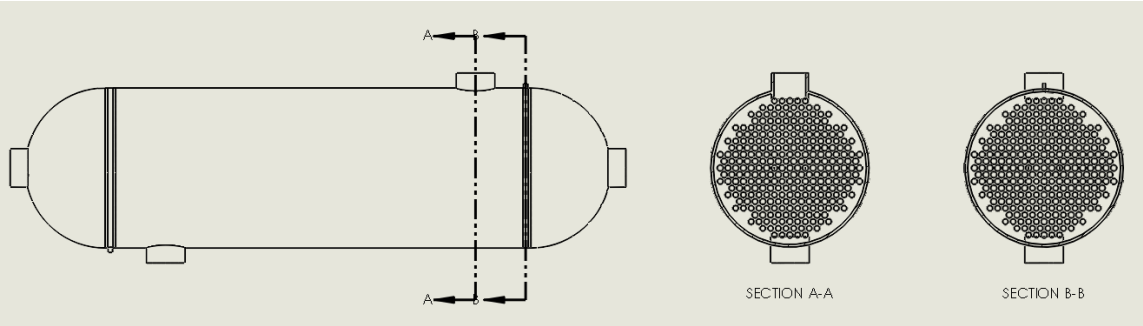

Figure 3.7 Structure of an IHX using molten salt as tritium permeation barrier

Another option for the sandwiched tritium permeation barrier in the intermediate heat exchanger is Al_2O_3, which is widely studied as a promising tritium permeation barrier material. The only difference in this design compared with the one above is that FLiNaK is replaced by Al_2O_3. According to the literature, a major application of Al_2O_3 is to apply it as a coating on surfaces. However, one of the major challenges with Al_2O_3 coating is that it is difficult to produce uniform coating without defects. Defects in the coating greatly reduces its effectiveness as a tritium permeation barrier. In addition, the coating cracks under irradiation and corrosion, which again reduces its permeation reduction performance significantly.

Al_2O_3 has a higher thermal conductivity compared to FLiNaK. The thermal conductivity of FLiNaK is around 1 W/(m-K), while that of Al_2O_3 is around 30 W/(m-K). Therefore, the heat

transfer performance should be better with the Al_2O_3 barrier, if both barriers are of the same thickness.

The current concern of the Al_2O_3 design is that the barrier may reach saturation at a certain time length after the operation starts. Unlike FLiNaK or other types of molten salt tritium permeation barriers which can flow and get cleaned up, the Al_2O_3 barrier is expected to last long before getting replaced. It still remains to be examined whether Al_2O_3 can still act as satisfactory tritium permeation barriers in an intermediate heat exchanger, even when it is saturated with tritium. In addition, the integrity of the barrier is a key factor in the tritium permeation reduction performance of the Al_2O_3 barrier. Under the high temperature gradient in the IHX, it is highly possible that the barrier will develop cracks that degrade the tritium permeation reduction performance.

3.4 Economic assessment

An economic assessment was conducted to evaluate the costs of the two tritium control strategies, i.e., the tritium removal facility and the double-wall heat exchanger. In addition, the costs of the three-loop and two-loop FHR systems were also compared to verify the economic advantages that the two-loop FHR design holds over the three-loop design.

3.4.1 Cost analysis of the cross-flow tritium removal facility

Because the cross-flow tritium removal facility has the geometry of a cross-flow heat exchanger, its cost can be calculated using the methods developed for heat exchanger cost evaluation. Therefore, for both the cross-flow tritium removal facility and the double-wall heat exchanger, a cost evaluation model developed by Taal et al. [82] is used. The total cost includes capital cost and operating cost, which are calculated separately. The capital cost includes both material cost and fabrication cost. For the operating cost, a base cost is calculated, and each year's operating cost is obtained by applying operating time-related factors and inflation factors to the base cost.

The operating cost is calculated for a time span of 10 years with a 2% inflation rate per year considered. The annual inflation rate is estimated using the average values during the past 10 years,

as shown in Table 3.4. The annual inflation rate each year is calculated using the monthly Consumer Price Index published by the Bureau of Labor Statistics (BLS) [83].

Table 3.4 Annual inflation rate 2006 – 2015 [83]

Year	Annual inflationrate [%]
2006	3.2
2007	2.8
2008	3.8
2009	-0.4
2010	1.6
2011	3.2
2012	2.1
2013	1.5
2014	1.6
2015	0.1
Average	2.15

The capital cost is affected by several parameters, including geometry, material, pressure, and annual inflation rate. Each heat exchanger has a fixed cost related to the total heat transfer surface area. For the tritium removal facility, it is the mass transfer surface area. The fixed cost C_b in UDS is calculated by:

$$C_b = \exp\left[8.202 + 0.01506\log A + 0.06811\left(\log A\right)^2\right], \tag{3.1}$$

where *A* is the total heat transfer surface area in the heat exchanger, m.

The fabrication cost of a heat exchanger is related to the type of heat exchanger built. The tritium removal facility resembles a fixed head heat exchanger, of which the fabrication cost factor F_d is expressed as:

$$F_d = \exp\left(-0.9003 + 0.0906\log A\right). \tag{3.2}$$

The pump work to compensate for the pressure drop varies with different pressure drop range, as listed in Table 3.5.

Table 3.5 Expressions of pressure cost

Operating pressure range [kPa]	Pressure cost expression
700 – 2100	$F_p = 0.8955 + 0.04981 \log A$
2100 – 4200	$F_p = 1.2002 + 0.0714 \log A$
4200 – 6200	$F_p = 1.4272 + 0.12088 \log A$

In the original model developed by Taal et al. [82], several common materials for heat exchanger fabrication are investigated. The material cost for each material is shown in Table 3.6.

Table 3.6 Expressions of material cost in the year 2003

Material	Material cost expression
Stainless steel 316	$F_m = 1.4144 + 0.23296 \log A$
Incoloy 600	$F_m = 2.4103 + 0.50764 \log A$
Incoloy 825	$F_m = 2.3665 + 0.49706 \log A$
Hastelloy	$F_m = 3.7614 + 1.51774 \log A$

For the evaluation of the cross-flow tritium removal facility, the construction material is stainless steel 316H. To calculate the material cost, an adjustment is made by multiplying the ratio of average market prices of two materials at two years, i.e., 2003 and 2016. Take stainless steel 316H for example, which is used in the tritium removal facility for current research, the stainless steel 316/316L surcharge is as shown in Table 3.7 when the model was first used in 2003. The average price of stainless steel 316/316L in 2003 and 2016 has a ratio of 0.60. This ratio is also taken into consideration because it could potentially represent the market price change of the main structural material of the tritium removal facility.

Table 3.7 Historical surcharge of stainless steel 316/316L [84]

Month	Year 2003	Year 2016
1	0.1583	0.4112
2	0.1556	0.4155
3	0.2097	0.4003
4	0.2525	0.4190
5	0.2608	0.4333
6	0.2377	0.4918
7	0.2804	0.5090
8	0.3198	0.5427
9	0.3109	0.5819
10	0.3552	0.5433
11	0.3970	0.0000
12	0.4526	0.0000
Average	0.28	0.47

The economy situation varies from year to year. So, a time factor is also added to the cost to take inflation into account. The annual inflation rate which is calculated before is adopted as the estimated time factor [83].

$$F_{yr} = 1.02 . \tag{3.3}$$

The total capital cost is:

$$C_{capital} = C_b F_d F_p F_m F_{yr} . \tag{3.4}$$

The energy cost C_E is required for the calculation of the operating cost. An estimated average market electricity cost of 10 cent/kWh is adopted [85].

$$C_E = 0.1 . \tag{3.5}$$

The pumping power is a major contribution to the operating cost. It is estimated using the following equation:

$$P = \frac{1}{\eta}\frac{\dot{m}}{\rho}\Delta p\,, \tag{3.6}$$

where

η is the pump efficiency, which is estimated to be 0.7 in this economic analysis;

$\dot{m}$ is the mass flow rate of molten salt on the shell side of the tritium removal facility;

ρ is the density of molten salt;

Δp is the pressure drop of molten salt flowing through the tritium removal facility.

Assuming the other costs are much smaller than the pumping power cost, the operating cost can be expressed as:

$$C_{operating} = PC_E H_{operation}\,, \tag{3.7}$$

where $H_{operation}$ is the number of operating hours per year. In this economic analysis, 7000 h/y is used.

The final total cost is the addition of the capital cost and the operating cost:

$$C_{total} = C_{capital} + C_{operating}\,. \tag{3.8}$$

A MATLAB code was written to calculate the cost of the tritium removal facility for 10 years. The results are listed in Table 3.8. The total cost is calculated for 10 years after construction. In this calculation, all primary salt flows through the tritium removal facility, which leads to a large facility tube number. The primary salt flow rate used is the same as that in the AHTR conceptual design [3].

Table 3.8 Cost of the tritium removal facility with full primary coolant flow

Fixed cost [$]	C_b	1.33×10^6
Fabrication cost factor	F_d	0.94
Pressure cost factor	F_p	1.35
Material cost factor	F_m	6.94
Yearly inflation factor	F_{yr}	1.02
Energy cost [$/kW-h]	C_E	0.1
Capital cost [$]	$C_{capital}$	1.19×10^7
Operating cost [$]	$C_{operating}$	1.14×10^6
Total cost (10 years) [$]	C_{total}	2.33×10^7

To make the tritium management more economically attractive, one practical method is to reduce the flow rate passing the tritium removal facility. Therefore, the facility size will consequently be reduced as well. If 10% of the total primary salt flow rate passes the tritium removal facility, the cost was calculated, as shown in Table 3.9 based on the above model. The total cost in 10 years after construction is also reduced to about 10% of the cost with 100% primary coolant flow. The tritium removal rate might be lower in the case of 10% flow rate compared with 100% flow rate if the tritium concentration level in the primary coolant is the same. This can be made up by raising the tritium concentration level in the primary loop, as discussed in previous sections.

Table 3.9 Cost of the tritium removal facility operating with 10% primary coolant flow rate

Fixed cost [$]	C_b	1.03×10^5
Fabrication cost	F_d	0.76
Pressure cost	F_p	1.24
Material cost	F_m	5.79
Yearly inflation factor	F_{yr}	1.02
Energy cost	C_E	0.1
Capital cost [USD]	$C_{capital}$	1.19×10^7
Operating cost [USD]	$C_{operating}$	1.14×10^5
Total cost (10 years) [USD]	C_{total}	1.20×10^7

The cost evaluation of a double-wall heat exchanger with tritium permeation barrier requires knowing the amount of barrier needed. The unit price of raw yttrium material, for instance, a highly efficient tritium getter, is $275/kg [86]. However, the estimation of the amount of yttrium required is complicated because the combination number of tritium to yttrium is subject to change with several factors, including temperature, pressure, and probably also the geometry of yttrium. The typical combination number is between 1 and 3. This makes the estimation difficult. For a conservative estimate, the combination number can be selected as 1, while 2 might be good for an average estimation.

The amount of yttrium required to absorb the permeated tritium is only one of the many factors that influence the total required amount. Because it is reasonable to assume not all tritium will be absorbed immediately upon contacting with yttrium, an additional diffusion factor should be applied. To date, there is limited research on the influence of absorbed tritium, i.e., the formation of yttrium hydride on the tritium absorption rate of yttrium. More research and investigation is needed for the estimation of yttrium amount in the double-wall heat exchanger.

While the cost of the double-wall heat exchanger cannot be readily evaluated, the cost of the double-wall heat exchanger with helium as the tritium permeation barrier can be calculated using the same model as the cross-flow tritium removal facility. The calculated cost is shown in the next section.

3.4.2 Cost comparison of tritium control strategies

In the AHTR preconceptual design, the cooling system consists of three loops: the primary loop containing FLiBe, the intermediate loop containing KF-ZrF_4 and the power cycle containing water. The function of the intermediate loop is to transfer heat from the primary loop to the power cycle, and isolate the power cycle from the reactor block. The cooling system is shown in Figure 3.8.

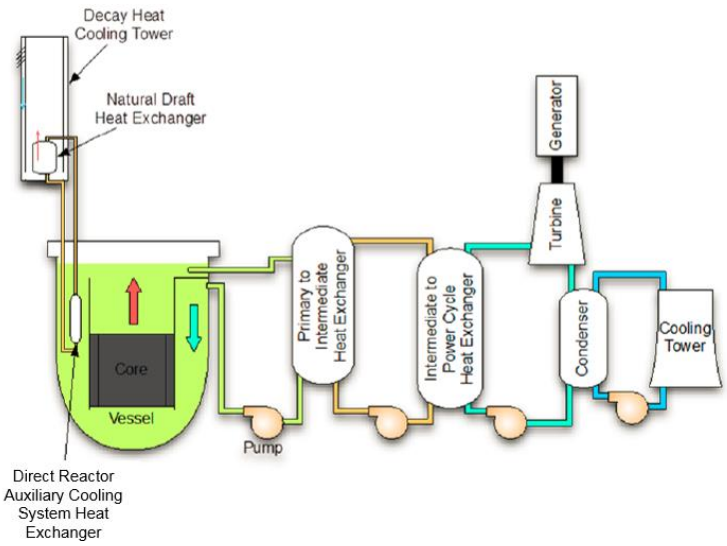

Figure 3.8 Cooling system of AHTR conceptual design [87]

With the tritium removal system designed for the primary loop, the function of the intermediate loop of preventing tritium from permeating into the power cycle is replaced. The intermediate loop can be eliminated for economic considerations. The primary loop will pass heat directly to the power cycle. The two-loop FHR design based on the AHTR conceptual design is shown in Figure 3.9.

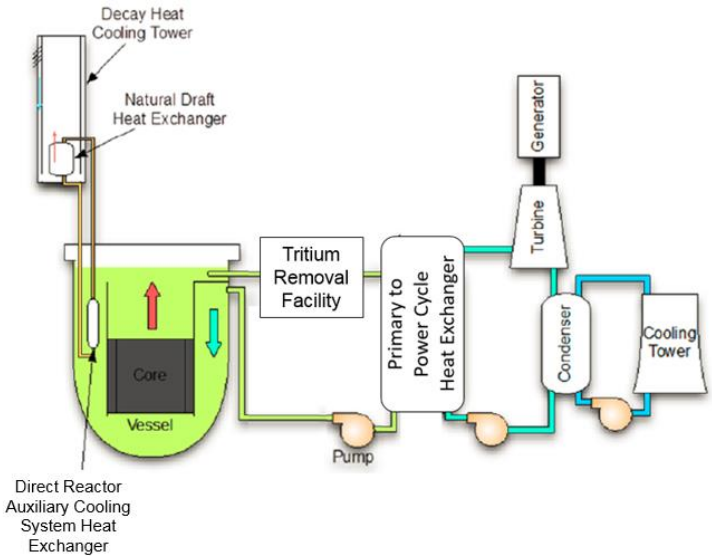

Figure 3.9 Two-loop FHR design

The strategies proposed for tritium control in a two-loop FHR system are as follows:

1. The tritium removal facility;
2. The double-wall heat exchanger [52];
3. The tritium removal facility and the double-wall heat exchanger;
4. The tritium removal facility and tritium-permeation-barrier coatings;
5. The double-wall heat exchanger and tritium-permeation-barrier coatings;
6. The tritium removal facility, the double-wall heat exchanger and tritium-permeation-barrier coatings.

The cross-flow tritium removal facility or the double-wall heat exchanger is the main facility in the tritium control system. It removes tritium from the system. Tritium-permeation-barrier coatings prevent tritium from permeating out of the system through structural materials. Coatings are necessary if the general tritium concentration in the primary loop is high. The higher the tritium concentration in the primary loop, the higher the removal rate that can be achieved in the main facility, but at the same time the higher the leakage rate from structural materials. Therefore, depending on the removal rate required and tritium concentration in the loop, one or more components can be incorporated in the tritium control system.

While the cost of the double-wall heat exchanger cannot be readily evaluated, the cost of the double-wall heat exchanger with helium as the tritium permeation barrier can be calculated using the same model as the cross-flow tritium removal facility.

The cost of each strategy is shown in Table 3.10. For the tritium-permeation-barrier coatings, Because the size of the AHTR loops is not available, the cost cannot be estimated. The cost of the double-wall heat exchanger is estimated using the double-wall NDHX. In the system, the intermediate heat exchanger is larger than the NDHX in size. Therefore, the cost of a double-wall intermediate heat exchanger is higher than a double wall NDHX listed in the table. From the comparison, strategy 1 is the most economical among the six strategies.

Table 3.10 Cost comparison of tritium control strategies

	Strategy	Capital cost [$M]
1	Tritium removal facility	11.9
2	Double-wall heat exchanger	36.6 [52]
3	Tritium removal facility + Double-wall heat exchanger	48.5
4	Tritium removal facility + Tritium-permeation-barrier coatings	11.9 plus cost of the tritium-permeation-barrier coatings
5	Double-wall heat exchanger + Tritium-permeation-barrier coatings	36.6 plus cost of the tritium-permeation-barrier coatings
6	Tritium removal facility + Double-wall heat exchanger + Tritium-permeation-barrier coatings	48.5 plus cost of the tritium-permeation-barrier coatings

Comparing the two-loop design to the original three-loop design, the former does not have the entire intermediate loop but has a tritium removal facility installed on the primary loop. An economic analysis is carried out to investigate whether the two-loop design is of advantages in the aspect of construction and operation cost.

The reference design of FHR in this project is the AHTR pre-conceptual design. Because this design is still in its early stage, not all the details have been determined. The size of the coolant loops, geometry or dimensions of the components, pumping power, etc. are not available yet. The available parameters of the intermediate loops in the AHTR pre-conceptual design are listed in Table 3.11 [87].

Table 3.11 Intermediate salt loops parameters

Parameter	Unit	Value
Salt material	-	$KF\text{-}ZrF_4$
Supply temperature	°C	675
Return temperature	°C	600
Flow rate	kg/s	43200
Pressure	-	Atmospheric
Number of loops	-	3
Pipe wall material	-	Hastelloy N

Because of the lack of design details, the following assumptions are made in the current economic analysis:

1. The amount of heat transfer fluids in the primary loops and the power cycle is the same in both the three-loop design and the two-loop design;
2. The cost of the heat exchanger between the primary loop and the power cycle in the two-loop design equals half of the cost of the two heat exchangers in the three-loop design. By reducing the intermediate loops, the cost of loop-coupling heat exchangers is reduced to half;
3. The cost of the main facility in the tritium control system equals the cost of a heat exchanger in the intermediate loop.

With the above assumptions, the main differences between the two designs are listed in Table 3.12. Because of the lack of the entire intermediate loop, the cost of the two-loop design does not include the salt, pump, piping of the intermediate loop. In addition, the two heat exchangers that are required in the three-loop design can be reduced to one in the two-loop design. The two-loop design has the cost of tritium removal facility which is not included in the original three-loop design.

Table 3.12 Main differences between the two-loop and three-loop FHR designs

FHR design	Two-loop design	Three-loop design
Components	Tritium control system	Intermediate loops piping
		Intermediate loops pumps
		Intermediate loops salt ($KF\text{-}ZrF_4$)
		Intermediate to power cycle heat exchanger

The main component of the tritium control system is the tritium removal facility or the double-wall heat exchanger. If the assumption that the cost of the main facility equals a heat exchanger is applied, then compared with the two-loop design, the three-loop design has the additional cost of the piping, pumps and salt. For the piping and the salt, it is mainly the construction cost. The cost of maintenance is relatively low. For the pumps, both the construction and the operation cost are major parts of the total cost. Therefore, both the construction and the operation cost of the three-loop design are higher than those of the two-loop design. The two-loop design FHR without the intermediate loop offers economic advantages compared with the original three-loop design.

Chapter 4. Development of a Tritium Analysis Code and Code Verification

In this chapter introduces the development of a novel mass transfer calculation method based on the LMSPD. A computer code realizing this method was validated against hydrogen permeation experimental data. This chapter also presents the design and carrying-out of the experiments intended for the evaluation of the effectiveness and efficiency of the cross-flow tritium removal facility.

To evaluate further the tritium-removal efficiency of the designed cross-flow tritium removal facility, the development of a tritium analysis code is necessary. Because of the similarity of mass transport and heat transfer, heat-transfer calculation methods were reviewed. In a heat-transfer calculation, two types of methods are commonly used: One is to divide the volume into meshes and solve for each mesh; the other is to use a 0-D, "black-box" method based on a mean temperature difference. The former can be applied to mass transfer calculation directly, but the latter needs some modification—especially when calculating interphase gas diffusion.

The two-film theory for interphase mass transfer shows that concentration can "jump" at the interface of two materials, but the partial pressure is continuous [88]. Therefore, the variable that corresponds to temperature is the partial pressure of the diffusing species. Then the logarithmic mean temperature difference (LMTD) should be modified to the LMSPD.

Calculation of diatomic gas diffusion across a metal and nonmetal interphase is a specially complicated situation if the 0-D method is used. This difficulty mainly comes from the solubility. Henry's law shows that solubility is proportional to the partial pressure of the solute gas, if the solvent is salt, for example, FLiBe or FLiNaK. Sievert's law predicts that the solubility is proportional to the square root of the partial pressure of the solute gas, if the solvent is metal. Therefore, special attention must be paid when deriving the overall mass transfer coefficient.

4.1 Derivation of tritium mass transfer calculation method

In Figure 4.1, a unit of interphase gas transferring is shown. Take the case of a bimolecular gas diffusing from fluid 1 to fluid 2 as an example. Correspondence between the concentration of the gas and the corresponding partial pressure is shown in Table 4.1.

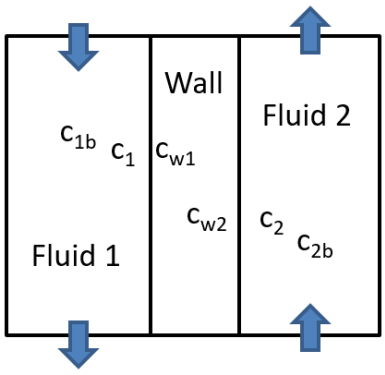

Figure 4.1. Mass transfer unit

Table 4.1. Variables in the mass transfer unit

	Concentration	Partial pressure
Fluid 1 bulk	c_{1b}	p_{1b}
Fluid 1 wall surface	c_1	p_1
Wall inside surface fluid 1 side	c_{1w}	p_{1w}
Wall inside surface fluid 2 side	c_{2w}	p_{2w}
Fluid 2 wall surface	c_2	p_2
Fluid 2 bulk	c_{2b}	p_{2b}

The diffusion of H_2 from the primary coolant mainstream to the inner surface of the wall can be written as Equation (4.1):

$$Q = h_1 A_1 \left(c_{1b} - c_{1w} \right), \tag{4.1}$$

where

Q is the mass transfer rate;

A_1 is the mass transfer area;

c_{1b} and c_{1w} are the T_2 concentrations in the main stream and at the tube wall surface, respectively.

$$Q = h_1 A_1 H_1 \left(p_{1b} - p_{1w} \right), \tag{4.2}$$

$$Q = h_1 A_1 H_1 \left(\sqrt{p_{1b}} + \sqrt{p_{1w}} \right)\left(\sqrt{p_{1b}} - \sqrt{p_{1w}} \right) = h_{1p} A_1 \left(\sqrt{p_{1b}} - \sqrt{p_{1w}} \right), \tag{4.3}$$

$$Q = D_w \frac{2\pi L}{\ln\left(\frac{d_{1o}}{d_{1i}} \right)} \left(c_{1w} - c_{2w} \right) = D_w \frac{2\pi L}{\ln\left(\frac{d_{1o}}{d_{1i}} \right)} S_w \left(\sqrt{p_{1w}} - \sqrt{p_{2w}} \right), \tag{4.4}$$

$$\begin{aligned} Q = h_2 A_2 \left(c_{2w} - c_{2b} \right) = h_2 A_2 H_2 \left(p_{2w} - p_{2b} \right) &= h_2 A_2 H_2 \left(\sqrt{p_{2w}} + \sqrt{p_{2b}} \right)\left(\sqrt{p_{2w}} - \sqrt{p_{2b}} \right) \\ &= h_{2p} A_2 \left(\sqrt{p_{2w}} - \sqrt{p_{2b}} \right) \end{aligned}, \tag{4.5}$$

The overall mass transfer equation has the form of

$$Q = h_o A_1 \left(\sqrt{p_{1b}} - \sqrt{p_{2b}} \right). \tag{4.6}$$

Combining Equations (4.2)–(4.6), the overall mass transfer coefficient is

$$h_o = \frac{1}{\frac{1}{h_{1p} d_{1i}} + \frac{\ln\left(\frac{d_{1o}}{d_{1i}} \right)}{2P_w} + \frac{1}{h_{2p} d_{1o}}} \frac{1}{d_{1i}}. \tag{4.7}$$

The difference of square roots of partial pressures in Equation (4.6) can be estimated by the log mean difference of partial pressures in the main streams of the two fluids:

$$\sqrt{p_{1b}} - \sqrt{p_{2b}} = LMPD = \frac{\left(\sqrt{p_{1i}} - \sqrt{p_{2o}}\right) - \left(\sqrt{p_{1o}} - \sqrt{p_{2i}}\right)}{\ln\left(\frac{\sqrt{p_{1i}} - \sqrt{p_{2o}}}{\sqrt{p_{1o}} - \sqrt{p_{2i}}}\right)}. \tag{4.8}$$

Mass transfer coefficients in the fluids can be calculated using the Sherwood number.

$$\mathrm{Sh} = \frac{h_i d_{hi}}{D_i}, \; i = 1 \text{ or } 2. \tag{4.9}$$

The Sherwood number itself can be calculated using correlations developed for heat transfer calculations, but with the Nu replaced with Sh and Pr replaced with Sc, as shown in the following equation:

$$\mathrm{Sh} = \begin{cases} 0.4\,\mathrm{Re}^{0.6}\,\mathrm{Sc}^{0.36} \text{ for } 1000 \le \mathrm{Re} \le 20000 \\ 0.022\,\mathrm{Re}^{0..84}\,\mathrm{Sc}^{0.36} \text{ for } \mathrm{Re} > 20000 \\ 3.41 \text{ for } \mathrm{Re} < 1000 \end{cases}. \tag{4.10}$$

An iteration loop can be written to calculate the mass transfer rate. The logic of the loop is as follows:

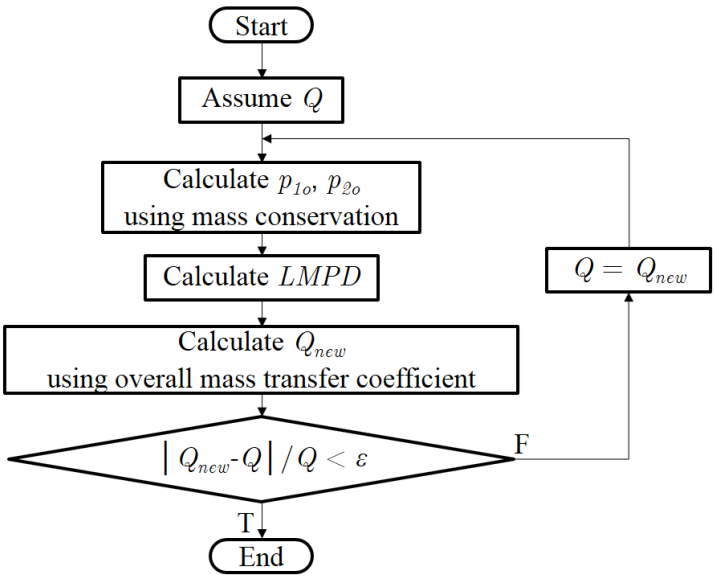

The idea of the LMSPD is adopted from the LMTD in heat transfer. In heat transfer, the driving force is the temperature difference between two objects. Similarly, in mass transport, the driving force is the chemical potential. While the chemical potential is difficult to measure or quantify, the driving force of mass transport can also be expressed in the term of partial pressure [89]. With the partial pressure in the mass transfer corresponding to the temperature in the heat transfer, the correspondence of the mass transfer parameters to the heat transfer parameters is summarized in Table 4.2.

Table 4.2 Analogue of mass and heat transfer

Mass Transfer				Heat Transfer			
Parameter	Symbol	Unit	Expression	Parameter	Symbol	Unit	Expression
Partial pressure	p	Pa	-	Temperature	T	K	-
Mass diffusivity	D	m^2/s	-	Thermal diffusivity	α	m^2/s	$\alpha = \frac{k}{\rho c_p}$
Henry's constant	H_{mt}	mol/(m^3-Pa)	-	Heat capacity	c_p	J/(kg-K)	-
Sievert's constant	K_{mt}	mol/(m^3-$Pa^{0.5}$)	-				
Sherwood number	Sh	-	$\mathrm{Sh} = \frac{hl}{D}$	Nusselt number	Nu	-	$\mathrm{Nu} = \frac{h_t l}{k}$
Schmidt number	Sc	-	$\mathrm{Sc} = \frac{\mu}{\rho D_{\mathrm{AB}}}$	Prandtl number	Pr	-	$\mathrm{Pr} = \frac{c_p \mu}{k} = \frac{\nu}{\alpha}$
Peclet number	Pe	-	$\mathrm{Pe} = \mathrm{Re}\,\mathrm{Sc}$	Peclet number	Pe	-	$\mathrm{Pe} = \mathrm{Re}\,\mathrm{Pr}$
Grashof number	Gr	-	$\mathrm{Gr} = g\beta^* l^3 \Delta c \left(\frac{\rho}{\mu}\right)^2$ $\beta^* = -\frac{1}{\rho}\left(\frac{\partial \rho}{\partial c}\right)_{T,p}$	Grashof number	Gr	-	$\mathrm{Gr} = g\beta l^3 \Delta T \left(\frac{\rho}{\mu}\right)^2$
Stanton number	St	-	$\mathrm{St} = \frac{\mathrm{Sh}}{\mathrm{Re}\,\mathrm{Sc}} = \frac{\mathrm{Sh}}{\mathrm{Pe}}$	Stanton number	St	-	$\mathrm{St} = \frac{\mathrm{Nu}}{\mathrm{Re}\,\mathrm{Pr}} = \frac{\mathrm{Sh}}{\mathrm{Pe}}$

4.2 Comparison with experimental data in the literature

For the benchmark of the developed LMSPD code, comparisons to existing experimental data were made. The ideal experiment would be tritium permeating through metal tubes or pipes in the cross-flow configuration. However, it appears that in the available literature, there are limited experiments of hydrogen isotopes permeating through metal tubes or pipes under flow conditions. Data concerning the separation of hydrogen isotopes using a cross-flow permeation facility are rare. Among the experiments that are available, the experiment performed by Wang et al. has the operating conditions to which the LMSPD code can be applied [90].

4.2.1 Experimental setup

A hollow fiber made of Ni was heated to different temperatures from 400 °C to 1000 °C. The feed gas, which was a mixture of H_2 with the carrier gas, flowed on the shell side, while the purging gas N_2 flowed on the tube side of the Ni fiber in the cocurrent direction with H_2. H_2 concentration on the shell side was controlled by adjusting the ratio of H_2 in the feed gas. Because Ni has high hydrogen selectivity, H_2 diffused from the shell side, permeated through the wall and entered the tube side. Outlet gases were analyzed using gas chromatography to determine the partial pressure difference between the two sides.

The schematic diagram of the experiment is shown in Figure 4.2. The inner diameter and outer diameter of the permeation tube are 1.33 mm and 2.00 mm, respectively. The effective length of the permeation section is 8 cm. Flow rates of gases on both sides are 30 ml/min. Mass flow rates and velocities of both gases will vary with different experimental temperatures. For the modeling, the permeability of H_2 through Ni used is the value provided in the paper, which is $\Phi_{Ni,H} = 1.44\times10^{-6}\exp\left(-\frac{5.107\times10^{4}}{RT}\right)$ [90]. Hydrogen diffusion in gases is also considered in the model. The carrier gas selected in the model is CO_2, and the molar percentage of H_2 on the shell side inlet is 50%.

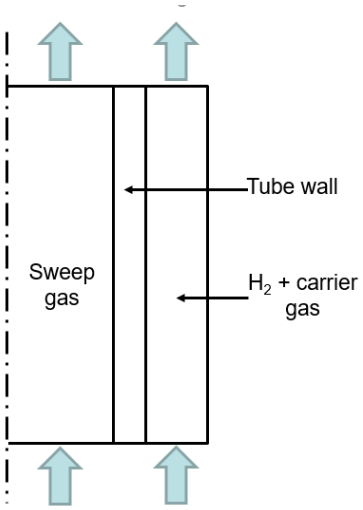

Figure 4.2 Diagram of a countercurrent flow model

Transport coefficients, i.e., diffusivity and solubility, of H_2 in CO_2 and N_2 are summarized in Table 4.3. Assuming all gases are ideal gases, and therefore, the solubility of H_2 in another gas can be estimated using the ideal gas law.

Table 4.3 Transport coefficients of H_2 in CO_2 and N_2

	Diffusivity [atm-m^2/s] [91]	Solubility [mol/(m^3-Pa)]
CO_2	$D_{CO_2,H} = \frac{3.14\times10^{-9}T^{1.750}}{\exp\left(\frac{11.7}{T}\right)}$	$K_{CO_2,H} = \frac{n}{pV} = \frac{1}{RT}$
N_2	$D_{N_2,H} = \frac{1.539\times10^{-6}T^{1.548}}{\left[\ln\left(\frac{T}{3.16\times10^{-7}}\right)\right]^2 \exp\left(-\frac{2.8}{T}\right)\exp\left(\frac{1067}{T^2}\right)}$	$K_{N_2,H} = \frac{n}{pV} = \frac{1}{RT}$

4.2.2 Code calculation results

The experimental data from Wang's paper for this study are shown in Figure 4.3 and Figure 4.4 by scattered points [90]. In this plot, the partial pressures used in the *x*-axis are calculated from the concentration measurements at the gas outlets.

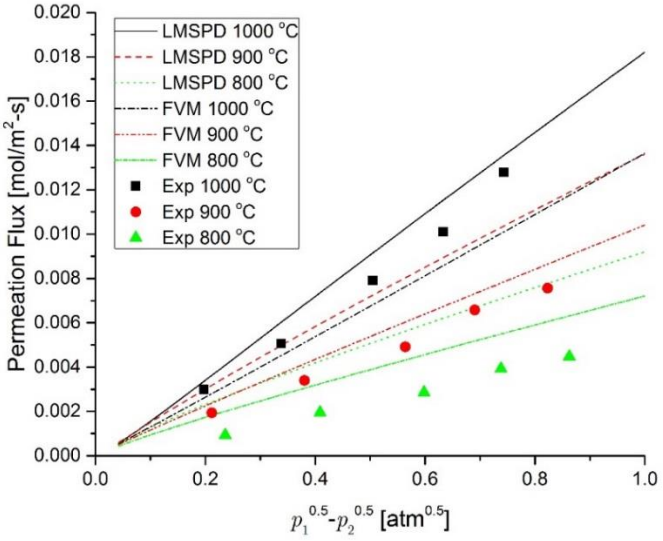

Figure 4.3 Comparison of code calculation results and experimental data (800–1000 °C)

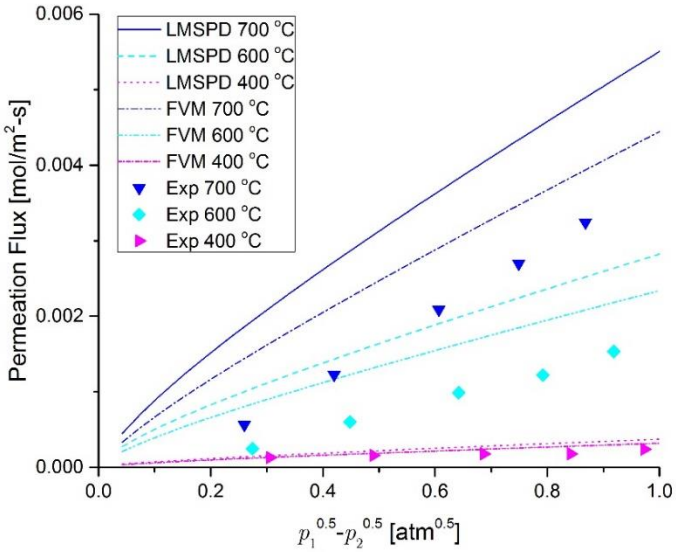

Figure 4.4 Comparison of code calculation results and experimental data (400–700 °C)

For the convenience of the benchmark, the code calculation results are also expressed in the permeation flux. The original experiment was performed under a variety of temperatures. To

examine how temperature influences the code calculation, the temperatures used in the calculation are set to be the same as the experimental temperatures, i.e., 400 °C, 600 °C, 700 °C, 800 °C, 900 °C and 1000 °C. The entire geometry is assumed to be at the same temperature in each case. The range of the partial pressure difference is slightly larger in the code calculation fully to cover the range performed in the original experiment.

The calculated H_2 permeation flux under different temperatures is plotted against the difference of the square root of the partial pressures in Figure 4.3 and Figure 4.4. With the increase of the partial pressure difference, the tritium permeation flux increases. The gas temperature also affects the permeation flux by influencing the mass transport coefficients. At the same partial pressure difference, the higher the temperature is, the larger the permeation flux becomes.

The same model was also calculated using a MATLAB code written based on a coupled heat transfer and tritium mass transport model [52], where the geometry was divided into segments and in each segment local mass and energy balances were imposed. This coupled code is referred to as the "Finite Volume Method code" (FVM code) in this paper. In the FVM code, tritium permeation is one dimensional from the tube wall outer surface (shell side) to the inner surface (tube side). It is assumed that the hydrogen concentration profiles in both the carrier gas and sweep gas are flat. In other words, the gradient of H_2 partial pressure exits only in the tube wall. The tube wall is divided into segments only in the axial direction but not in the radial direction. The results of the FVM code are also plotted in Figure 4.3 and Figure 4.4. The same as the results obtained from the LMSPD code and consistent with expectations from the theoretical basis, the hydrogen permeation flux increases with the increase of temperature or hydrogen partial pressure difference.

From the results it can be observed that temperature has a significant effect on the permeation flux. As an example, for high temperatures, the permeation flux at 1000 °C obtained from the two codes are compared with the experimental data. In general, the LMSPD code overestimates the permeation flux while the FVM code underestimates it. The average difference between the LMSPD code results and experimental data is 13.3%. The average difference between FVM code results and experimental data is 14.7%.

As the temperature decreases, the absolute differences between both code results and the experimental data are of the same magnitude, while the relative differences become larger because the values of the permeation flux also decrease. For even lower temperatures, for instance, at 600 °C, both codes tend to overestimate the permeation flux. The differences between the calculation results and the experimental data at 600 °C are apparently larger than those at 1000 °C. For lower difference values of the square root of the partial pressures, the code calculation results could be as high as two or three times greater than the experimental results. At 400 °C, the differences between the code results and the experimental data are smaller than those at 600 °C, while still about four times larger than those at 1000 °C.

The normal operating temperature of FHRs is about 700 °C. The tritium permeation rate at 700 °C is of particular interest in this study. Therefore, the calculation results and the experimental data at 700 °C are compared. The calculated permeation flux from both codes are higher than the experimental data by 6.97×10^{-4}–1.66×10^{-3} mol/(m^2-s). Comparing the results obtained from the two codes, the hydrogen permeation flux calculated from the LMSPD code is higher than that calculated from the FVM code by 4.21×10^{-4}–9.59×10^{-4} mol/(m^2-s).

Calculation of the experiment using the finite element method is also performed. An axisymmetric model is built using COMSOL Multiphysics. The geometry and domains are set as shown in Figure 4.2. Physics modules used in the model are turbulent flow and transport of diluted species. The model is solved using stationary solvers. The two turbulent flow modules are solved first using a segregated and direct solver, and the three mass transport modules are then solved using a fully coupled and direct solver. The velocity field obtained from the first step is used as the initial conditions in the second step. On the interfaces between fluids and the wall, pointwise constraints are used to force the flux to continue while allowing the concentration to jump [92].

Permeation flux at 1000 °C obtained from the two codes are compared with the experimental data in Figure 4.5. In general, the LMSPD method overestimates the permeation flux, while the meshed method underestimates it. The difference between the LMSPD method results and experimental data varies from 5.9% to 19.0%. The difference between the FVM method results and experimental data varies from 10.6% to 21.1%.

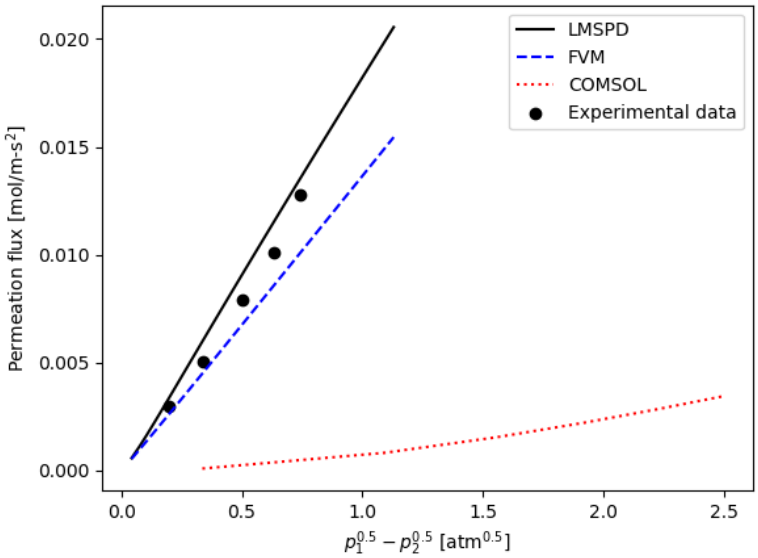

Figure 4.5 Comparison of calculation results at 1000 °C

For lower temperatures, both codes tend to overestimate the permeation flux, as shown in Figure 4.6 where the calculation results and experimental data are compared at 600 °C. In addition, the difference between the calculation results and the experimental data were apparently larger than at higher temperatures. For lower differences of the square root of partial pressure, the code calculation results could be as high as twice or three times the experimental results.

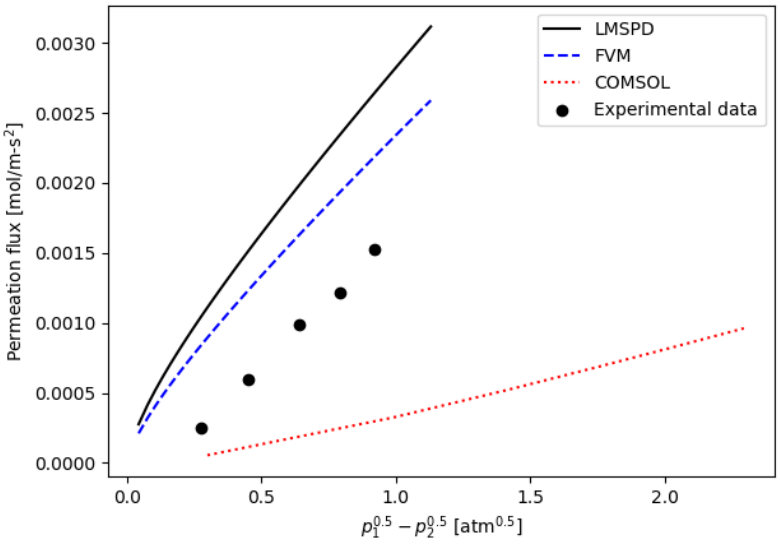

Figure 4.6 Comparison of calculation results at 600 °C

4.2.3 Difference between code calculation and experimental data

The absolute and relative differences between the code calculations and experimental data are shown in Table 4.4. The differences are larger at lower temperatures and with smaller driving forces, i.e., smaller values in the difference of square roots of partial pressures on two sides. Comparing the absolute difference between the code calculation results and the experimental data, it can be found that the value always falls in the $10^{-6} – 10^{-3}$ magnitude range. The relative difference, however, becomes significant when the permeation flux is low.

Table 4.4 Difference of permeation flux between the code results and experimental data

Temperature [°C]	Code	Type	Min. difference	$p_1^{0.5}–p_2^{0.5}$ [atm$^{0.5}$]	Max. difference	$p_1^{0.5}–p_2^{0.5}$ [atm$^{0.5}$]
1000	LMSPD	Absolute	3.58×10^{-4}	0.20	1.43×10^{-3}	0.63
		Relative (%)	5.91	0.74	19.0	0.34
	FVM	Absolute	3.92×10^{-4}	0.20	2.69×10^{-3}	0.74
		Relative (%)	10.6	0.34	21.1	0.74
900	LMSPD	Absolute	1.27×10^{-3}	0.21	3.88×10^{-3}	0.82
		Relative (%)	47.9	0.69	65.9	0.21
	FVM	Absolute	4.57×10^{-4}	0.21	1.16×10^{-3}	0.56
		Relative (%)	11.7	0.69	24.0	0.56
800	LMSPD	Absolute	1.73×10^{-3}	0.24	3.62×10^{-3}	0.86
		Relative (%)	80.0	0.74	184	0.24
	FVM	Absolute	1.06×10^{-3}	0.24	1.83×10^{-3}	0.86
		Relative (%)	39.6	0.74	113	0.24
700	LMSPD	Absolute	1.30×10^{-3}	0.26	1.66×10^{-3}	0.87
		Relative (%)	51.1	0.87	230	0.26
	FVM	Absolute	6.97×10^{-4}	0.87	9.06×10^{-4}	0.42
		Relative (%)	21.5	0.87	155	0.26
600	LMSPD	Absolute	7.94×10^{-4}	0.27	1.12×10^{-3}	0.79
		Relative (%)	72.0	0.92	318	0.27
	FVM	Absolute	5.90×10^{-4}	0.27	7.13×10^{-4}	0.79
		Relative (%)	42.3	0.92	236	0.27
400	LMSPD	Absolute	2.43×10^{-5}	0.31	1.47×10^{-4}	0.84
		Relative (%)	18.5	0.31	81.6	0.84
	FVM	Absolute	1.18×10^{-6}	0.31	1.00×10^{-4}	0.84
		Relative (%)	0.90	0.31	55.7	0.84

There are several potential reasons for the differences between code calculation results and the experimental data. Temperature is the main factor affecting the permeation flux. Compared with higher temperatures, at lower temperatures, the permeability of hydrogen through a nickel wall decreases, and therefore, the amount of hydrogen permeating through the wall is less than that at higher temperatures. The absolute differences between code results and the experimental data are reasonable and are of the same magnitude as the differences at higher temperatures. However, because the permeation rates are much smaller at lower temperatures, the relative differences appear much larger than those at higher temperatures. The larger differences at smaller driving forces can also be explained by the decreased hydrogen permeation rates. For application in FHRs, the temperature range of most interest is the operating temperature of the tritium removal facility, i.e., above 700 °C, at which temperatures the agreement between the codes and the experimental data is good. In the sections where the operating temperature is lower, tritium leakage from the primary coolant to the surrounding environment is relatively small. Therefore, even a larger relative uncertainty of the code prediction might not be of considerable concern.

Surface conditions of the permeation tube also have an effect on the hydrogen permeation flux. In the experiments, the nickel tube surface could be oxidized, which decreases the permeation flux. Surface oxidation could be a possible cause of the overestimation of both codes at most of the temperatures modeled. In addition, although the information of measurement uncertainties is not available for the original experiments, from the principles of the gas chromatographic method, measurement uncertainties have a more dominant effect when the concentration is low [93].

4.2.4 Difference between COMSOL simulation and experimental data

COMSOL simulation results are at least one order of magnitude lower than either code calculation results or experimental data. The differences between the COMSOL simulation results and the experimental data at 1000 °C, 600 °C, and 400 °C are listed in Table 4.5.

Table 4.5 Difference of permeation flux between the code results and experimental data

Temperature [°C]	Type	Min. difference	$p_1^{0.5}$–$p_2^{0.5}$ [atm$^{0.5}$]	Max. difference	$p_1^{0.5}$–$p_2^{0.5}$ [atm$^{0.5}$]
1000	Absolute	-4.97×10^{-3}	0.34	-1.23×10^{-2}	0.74
	Relative (%)	96.20	0.74	98.13	0.34
600	Absolute	-4.86×10^{-4}	0.45	-1.24×10^{-3}	0.92
	Relative (%)	79.73	0.79	81.04	0.45
400	Absolute	-1.14×10^{-4}	0.31	-1.76×10^{-4}	0.97
	Relative (%)	69.39	0.84	87.00	0.31

The difference might come from the different approaches to dealing with interface boundary conditions. In COMSOL, the pointwise constraint condition does not model the flux but assigns a concentration value to the downstream side. A parameter named the partition factor is used to define the jump of concentration across the boundary. The definition of partition factor is the ratio of concentrations in two different and immiscible phases at equilibrium [94], shown as the following:

$$P_{AB} = \frac{c_B}{c_A}. \tag{4.11}$$

For the interface of feed gas and wall, the partition factor should be

$$K_{partition,1w} = \frac{c_{w1}}{c_{1w}} = \frac{K_w\sqrt{p_{1w}}}{K_1 p_{1w}} = \frac{K_w}{K_1\sqrt{p_{1w}}} = \frac{K_w}{\sqrt{K_1 c_{1w}}}. \tag{4.12}$$

Similarly, the partition factor for the interface of the wall and sweep gas can be written. Therefore, the partition factor is dependent on the concentration of hydrogen in the fluids, and could vary with location. However, in most cases, the partition factor is known beforehand, often obtained via experiments or atom-based calculation [95]. Estimating the partition factor during the simulation process might be inaccurate.

In addition, in COMSOL, diffusivities in each material must be input. The experiment modeled only provided hydrogen permeability through the nickel wall. While the exact diffusivity of the nickel wall used in the experiment is unknown, a value from the literature was used in the simulation. This estimation will also lead to inaccuracy in the permeation flux.

4.2.5 Permeation flux and the difference of square root of partial pressure

The mass transfer coefficients of H_2 in all three domains are compared in Table 4.6. The mass transfer coefficient in the tube wall is several orders of magnitude lower than that in the sweep gas or the feed gas, showing that the main resistance exists in the tube wall. Because of this difference, omitting the mass transfer resistance in gases would not have a significant effect on the calculation results. Therefore, only hydrogen permeation through the wall is considered in the FVM code.

Table 4.6 Comparison of the mass transport coefficients in different domains

Temperature [°C]	$p_1^{0.5}$–$p_2^{0.5}$ [atm$^{0.5}$]	Mass transfer coefficient [mol/m^2-s-Pa]		
		Feed gas	Wall	Sweep gas
1000	0.125	5.80×10^{-3}	8.53×10^{-8}	2.27×10^{-4}
	0.743	6.00×10^{-3}	8.07×10^{-8}	2.40×10^{-4}
900	0.212	2.51×10^{-3}	1.96×10^{-7}	6.85×10^{-5}
	0.823	6.88×10^{-3}	4.65×10^{-8}	2.89×10^{-4}
800	0.236	2.79×10^{-3}	1.08×10^{-7}	8.00×10^{-5}
	0.862	7.52×10^{-3}	2.65×10^{-8}	3.26×10^{-4}
700	0.260	3.17×10^{-3}	5.33×10^{-8}	9.51×10^{-5}
	0.868	7.94×10^{-3}	1.44×10^{-8}	3.52×10^{-4}
600	0.274	3.60×10^{-3}	2.32×10^{-8}	1.12×10^{-4}
	0.918	8.67×10^{-3}	6.54×10^{-9}	3.99×10^{-4}
400	0.306	4.50×10^{-3}	2.43×10^{-9}	1.53×10^{-4}
	0.973	9.94×10^{-3}	7.58×10^{-10}	4.91×10^{-4}

The permeation flux is directly related to the difference of square roots of partial pressures on both sides. The linearity of the curves of permeation flux calculated from LMSPD and FVM codes shown in Figure 4.3 and Figure 4.4 are apparent and consistent with the form of Eq. (4.6). Fitting the code results in Figure 4.3 and Figure 4.4 to linear relationships with $\left(\sqrt{p_1} - \sqrt{p_2}\right)$, the R^2 values of the fitted correlations are above 0.94. This is consistent with what is predicted in Sievert's

equation [96], confirming that the assumption of diffusion in the wall being the rate-determining step is reasonable.

4.3 Validation experiment of the tritium removal facility

The experiment in the previous section, in which, the LMPSD code was validated, used nickel as the material for the permeation tube wall. In the FHR system, the tritium removal facility is fabricated with stainless steel 316. To validate the code further with facilities made of steel materials, two laboratory-scale experiments were designed. In addition, the experiments can be used for validation of the effectiveness of the tritium removal facility.

For safety concerns, hydrogen was used as a surrogate for tritium. Before formally performing experiments using molten salt, a test experiment was planned using a surrogate for the molten salt. Because of time constraint and delay in the construction of the molten salt loop in the lab, the molten salt experiment has not been completed.

4.3.1 Surrogate for molten salt

The surrogate selected is better to have large enough hydrogen solubility, be physically and chemically stable, not be corrosive to structure materials and have a similar viscosity to the molten salt. In addition, it would be advantageous if the testing experiments can be conducted at room temperature. But a high hydrogen solubility is the most important criterion for the selection of potential surrogates because it is the key factor to determine whether the hydrogen in the samples collected can be detected.

Water, as the most common solvent, is studied first. Hydrogen solubility in water has been investigated by several research groups. Gevantman took the values of hydrogen solubility in water listed in the International Union of Pure and Applied Chemistry “Solubility Data Series” and fitted them to the following correlation [97]:

$$\ln K = -48.1611 + \frac{55.2845}{\frac{T}{100}} + 16.8893 \ln \frac{T}{100} \tag{4.13}$$

where the applicable temperature range is 273.15 to 353.15 K, and the unit of solubility is mole fraction of hydrogen in water.

The solubility of hydrogen in water is also plotted in Figure 4.7 [98]. The temperature range of this plot is 0 to 60 °C. The unit of the solubility is the weight fraction of hydrogen to water.

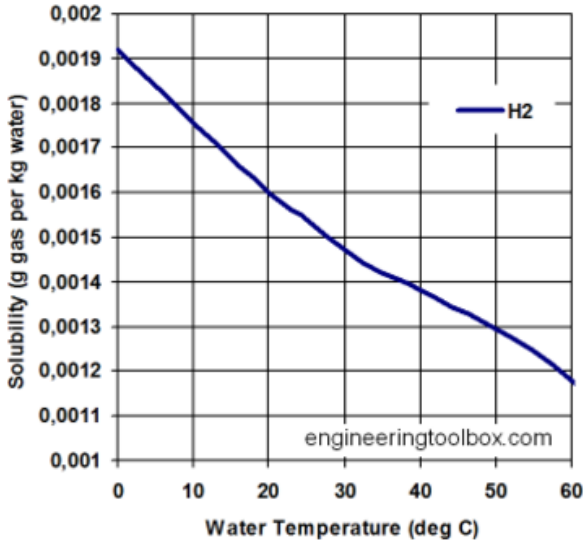

Figure 4.7. Hydrogen solubility in water [98]

A simple comparison of H_2 solubility in water obtained from the above-mentioned sources [97][98] is shown in Figure 4.8 and Table 4.7. From the figure, it can be observed that H_2 solubility in water is consistent across the two models. The relative error shown in the table also confirms the consistency.

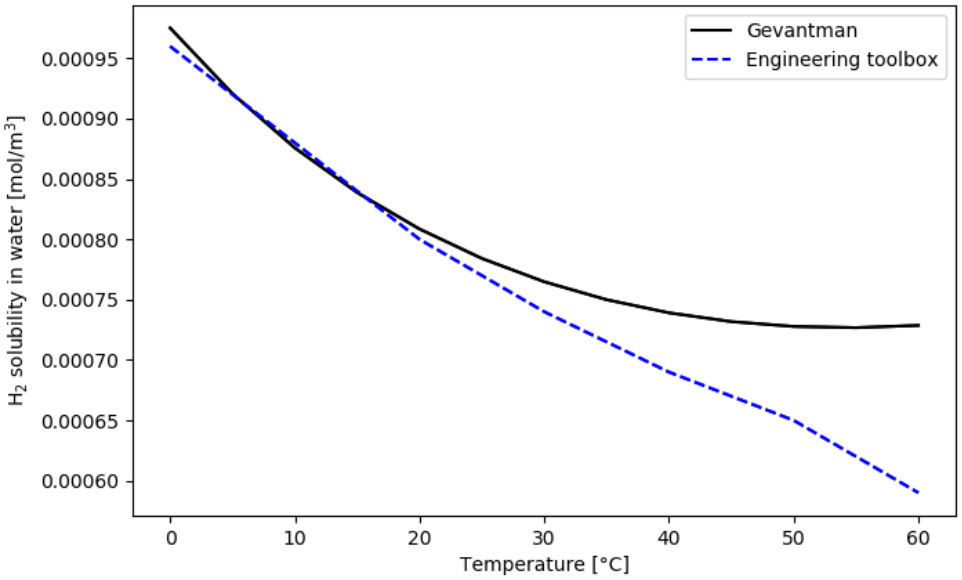

Figure 4.8. Comparison of H_2 solubility in water obtained from different models

Table 4.7. The relative difference of H_2 solubility in water obtained from different models

Temperature [°C]	Solubility [$\times 10^{-4}$ mol/m^3]	Solubility [$\times 10^{-4}$ mol/m^3]	Relative error [%]
	Gevantman [97]	Engineering toolbox [98]	
0	0.000975192	0.00096	1.56
5	0.000920734	0.00092	0.08
10	0.000875766	0.00088	0.48
15	0.000838773	0.00084	0.15
20	0.000808558	0.0008	1.06
25	0.00078417	0.00077	1.81
30	0.000764851	0.00074	3.25
35	0.000749995	0.000715	4.67
40	0.000739115	0.00069	6.65
45	0.000731823	0.00067	8.45
50	0.000727808	0.00065	10.69
55	0.000726825	0.00062	14.70
60	0.000728682	0.00059	19.03

Hydrogen diffusivity in water was measured and fitted to a correlation by Jähne et al. [99]:

$$D = 3.338 \times 10^{-6} \exp\left(-\frac{16060}{R_g T}\right) \tag{4.14}$$

where

D is the hydrogen diffusivity in water with the unit of m^2/s;

T is the temperature in K;

R_g is the ideal gas constant, 8.314 J/(K-mol).

However, from the values of H_2 solubility in water, it can be observed that water is actually a poor solvent of gaseous hydrogen. The reason behind this is that H_2 is a nonpolar molecular gas, while water (H_2O) consists of polar molecules.

Aqueous salt solutions, such as NaCl solution, is another possible option to investigate. However, ionic salt molecules dissociate and exit as ions once dissolved in water. The ions tend to be solvated by water molecules and further decrease the solubility of the nonpolar hydrogen molecules. Consequently, hydrogen solubility in aqueous solutions of salts is even lower than that in pure water. Both pure water and aqueous salt solutions are not ideal surrogates for the molten salt.

Then, the search for the solvent was switched to organic liquids. Researches have been performed for decades to develop liquid hydrogen carriers. These hydrogen carriers were originally designed for storing hydrogen as a potential green energy source. Therefore, the requirements of the hydrogen carriers include:

1. Large hydrogen storage capacity;
2. Quick absorption and desorption under reasonable conditions.

However, hydrogen carriers do not have to dissolve gaseous hydrogen physically. Hydrogen could combine with the atoms of the chemical structure and form chemical bonds or hydrogen bonds. This is the case with most organic hydrogen carriers. Because hydrogen dissolves in the molten salt physically, to simulate the real situation, it is crucial that hydrogen does not form chemical bonds with the surrogate liquid molecules.

In Table 4.8, hydrogen solubility in several organic liquids is listed and compared with that of water. The last column, desired hydrogen solubility, is the equivalent value in mole fraction to H_2 concentration in the liquid, i.e., 100 moles of hydrogen per cubic meter of solution. This value is of importance because H_2 solubility in the molten salt is of the same magnitude of 100 mol/m^3.

Table 4.8. Hydrogen solubility in organic liquids

Chemical	Molecular formula	Flammability	Molar mass [g/mol]	Density [25 °C]	Molecular density [mol/m^3]	Hydrogen solubility [mole fraction]	Desired hydrogen solubility [mole fraction] (equivalent to 100 mol H_2/m^3)
water	H_2O	N	18	1000	55555.56		0.0018
n-hexane	C_6H_{14}	Y	86.178	664.7	7713.105	0.000713	0.012965
n-octane	C_8H_{18}	Y	114.23	698.6	6115.731	0.000676	0.016351
n-decane	$C_{10}H_{22}$	Y	142.285	726.4	5105.247	0.000673	0.019588
toluene	C_7H_8	Y	92.141	873.6	9481.121	0.000315	0.010547
acetonitrile	C_2H_3N	Y	41.053	779.5	18987.65	0.000287	0.005267
acetone	C_3H_6O	Y	58.08	784.4	13505.51	0.00027	0.007404
N,*N*-dimethyl-formamide	C_3H_7NO	Y	73.095	944.5	12921.54	0.000184	0.007739
tetrahydrofuran	C_4H_8O	Y	72.108	882.5	12238.59	0.000141	0.008171
1,4-dioxane	$C_4H_8O_2$	Y	88.107	1028	11667.63	0.000147	0.008571
N-methyl-2-pyrolodone	C_5H_9NO	Y	99.133	1028	10369.91	0.000178	0.009643
dibenzyltoluene	$C_{21}H_{20}$	N	272	1040	3823.529	0.003	0.026154

From Table 4.8, all of the candidates listed fail to have a H_2 solubility close to that of the molten salt. Most of them are an order of magnitude (in mole fraction) below the needed level, while a few are two orders of magnitudes below. In addition, most of the candidates investigated are highly flammable, which is not ideal for laboratory experiments. Therefore, the organic surrogates were not selected.

It was then decided to use a carrier gas as the surrogate for the molten salt. The idea is to mix H_2 with another nonflammable gas and use the gaseous mixture instead of the molten salt. Krypton was selected as the carrier gas. The reason for selecting krypton as the carrier gas is that Kr is a major component of the reactor off-gas. In addition, it is a heavy inert gas which does not permeate through metals. Hydrogen is also a component of the off-gas from the reactor. Separation of H_2 from the other components of the off-gas has been researched for years. The experimental results of separating H_2 from Kr can also benefit the research of reactor off-gas clean-up, providing data for off-gas separation. The properties of Kr are listed in Table 4.9.

Table 4.9 Kr properties

Property	Unit	Value
Density (STP)	g/L	3.749
Molecular mass	g/mol	83.798
Heat capacity	J/(kg-K)	251
Thermal conductivity	W/(m-K)	0.00943
Viscosity	Pa-s	2.32×10^{-5}
H_2 diffusivity	m^2/s	$\frac{1.82\times10^{-6}T^{-1.564}}{\left(\ln\frac{T}{1.69\times10^{8}}\right)^{2}\exp\left(\frac{26.4}{T}\right)}$

4.3.2 Setup of gas loop experiment

To take advantage of the measurement instrument (a gas chromatograph) and lab space, a validation experiment of the cross-flow tritium removal facility was constructed at the University of Idaho.

As explained in the previous section, the carrier gas selected was Kr. Nitrogen was selected as the sweep gas in the experiment for the consideration of achieving a good accuracy in the H_2 detection. A gas chromatograph (GC) was selected to be the instrument for measuring the H_2 concentration in the outlet sweep gas. The GC has a thermal conductivity detector, which detects different gases according to the difference in their thermal conductivities. Although helium is usually used as a sweep gas in nuclear reactor systems, its thermal conductivity is too close to that of hydrogen to be separated apart. Therefore, helium is not used as the sweep gas in this experiment.

The designed experimental setup is shown in Figure 4.9. Kr and H_2 are stored premixed in a gas cylinder. The gas mixture flows across the tube bank. The sweep gas, which is N_2, flows inside the tube bank. H_2 will permeate through the tube walls and be carried out by the sweep gas. Samples will be collected at the outlet of the sweep gas and analyzed. Temperatures and pressures of the inlet and outlet gases will be monitored and recorded for the accurate calculation of gas flow rates.

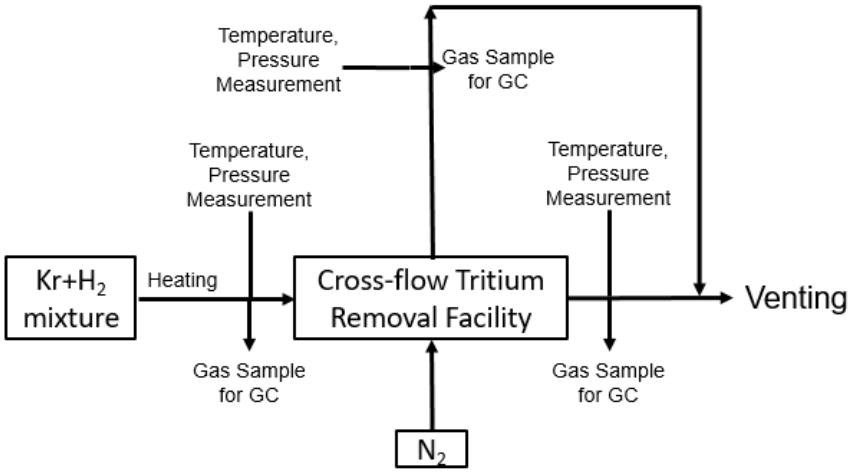

Figure 4.9 Scheme of the experimental setup

The designed flow diagram is shown in Figure 4.10 and a more detailed drawing is shown in Figure 4.11. The loop will be vacuumed and then charged with a mixture of H_2 and Kr. The percentage of H_2 to Kr in the gas cylinder is 50–50%. The pressure of the gas mixture will be released from

the high-pressure gas cylinder to slightly above the atmospheric pressure (1–10% above the atmospheric pressure) via a gas regulator. The gas mixture in the loop will be circulated until the concentration of H_2 in the loop cannot be detected by the GC. During the process, H_2 will permeate into the sweep gas gradually and be vented into the hood. To ensure safety, the exhausted H_2 and N_2 mixture will be monitored for H_2 concentration and extra N_2 will be added as necessary to keep the H_2 level in the mixture below 1%. The flow rate of the sweep gas, N_2, will vary from 30 to 500 cm^3/min.

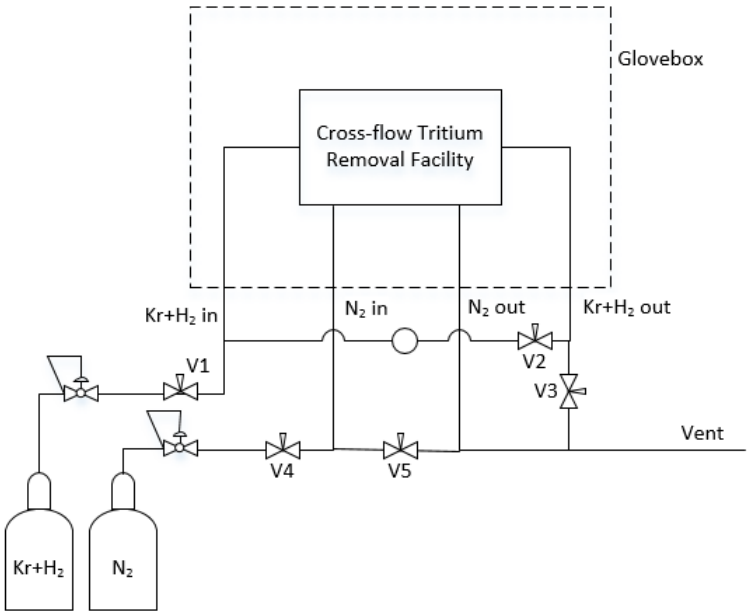

Figure 4.10 Flow diagram

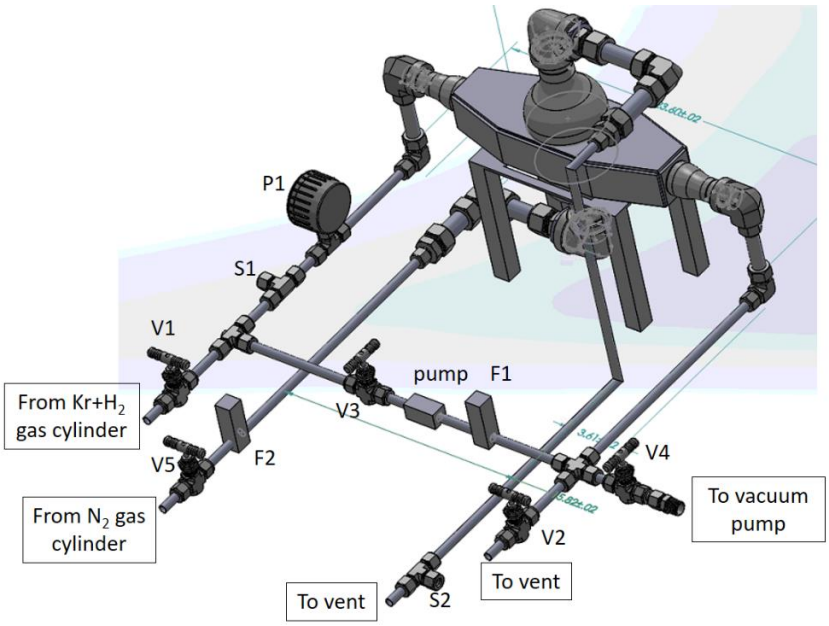

Figure 4.11 CAD drawing of the experimental setup

As designed, before the experiment, all the valves are closed. The $Kr+H_2$ line will be vacuumed. Then V2 is opened while V3 is kept closed. V1 will be open and the gas mixture will fill up the loop until the pressure transducer shows the pressure in the loop is 1.0 atm. The total amount of $Kr+H_2$ volume is 0.5 L. Then, V1 is shut off, V4 is opened, and the pump is turned on. The experiment will run for a couple of hours, while samples are taken at the outlets of the gas lines outside the glovebox. A monitor will be placed at the vent. If the H_2 concentration in the vented gas is higher than 4%, V5 will be opened and N_2 will be used to reduce the H_2 concentration. When the H_2 concentration in the out-going N_2 is lower than its detectable limit by the GC, the experiment ends. V2 is shut off and V3 is opened. Kr and the remaining H_2 (<4% concentration expected) will be vented.

The section of the loop that was originally designed to be set up inside the glove box is mainly the laboratory-scale cross-flow facility. Taking into consideration the dimensions of the glove box main chamber, the connections of the facility to the tubes need to be bent, as shown in Figure 4.12. A table was built to support the weight of the facility. The completed setup is shown in Figure 4.13. For the penetration of the four tubes in and out of the glovebox, four through holes were drilled on the back wall of the glovebox. Bored-through fittings were used with gaskets to seal the

pass-throughs. However, due to lack of time, the glovebox was not configured into full operation, and the experimental setup was placed in the hood instead.

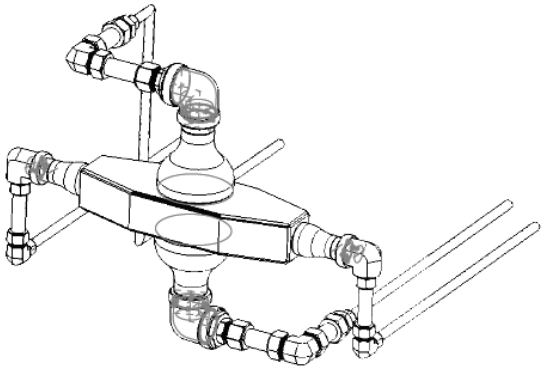

Figure 4.12 Section inside the glove box

Figure 4.13 Completed experimental setup inside glovebox

The main body of the experimental facility, i.e., the tritium removal facility was wrapped in thermal insulations. Six thermocouples were installed at different locations of the loop, five of which were on the tritium removal facility. The locations are noted as “top,” “bottom,” “left,”

“right,” “surface,” and “tee,” respectively. The thermocouple on the tee was located away from the tritium removal facility outlet with a significant distance and measured the temperature of the tubing outer surface. The thermocouples used in this experiment were wire-type thermocouples. Figure 4.14 shows a close-up look at the installation of the thermocouples. The wire was wrapped around a nut. The nut also fixed the thermocouple in place for stable measurement. Tape heaters were wrapped tightly around the outer surfaces of the tritium removal facility, and then the thermal insulations were wrapped outside the tape heaters. Figure 4.15 shows the facility with thermal insulations wrapped around.

Figure 4.14. A close-up look at the thermocouple installation

Figure 4.15. Tritium removal facility wrapped in thermal insulations

At the time of carrying out the experiment, the GC, which in the original experiment design was to be used for the measurement of the H_2 concentration in the sweep gas N_2, was not available. To compensate, a pressure transducer was installed on the loop and measured the pressure of the Kr + H_2 gas mixture inside the loop.

4.3.3 Safety measures for H_2 usage

It is to be noted that since explosive gas (H_2) is used in this experiment, we designed several measures to ensure safety. The measures are as follows:

1. The experimental loop, or at least the major section including the tritium removal facility, should be set up inside a glovebox or fume hood.
2. The exhaust gas, i.e., the N_2 and H_2 mixture, should be monitored for H_2 concentration.
3. Once the H_2 concentration in the exhaust gas exceeds 1% limit, extra N_2 will be added to the exhaust gas mixture to dilute H_2.
4. Faculty, staff, and students must follow the university safety guidelines and wear safety equipment during operation of the experiment.

4.3.4 Fabrication of the laboratory-scale cross-flow tritium removal facility

A laboratory-scale cross-flow tritium removal facility was fabricated for the experiment. It was made of stainless steel 316L. The tube bank consists of 27 stagger-arranged tubes. The drawings with dimensions of the facility are shown in Figure 4.16. The tubes are a half inch in size and have a wall thickness of 0.035 in. The thinnest wall thickness commercially available was used to promote hydrogen permeation. Reducers were welded on the facility as the gas inlets and outlets for smooth transitions from gas lines to the facility. For convenience of connection, pipe nipples were welded onto the reducers. The width of the main flow body is 6 inches, which left two gaps between the side walls and the tube bank. To reduce the percentage of the gas bypass from the two gaps, trapezoidal-shaped spacers were added to the side walls. A 1-inch cylinder was also welded in front of the tube bank for the even distribution of the gas flow. It prevents the main gas stream from concentrating in the center of the tube bank.

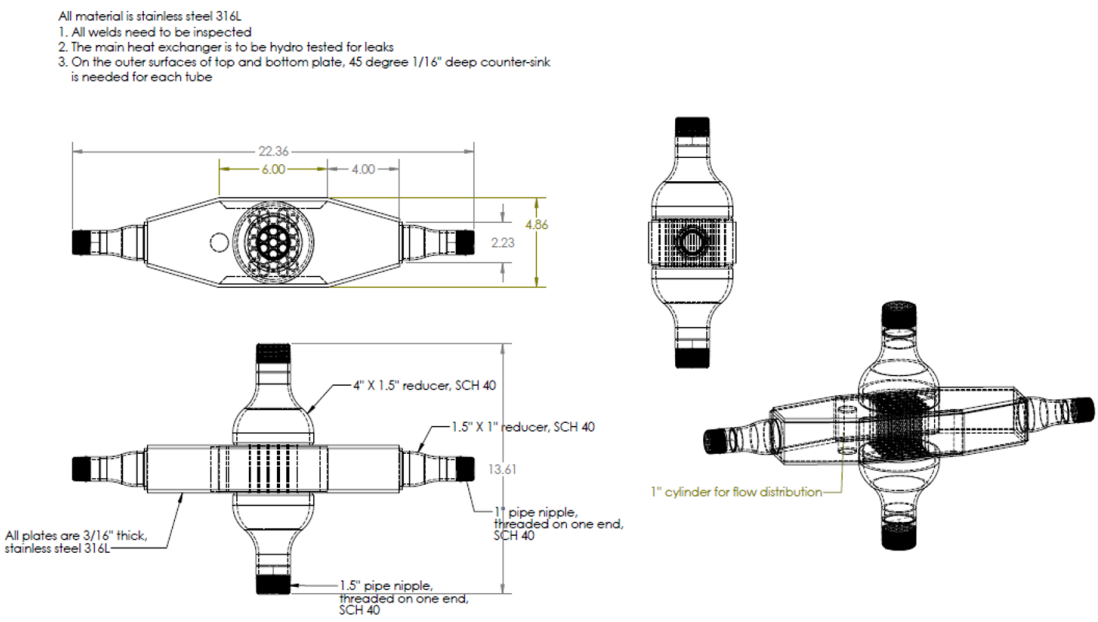

Figure 4.16 Drawings of the small-scale facility

The plates of the facility were made by laser cutting and welded together with the tube bank. Figure 4.17 shows the status of the facility after the tube bank was welded and has passed a 35-psi leakage test. The completed facility is shown in Figure 4.18. All the welds are full penetration welds.

Figure 4.17 Laboratory-scale cross-flow tritium removal facility with tube bank welded

Figure 4.18 Completed laboratory-scale cross-flow tritium removal facility

4.3.5 Prediction of gas-loop experiment results

Before the hydrogen-permeation experiment, a prediction calculation of the experiment was carried out. The hydrogen concentration in the outlet sweep gas was calculated with various values of the key operational parameters. The major objectives of the prediction calculation were to obtain an idea of the magnitude of the hydrogen level to be detected in the sweep gas samples and to determine the appropriate operating conditions.

The effects on the outlet H_2 concentration in sweep gas of various inlet H_2 concentrations, temperatures, and gas flow rates were investigated. The calculation results are plotted in Figure 4.19 to Figure 4.21. It can be observed that with the increase of inlet H_2 concentration, the outlet H_2 concentration in the sweep gas increases at first, and then the increase slows down after the inlet H_2 concentration exceeds about 30%. With the increase in temperature, the H_2 extraction rate slightly drops. This is because the calculation controls the flow velocity of the feed gas. At higher temperatures, the density of the gas decreases and this leads to a decrease in the flow rate. Less H_2 enters the cross-flow facility, resulting in a decrease in the outlet H_2 concentration in the sweep gas. Increase of the feed gas velocity affects the outlet H_2 concentration positively. However, similar to inlet H_2 percentage, the increase of feed gas velocity is more obvious initially. After the velocity reaches about 0.1 m/s, further increase of the feed gas velocity has limited influence on the outlet H_2 concentration in the sweep gas.

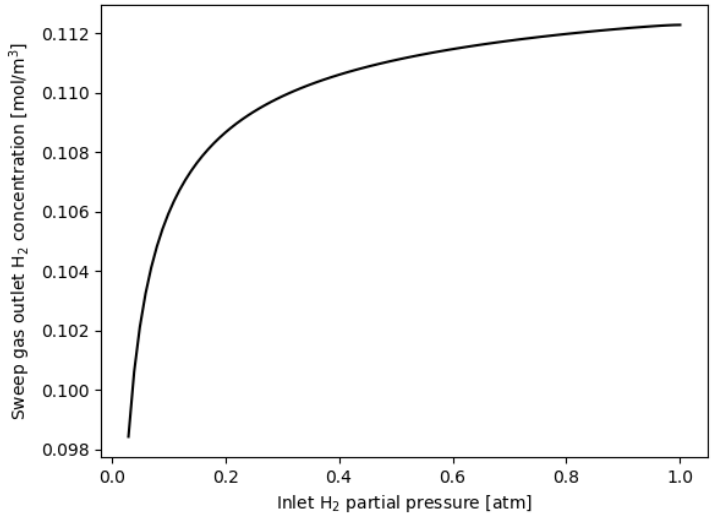

Figure 4.19 Effect of inlet H_2 percentage on outlet H_2 concentration in the sweep gas

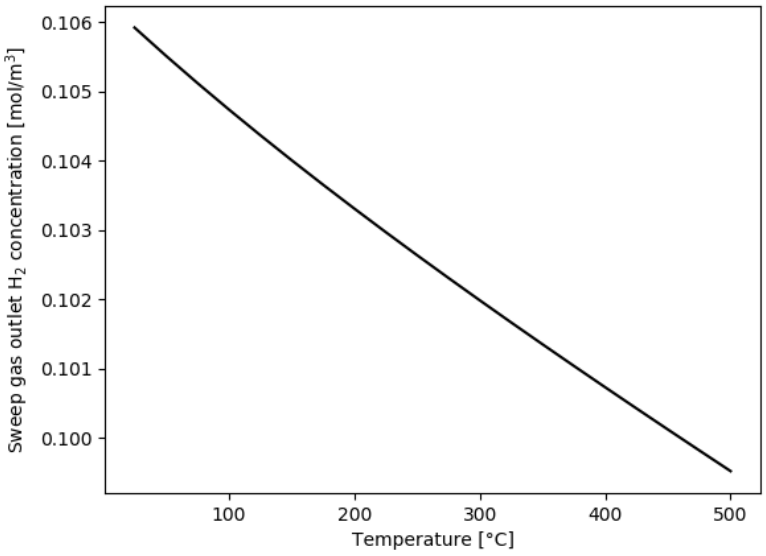

Figure 4.20 Effect of operating temperature on outlet H_2 concentration in the sweep gas

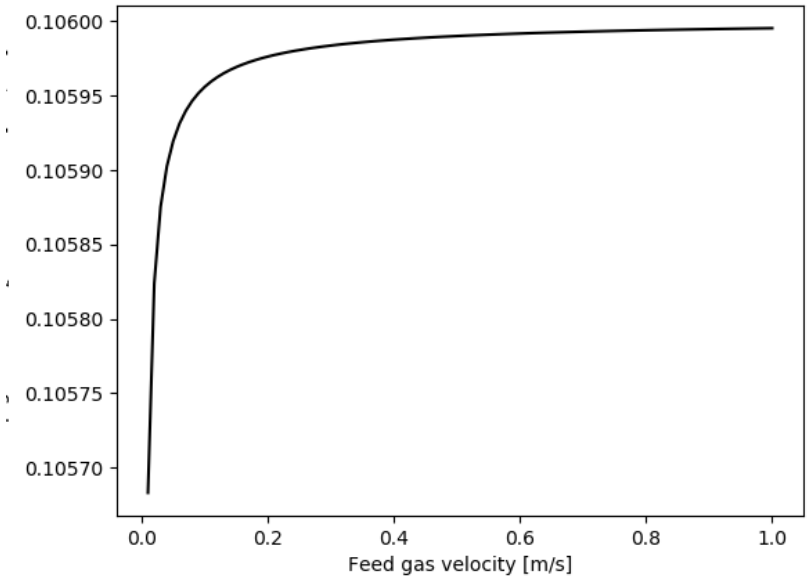

Figure 4.21 Effect of feed gas velocity on outlet H_2 concentration in the sweep gas

The code calculations results can be used as a guide for selection of operating conditions in the experiment. The feed gas velocity can be set in a range of 0.5 to 1 m/s. Considering the temperature features of the material, the operating temperature can vary from room temperature to moderately high temperature, for example, 300 °C. The inlet H_2 percentage can vary from <3% to 50%.

4.3.6 Experiment results

Before running the hydrogen-permeation experiment, a placebo test was carried out, filling the loop with N_2 instead of the Kr and H_2 gas mixture. The objective of the placebo test is to show the air-tightness of the loop. Because the permeability of N_2 through metal is significantly smaller than that of H_2, the pressure of the N_2 inside the loop should not decrease. The permeability of Kr though metal is even lower than that of N_2. Therefore, in the experiment, any observed pressure loss should be caused by H_2 permeating out of the loop. The measured temperatures at the six different locations and the pressure of the gas mixture inside the loop are plotted in Figure 4.22 and Figure 4.23, respectively.

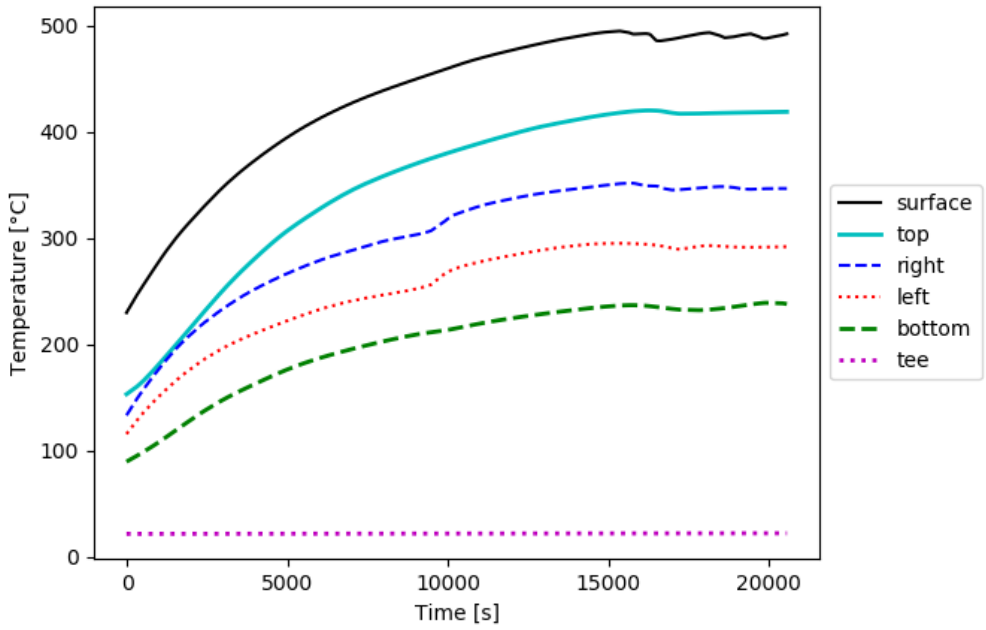

Figure 4.22 Measured temperatures in the N_2 placebo experiment

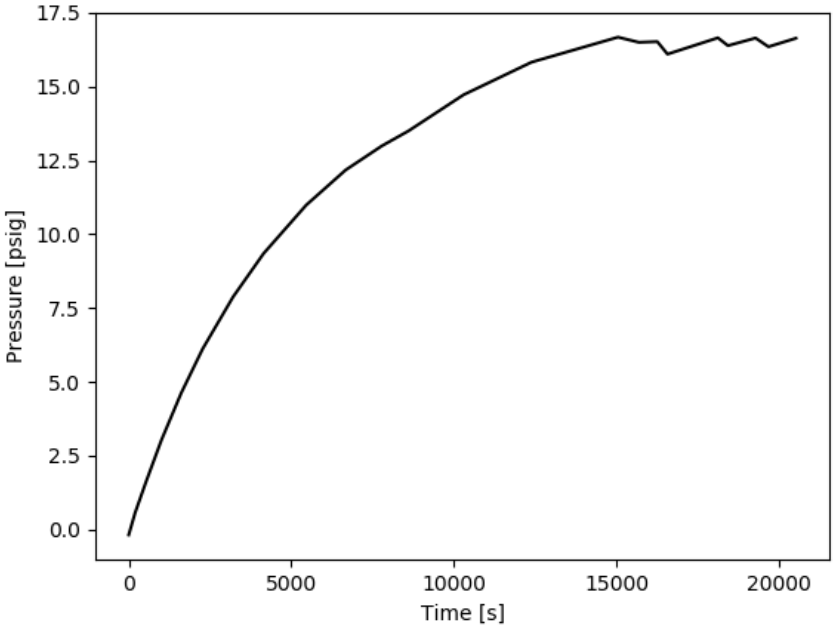

Figure 4.23 Measured pressure in the N_2 placebo experiment

The curves of both the temperatures and the pressure show some fluctuation after 15000 s. This might be caused by the contact of the tape heater and the facility surface becoming loose towards the end of the experiment. The issue was fixed later for the hydrogen-permeation experiments. From the comparison of the curves, it can be observed that the fluctuation of pressure most closely follows the surface temperature. This indicates that the surface temperature is the most accurate among all the six temperatures measured, in regards representing the development of the temperature of the gas mixture. Therefore, in the modeling of the experiment, the surface temperature is adopted as the temperature of the outer surface of the tritium removal facility to calculate the gas mixture temperature.

For the hydrogen-permeation experiment, two runs were carried out. The first lasted for 6 hours and the second 10 hours. The pressure of the gas mixture inside the loop was measured, and so were the temperatures of the six locations. The measured data are plotted in Figure 4.24 to Figure 4.27. It can be observed that during the 6-hour run, the pressure was not measured very well. This might be caused by the loose contact of the electronic wire of the pressure transducer. The issue was fixed in the 10-hour run.

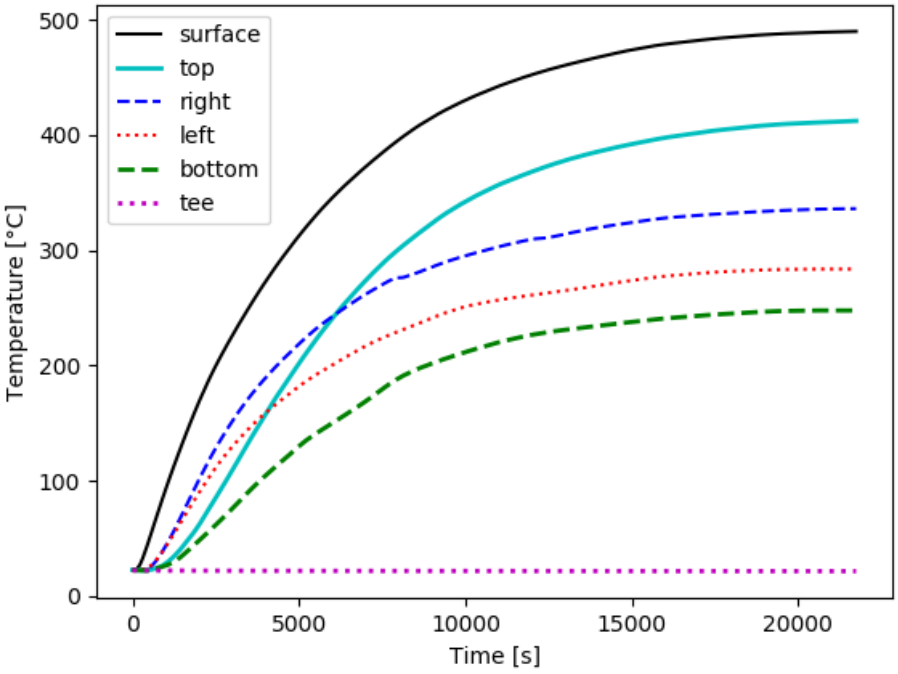

Figure 4.24. Temperatures at various locations (6-hour run)

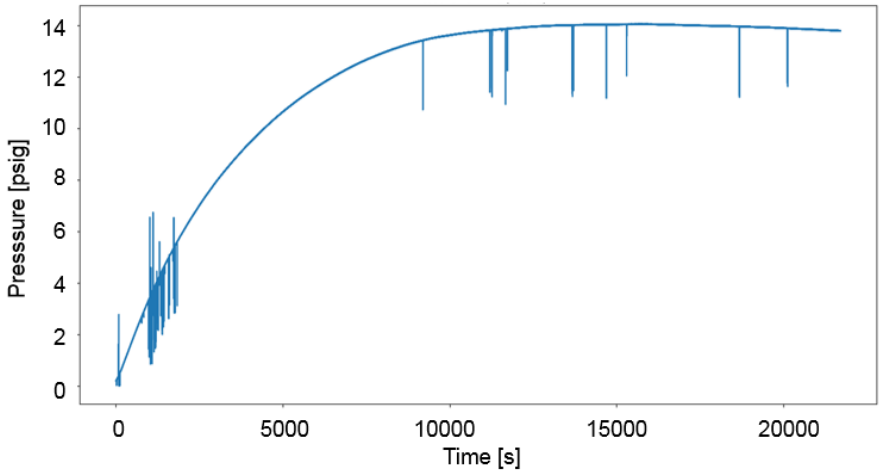

Figure 4.25. The pressure of the gas mixture (6-hour run)

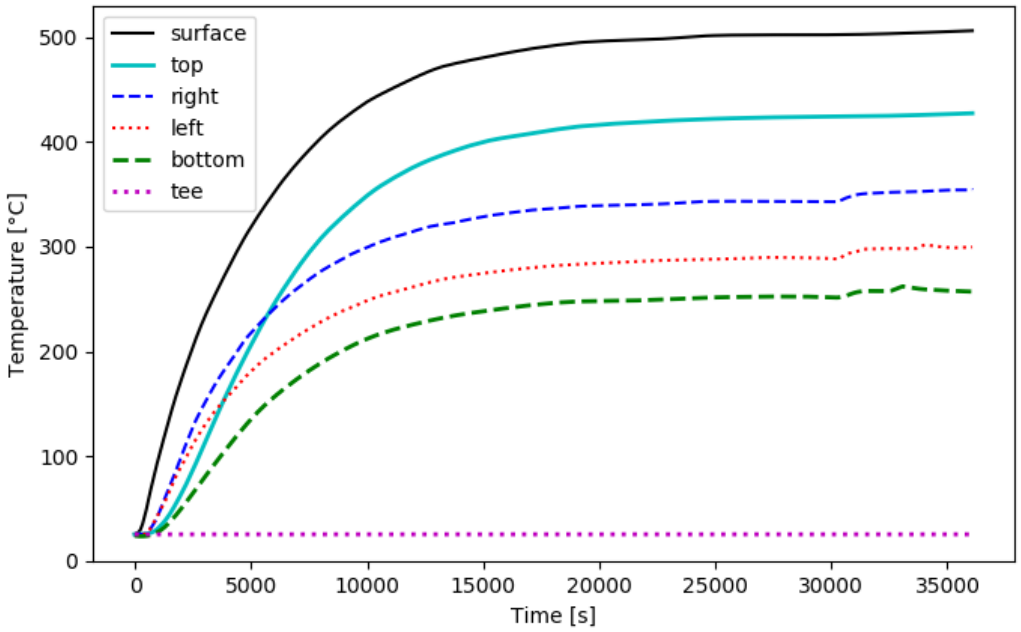

Figure 4.26. Temperatures at various locations (10-hour run)

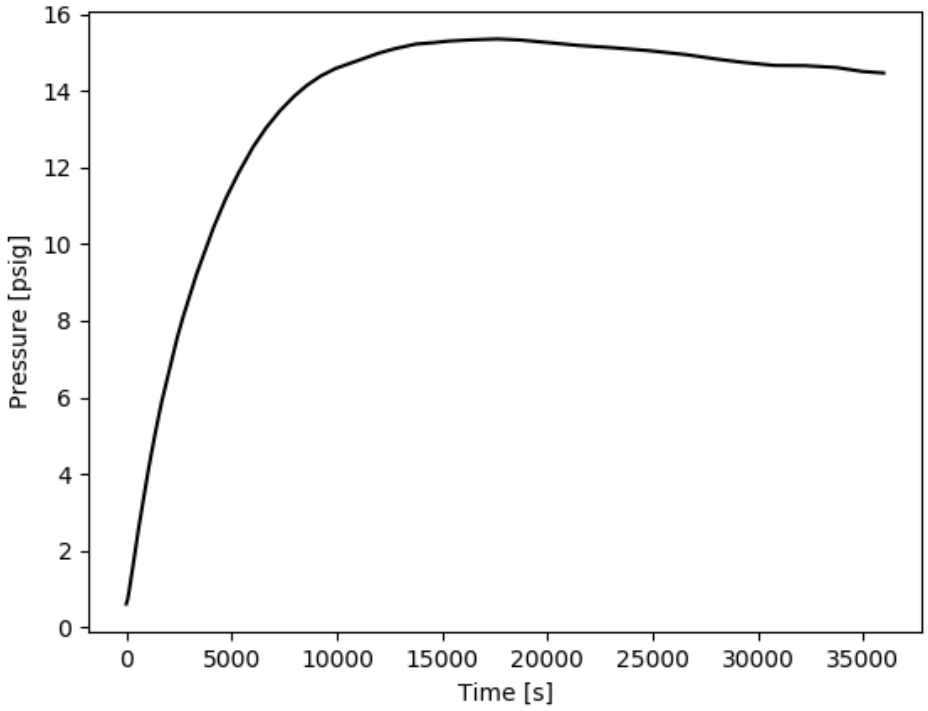

Figure 4.27. The pressure of the gas mixture (10-hour run)

During the early stage of the experiment, the temperature of the gas mixture inside the tritium removal facility rose quickly under the heating of the tape heater. After a few hours, the increase of temperature slowed down, but still had not reached a steady state. The pressure at first increased due to the temperature increase of the gas mixture in a confined volume. As the temperature tended to level out, however, the pressure stopped increasing in proportion to the temperature and even started to drop. In the pressure plot from the 6-hour run, it can be observed that the curve turns downward after 15000 s. In the pressure plot from the 10-hour run, this decrease in the pressure can be seen more clearly with the extension of the experiment time. The drop in the Kr + H_2 gas mixture pressure was caused by the H_2 permeation.

Modeling of the 10-hour run was carried out using the LMSPD code. Measured surface temperature is used as the temperature of the facility outer surface. The temperature is assumed to be uniform across the tritium removal facility outer surface. The heating power is assumed to be uniform across the tape heater and steady at 624 W throughout the experiment. Based on the geometry of the facility and the flow rate of the gas mixture inside the loop, heat transfer coefficients were calculated for the facility wall and the gas mixture. A heat transfer code was written in Python and the temperature of the gas mixture was then calculated, as plotted in Figure 4.28.

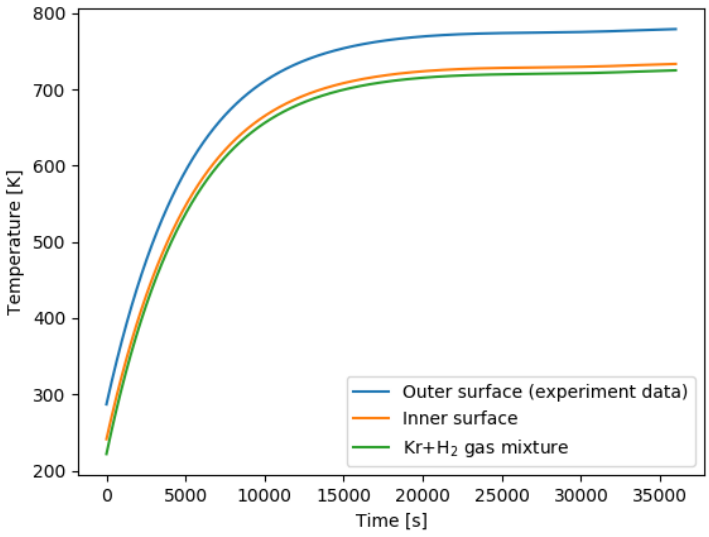

Figure 4.28 Calculated temperatures of the H_2 permeation experiment

Taking both the temperature effect on the pressure and the hydrogen permeation out of the loop, the pressure of the gas mixture was calculated and plotted in Figure 4.29. The difference between the calculation results and the experimental data is within 2.33%. From the comparison, the developed LMSPD code was verified for the cross-flow tritium removal facility fabricated with stainless steel 316.

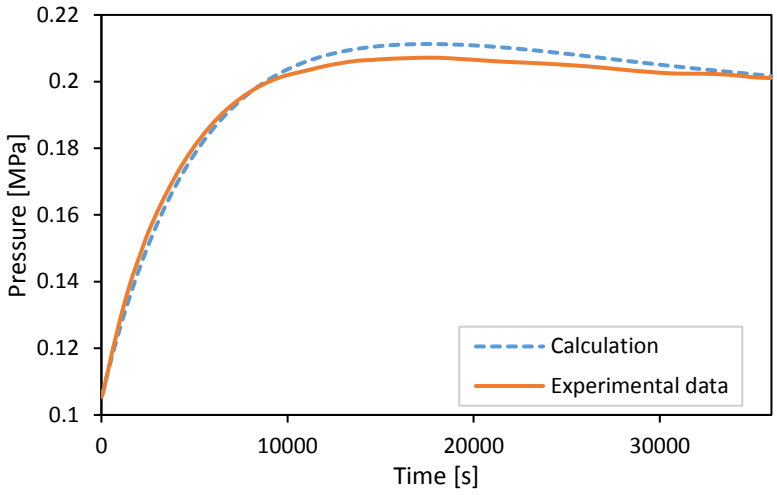

Figure 4.29. Calculated pressure of the gas mixture compared with the experimental data

Because the experiment loop was not insulated in hydrogen permeation barriers, the probability of H_2 escaping the loop into the surrounding environment instead of into the sweep gas should be considered. Figure 4.30 plots the permeability of H_2 through the structure walls at different temperatures. At room temperature, the value of H_2 permeability is 1/34 of that at 300 °C and 1/61 of that at 400 °C. The measured temperature at the location away from the tritium removal facility shows that the temperature of the gas mixture in the rest of the loop is well below that in the heated tritium removal facility. Comparing the H_2 permeability values at different temperatures, the amount of H_2 that escaped at other locations of the loop can be neglected.

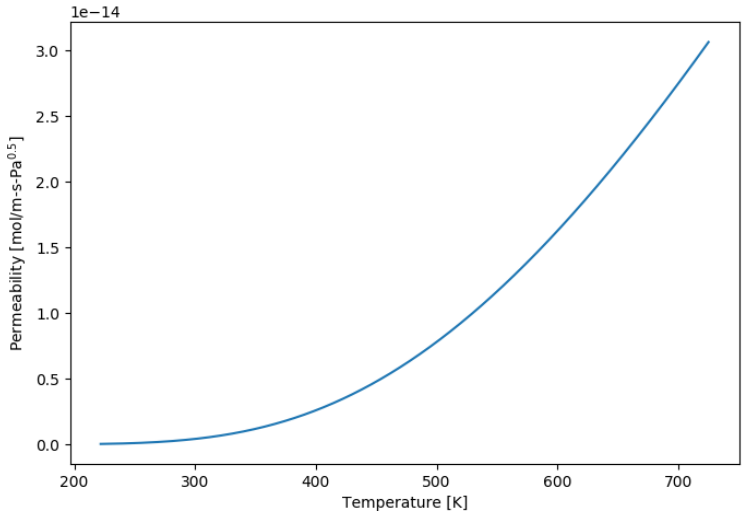

Figure 4.30 H_2 permeability through stainless steel at different temperatures

4.3.7 Design of the validation experiment using molten salt

For the experiment using molten salt as the H_2 carrier, a schematic of the loop is shown in Figure 4.31. The experimental setup consists of a molten salt loop, a H_2 loop and an Ar purging gas loop. FLiNaK is the selected molten salt material. FLiNaK is pumped through a loop, which consists of a H_2 addition facility and a H_2 removal facility. H_2 dissolves into the molten salt in the H_2 addition facility, and part of the H_2 dissolved is removed in the H_2 removal facility. The remainder circles in the loop with the molten salt. The H_2 carried out by the purging gas from the removal facility is quantitatively analyzed by a hydrogen sensor, which will probably be a GC. The mixed gas is then vented out through a ventilation hood. At equilibrium, the rate of H_2 dissolving into FLiNaK equals the H_2 flow rate at the molten salt inlet of the removal facility. By recording the H_2 flow rate in the outlet purging gas during the steady-state operation, the overall mass transfer coefficient of the experiment facility can be calculated. The results can be scaled up to obtain the removal effectiveness for the full-scale tritium removal facility.

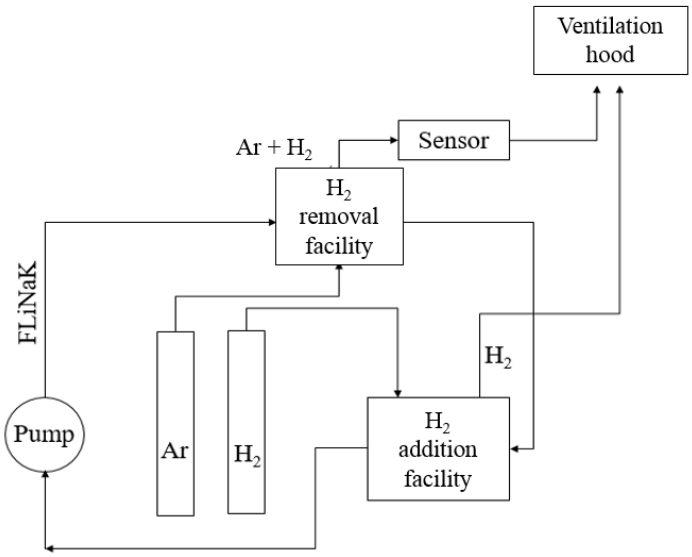

Figure 4.31 Schematic of the H_2 removal validation experiment with molten salt

Figure 4.32 shows a CAD drawing of the test section of molten salt. This experiment will take advantage of the FLiNaK loop in the lab, which is designed to investigate the performance of DRACS in FHRs [100]. The test section shown here will be connected to the existing loop via flanges. The experiment loop section will share pumps, heaters, flowmeters, thermocouples, and pressure transducers with the existing High-Temperature DRACS Test Facility (HTDF). NPS 1.5″ stainless steel 316H pipes will be used to match existing facility pipes. Thermal insulation will be applied around the pipes and facilities to avoid salt freezing due to heat loss. The main facilities in the testing loop are the H_2 addition facility and the H_2 removal facility. The two are identical in geometry and are connected by flanges. The short distance between the two facilities is intended to minimize the H_2 leakage from the molten salt. An ultrasonic flowmeter will be installed on the loop to monitor the molten salt flow rate. To avoid molten salt leakage, flanges and elbows will be directly welded to the pipes.

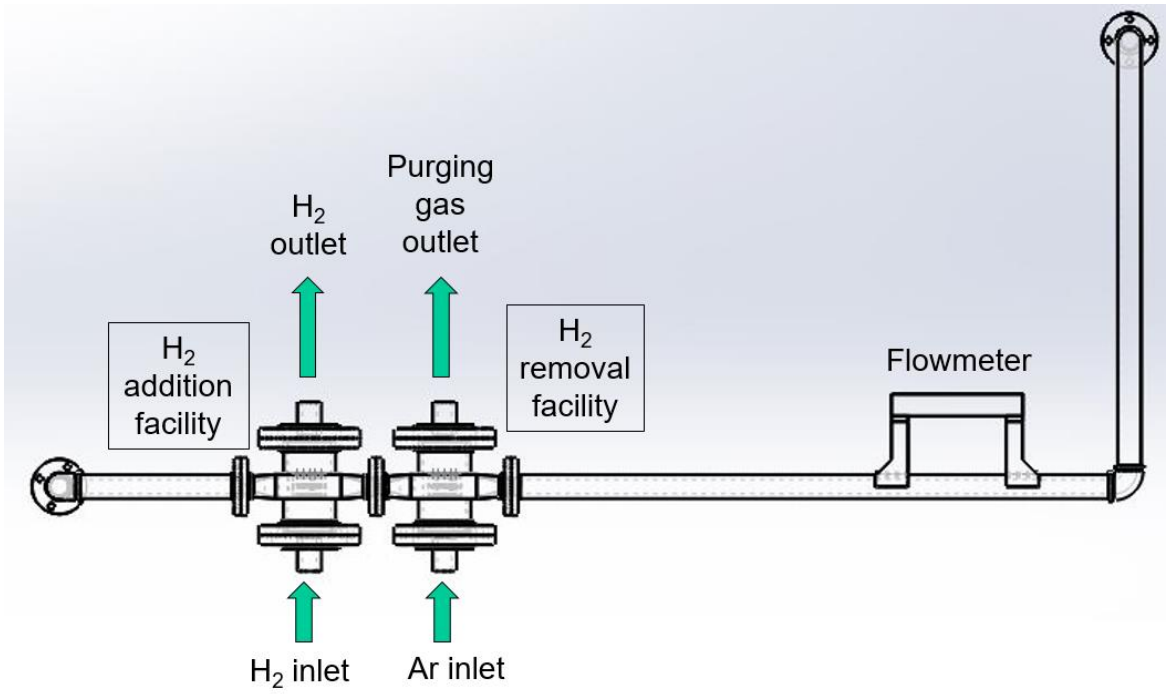

Figure 4.32 Design of test section in the molten salt loop

The gas lines are shown in Figure 4.33 and Figure 4.34. The H_2 addition gas line is connected through the H_2 addition facility. The Ar purging gas line is connected through the H_2 removal facility. Hoses and ¼-inch tubes will be used to connect gas cylinders and the facilities. Table 4.10 explains the components of the loops.

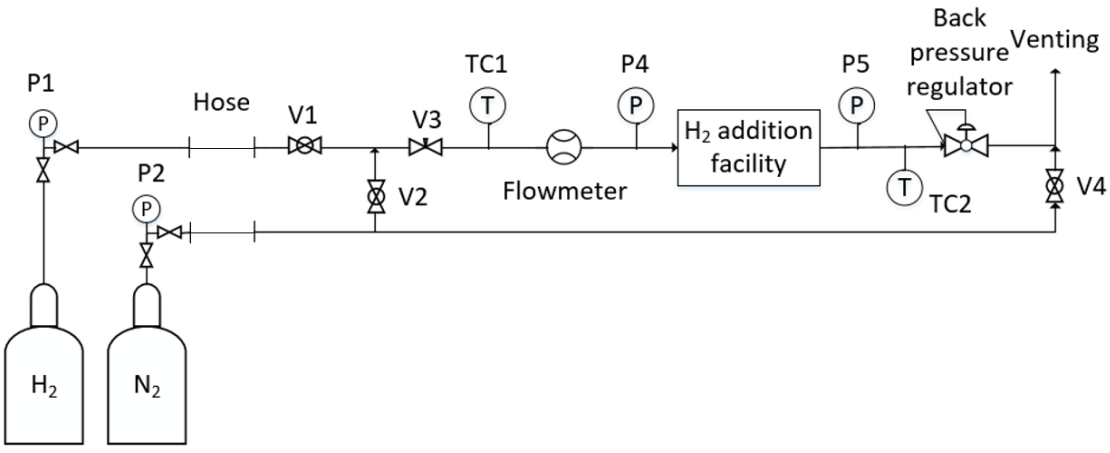

Figure 4.33 Schematic of the H_2 addition gas line

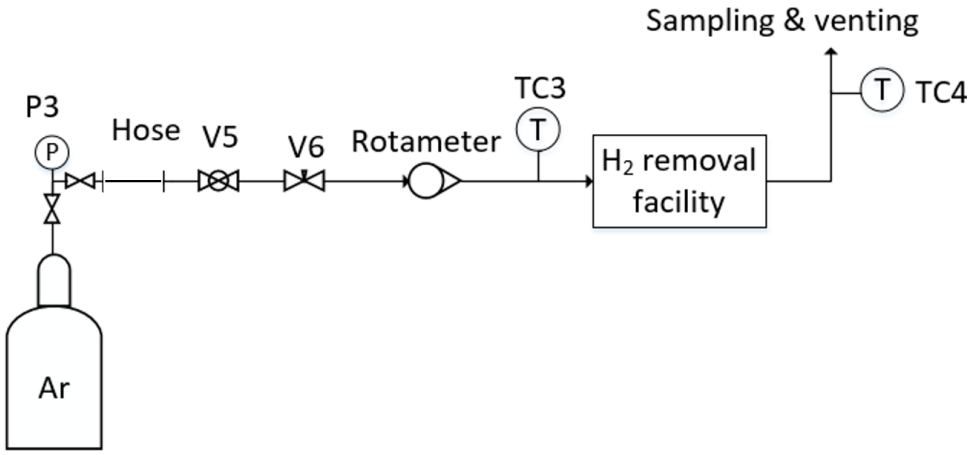

Figure 4.34 Schematic of the Ar purging gas line

Because of the delay in loop construction, the experiment using molten salt has not been set up. However, in the future, if permitted, after the FLiNaK loop is completed and in operation, the experiment can be setup and carried out. Computer simulation of the experiment will be performed, and the experimental data and the simulation results will be compared.

Table 4.10 Table of loop components

Denotation	Component type	Location	Function
V1	Ball valve	H_2 addition gas line	Shut-off valve for H_2 gas cylinder
V2	Ball valve	H_2 addition gas line	Shut-off valve for N_2 gas purging line
V3	Needle valve	H_2 addition gas line	Control and adjust H_2/N_2 flow rate
V4	Ball valve	H_2 addition gas line	Shut-off valve for N_2 gas venting line
V5	Ball valve	Ar purging gas line	Shut-off valve for Ar gas cylinder
V6	Needle valve	Ar purging gas line	Control and adjust Ar flow rate
TC1	Thermocouple	H_2 addition gas line	Monitor and record H_2/N_2 temperature near the Flowmeter
TC2	Thermocouple	H_2 addition gas line	Monitor and record H_2/N_2 temperature near P5
TC3	Thermocouple	Ar purging gas line	Monitor and record Ar temperature near the Rotameter
TC4	Thermocouple	Ar purging gas line	Monitor and record out-coming purging gas temperature near the sampling station
P1	Pressure regulator	H_2 addition gas line	Pressure regulator for H_2 gas cylinder
P2	Pressure regulator	H_2 addition gas line	Pressure regulator for N_2 gas cylinder
P3	Pressure regulator	Ar purging gas line	Pressure regulator for Ar gas cylinder
P4	Pressure transducer	H_2 addition gas line	Monitor and record H_2 gas line pressure before the H_2 addition facility
P5	Pressure transducer	H_2 addition gas line	Monitor and record H_2 gas line pressure after the H_2 addition facility
Back pressure regulator	Pressure regulator	H_2 addition gas line	Control H_2/N_2 loop pressure (coupling with P1/P2); release pressure before exhausted gas is vented
Flowmeter	Flowmeter	H_2 addition gas line	Monitor and record H_2/N_2 flow rate
Rotameter	Flowmeter	Ar purging gas line	Monitor and record Ar flow rate
Hose	Flexible hose	Ar purging gas line	Connect gas cylinders and main loops

4.4 Performance evaluation of the cross-flow tritium removal facility

To evaluate the effectiveness and efficiency of the designed cross-flow tritium removal facility in the molten salt reactor, a calculation using the LMSPD code was performed. The dimensions and flow configurations of the cross-flow tritium removal facility are from Table 3.2. The calculated tritium removal rates of the two configurations are listed in Table 4.11. From the results, it can be seen that configuration A performed better than configuration B, by almost 13% in the tritium removal rate under the condition of the same tritium inlet concentration.

Table 4.11 Tritium removal rate of the tritium removal facility

Configuration	Tritium removal rate [%]
A	66.58
B	53.72

4.5 Summary of the tritium analysis code and experimental validation

In this part of the study, a novel mass transport calculation method was developed based on the LMSPD, and the method was validated against hydrogen permeation experiments. Although comparison of the code calculation results with the experimental data in the literature shows greater discrepancy at low temperatures, they agree well at operating temperatures of the FHR. The comparison validates the correctness of the LMSPD method.

The LMSPD method was further validated using the data from a laboratory-scale gas-loop hydrogen extraction experiment. This experiment is the first one of the two experiments designed for validating the effectiveness and efficiency of the cross-flow tritium removal facility. The gas-loop experiment was performed as a testing experiment for the molten salt-loop experiment. Kr was used as a surrogate for the molten salt and functioned as a carrier gas of H_2. The gas mixture was circulated through a laboratory-scale cross-flow tritium removal facility inside a closed loop. The pressure of the gas mixture was recorded, and it was observed clearly that H_2 permeates out of the loop from the tube bank. The experiment was modeled using the LMSPD code and the code

calculation results are consistent with the experimental data. The LMSPD code was then used to evaluate the cross-flow tritium removal facility designed for the FHR systems, finding that the designs were able to achieve above 50% tritium removal.

There are some limitations to the gas-loop experiment. One of the most significant ones is the difference in properties between molten salts and Kr gas. The diffusive and convective transport of hydrogen in molten salts cannot be fully represented in a carrier gas. Therefore, to evaluate fully the performance of the cross-flow tritium removal facility, a molten salt-loop experiment was designed. H_2 will first be added to the molten salt via diffusion through a hydrogen addition facility before it is removed in the hydrogen removal facility. However, due to time constraints, the molten salt-loop experiment has not been carried out by the time this dissertation is completed.

Chapter 5. Summary, Conclusions, and Future Work

The principal objective of the current research is to propose a solution for the tritium generation challenge in advanced nuclear reactors such as FHRs. Topics that this study tries to address include evaluation of the health impacts of released tritium on the public, proposing a tritium control and mitigation strategy, development of a tritium transport calculation method, and experimental validation of the proposed tritium removal facility.

Governmental regulations on public doses of tritium and radioactive materials were reviewed here, as were studies on the dispersion and transport of human-sourced tritium released into the environment. It was discovered that limited research had been carried out on the health impact of chronic airborne tritium release to residents near the tritium release sources. Therefore, to evaluate the impact of tritium released from FHRs on the public health, the dispersion of airborne tritium was studied, and the doses public individuals would receive from tritium release were calculated. The meteorological conditions that favor lowering the maximum individual dose were discovered. These include low temperature, upwind direction, high wind speed, and high relative humidity. In addition, it is suggested that several measures can be taken to reduce the negative impact of tritium release on local residents such as locating residents away from the tritium-release facility, avoiding the downwind direction, and increasing the height of the tritium release point.

The uncertainty analysis of the dose assessment shows that climate change could significantly influence the health impact to the public from FHR tritium release. For a selected location, its suitability for FHR construction and operation might change with the change of local meteorological conditions over time. In addition, it is discovered from the sensitivity study that for different geological locations, the contribution from each meteorological parameter to the dose equivalent vary greatly. Therefore, dose assessment for the future should include the effects of

climate change, and uncertainty analysis should be performed to address the significant uncertainties in meteorological parameters.

To limit the leakage rate of tritium to an allowable level, a tritium control and mitigation system was designed for advanced nuclear reactor systems. The system consists of four main components: namely, redox control of the primary coolant, a cross-flow tritium removal facility, an IHX, possibly with double-wall design and tritium permeation barrier coatings applied to structural materials as necessary. The double-wall IHX was designed as an optional component of the tritium control and mitigation system, to be used if necessary. It was designed to minimize tritium leakage into the secondary (or intermediate) coolant through the large surface area of the IHX. In this IHX design, the molten-salt coolant flows through the gaps between the two tube walls, or tritium-permeation-barrier materials are filled in the tube gaps. The materials in the tube gaps prevent tritium from leaking into the secondary coolant.

To further minimize tritium leaking into the surrounding environment through the structural materials, tritium-permeation-barrier coatings can be applied as necessary. The tritium permeabilities of several candidates were reviewed, and it was found that Al_2O_3 is a promising material for this purpose. One limitation of using tritium permeation barriers is that the barrier coating requires a high level of integrity. Cracks and other defects of the coating significantly reduce tritium permeation reduction. In practical operation, this could be a challenge, as the integrity of the coating may be hard to maintain, especially at high temperatures.

A preliminary economic analysis was carried out to study the construction and operating cost of the cross-flow tritium removal facility. It was discovered that the operation cost can be lowered if a fraction of the primary coolant flow, instead of the entire primary coolant flow, is directed to flow through the tritium removal facility. The costs of the two-loop and three-loop FHR designs were compared. The AHTR pre-conceptual design was used as a prototype for the three-loop design. In the AHTR design, the intermediate loop functions as a buffer loop for tritium permeation from the primary loop to the power-generation cycle loop. It is shown that, with the elimination of the intermediate loop, the two-loop FHR design has economic advantages over the original three-loop design.

From the economic analysis, it was discovered that, of the tritium control strategies, the cross-flow tritium removal facility is the most economical. The cross-flow configuration was designed to increase the turbulence of the molten salt and to thereby increase the efficiency of tritium removal. Since mass transfer in the cross-flow configuration was rarely model by computer codes, a novel tritium transport calculation method based on the logarithmic mean square root of the partial-pressure difference was developed to evaluate the performance of the designed facility. The method was implemented in MATLAB. The calculation results of the LMSPD codes were compared with the calculation results from a code using the FVM and experimental data of hydrogen permeation through a nickel tube. The results agree well.

To verify the developed LMSPD code with the cross-flow tritium removal facility fabricated with stainless steel, two validation experiments were designed with H_2 as a surrogate for T_2: one with reactor off-gas Kr as the fluid and the other with molten salt FLiNaK as the fluid and solvent of H_2. The experiment with the off-gas Kr was carried out at the University of Idaho. A laboratory-scale cross-flow tritium removal facility that consists of 27 tubes in the tube bank was fabricated, and a laboratory-scale experimental loop was constructed. Two runs were carried out, lasting 6 hours and 10 hours. The 10-hour run was modeled using the LMSPD code, and the calculation results agreed well with the experimental data. An experiment using the molten-salt FLiNaK will be carried out if resources are available in the future.

For the future investigation of the tritium challenge in advanced nuclear reactors, studies can be performed in several fields. First, current tritium transport coefficients in several types of molten salts (for example, FLiNaK and FLiBe) reported in the literature exhibit significant discrepancies. Both theoretical and experimental work is necessary to help understand tritium diffusion in molten salts. Second, tritium dispersion in the atmosphere requires further investigation—especially wet deposition. The influence of precipitation on tritium wash-out lacks theoretical support and experimental validation. Third, uncertainty analysis and sensitivity study of the tritium dispersion process are of interest as well. In this study the uncertainty of the meteorological parameters were addressed, but not much investigation had been performed on the uncertainty in the dispersion process itself. Fourth, in this study, a cross-flow tritium-removal strategy is proposed and

evaluated. It is only one of the many possible strategies for tritium mitigation. Other strategies can be developed and evaluated, as well. Finally, experiments on hydrogen (or tritium if safety conditions permit) extraction from molten salts need to be performed to validate further the cross-flow configuration and the LMSPD code.

BIBLIOGRAPHY

[1] C.W. Forsberg, L.W. Hu, P.F. Peterson, and K. Sridharan, "Fluoride-salt-cooled high-temperature reactors (FHRs) for base-load and peak electricity, grid stabilization, and process heat," Department of Nuclear Science and Engineering, Massachusetts Institute of Technology, Cambridge, MA, MIT-ANP-TR-147, 2012.

[2] D.F. Williams, "Assessment of candidate molten salt coolants for the advanced high temperature reactor (AHTR)," ORNL/TM-2006/12, ORNL, 2006.

[3] D.T. Ingersoll, "Status of preconceptual design of the advanced high-temperature reactor (AHTR)," ORNL/TM-2004/104, ORNL, 2004.

[4] C. Anderades, A.T. Cisneros, J.K. Choi, Y.K. Chong, M. Fratoni, S. Hhong, L.R. Huddar, K.D. Huff, D.L. Krumwiede, M.R. Laufer, M.Munk, R.O. Scarlat, N. Zweibaum, E. Greenspan, and P.F. Peterson, "Technical description of the 'Mark 1' pebble-bed fluoride-salt-cooled high-temperature reactor (PB-FHR) power plant," UCBTH-14-002, University of California-Berkeley, 2014.

[5] P. Sabharwall, H. Schmutz, C. Stoots, and G. Griffith, "Tritium production and permeation in high-temperature reactor systems," *Proceedings of the ASME 2013 Heat Transfer Summer Conference*, American Society of Mechanical Engineers, 2013.

[6] "Management of waste containing tritium and carbon-14," Technical Reports Series No. 421, International Atomic Energy Agency, (2004).

[7] J.D. Stempien, "Tritium transport, corrosion, and fuel performance modeling in the fluoride salt-cooled high-temperature reactor (FHR)," PhD diss., Massachusetts Institute of Technology, 2015.

[8] M.F. Simpson, G.R. Smolik, J.P. Sharpe, R.A. Anderl, D.A. Petti, Y. Hatano, M.Hara, Y. Oya, S. Fukada, S. Tanaka, T. Terai, and D. Sze, "Quantitative measurement of beryllium-controlled redox of hydrogen fluoride in molten FLiBe," *Fusion Engineering and Design* **81**, pp. 541-547, 2006.

[9] S. Fukada, A. Morisaki, A. Sagara, and T. Terai, "Control of tritium in FFHR-2 self-cooled FLiBe blanket," *Fusion Engineering and Design* **81**, pp. 477-483, 2006.

[10] International Atomic Energy Agency, Code on the Safety of Nuclear Power Plants: Siting, Safety Series No. 50-C-S (Rev. 1), IAEA, Vienna, 1988.

[11] P. Calderoni, P. Sharpe, M. Hara, and Y. Oya, "Measurement of tritium permeation in FLiBe ($2LiF–BeF_2$)," *Fusion Engineering and Design* **83**, pp. 1331-1334, 2008.

[12] A.P. Malinauskas and D.M. Richardson, "The solubilities of hydrogen, deuterium, and helium in molten Li_2BeF_4," *Industrial & Engineering Chemistry Fundamentals* **13**, pp. 242-245, 1974.

[13] R.A. Anderl, S. Fukada, G. R. Smolik, R. J. Pawelko, S. T. Schuetz, J. P. Sharpe, and B. J. Merrill, "Deuterium/tritium behavior in FLiBe and FLiBe-facing materials," *Journal of Nuclear Materials* **329**, pp. 1327-1331, 2004.

[14] S. Fukada and Akio Morisaki, "Hydrogen permeability through a mixed molten salt of LiF, NaF and KF (Flinak) as a heat-transfer fluid," *Journal of Nuclear Materials* **358**, pp. 235-242, 2006.

[15] Y. Zeng, L. Du, S. Wu, Y. Qian, G. Wang, Y. Huang, H. Zhu, and W. Liu, "Permeability of hydrogen in molten salt FLiNaK (LiF-NaF-KF)," *Nuclear Energy Science and Engineering* **38**, No. 2, 2015.

[16] H.D. Röhrig, R. Hecker, J. Blumensaat, and J. Schaefer, "Studies on the permeation of hydrogen and tritium in nuclear process heat installations," *Nuclear Engineering and Design* **34**, pp. 157-167, 1975.

[17] Peterson, S.R., "Historical doses from tritiated water and tritiated hydrogen gas released to the atmosphere from Lawrence Livermore National Laboratory (LLNL). Part 2. LLNL Annual Site-specific Data, 1953 -2005," UCRL-TR-211722-REV-1, 2007.

[18] X. Wu, S. Zhang, S. Shi, X. Sun, D. Holcomb, R. Christensen, and P. Sabharwall, "Tritium release limit for fluoride salt-cooled high-temperature reactors," *Proceedings of ANS Winter Meeting*, pp. 6-10. 2016.

[19] L.M. Dorfman and B.A. Hemmer, "Ion-pair yield of the tritium-oxygen reaction," *The Journal of Chemical Physics* **22**(9), pp. 1555, 1954.

[20] https://www.irsn.fr/EN/Research/publications-documentation/radionuclides-sheets/environment/Pages/Tritium-environment.aspx, as accessed on April 1, 2019.

[21] R.P. Bell, M.W. Davis, K.Y. Wong, and S. Joseph, "Development of a tritium dispersion code," *Fusion Technology* **8**(2P2), pp. 2582-2586, 1985.

[22] J.-S. Chae and G. Kim, "Dispersion and removal characteristics of tritium originated from nuclear power plants in the atmosphere," *Journal of environmental radioactivity* **192**, pp. 524-531, 2018.

[23] T. Okai and Y. Takashima, "Tritium concentrations in atmospheric water vapor, hydrogen and hydrocarbons in Fukuoka," *International Journal of Radiation Applications and Instrumentation. Part A. Applied Radiation and Isotopes*, **42**(4), pp. 389-393, 1991.

[24] Code of Federal Regulations (10 CFR 20.1003) (2015).

[25] "Backgrounder on tritium, radiation protection limits, and drinking water standards," http://www.nrc.gov/reading-rm/doc-collections/fact-sheets/tritium-radiation-fs.html, accessed on July 2, 2016.

[26] Code of Federal Regulations, Title 40, "Protection of environment," Section 141.16, "Maximum Contaminant Levels for Beta Particle and Photon Radioactivity from Man-Made Sources," 2000.

[27] Code of Federal Regulations, 10 CFR Part 50, 2016.

[28] "Investigation of the environmental fate of tritium in the atmosphere," Canadian Nuclear Safety Commission, 2014.

[29] "Radiation Protection Regulations," SOR/2000-203, Consolidation, Canada, 2016.

[30] A.C. Chamberlain and A.E.J. Eggleton, "Washout of tritiated water vapor by rain," *International Journal of Air Water Pollution* **8**, pp. 135, 1964.

[31] P.I. Barry, "Maximum permissible concentrations of radioactive nuclides in airborne effluents from nuclear reactors," Canadian Report CKER-1098, 1962.

[32] J.O. Blomcke, "Management of fission product tritium in fuel processing wastes," USAEC Report ORNL-TM-851, Oak Ridge National Laboratory, 1964.

[33] A. Doury, "Risks presented by the diffusion of large quantities of tritium in the atmosphere," in Seminaries sur la Protection Contre les Dangers du Tritium, Service Central de Protection Contre des Rayonnrnents Ionissants, pp. 17, le Veshet, April 16-18, 1964.

[34] J.Y. Yang and L.H. Gevantman. "Tritium-β-radiation-induced isotopic exchange in the T_2-H_2O system," Report USNRDL-TR-471, Naval Radiological Defense Laboratory, 1960.

[35] R.E. Blanco and J.O. Blomeke, "Survey of a site for a nuclear fuel processing plant and waste disposal area at Oak Ridge," ORNL-TM-1748, Oak Ridge National Laboratory, 1967.

[36] C.W. Forsberg, P.F. Peterson and R.A. Kochendarfer, "design options for the advanced high-temperature reactor," *Proceedings of ICAPP 2008* **8**, pp. 8, 2008.

[37] V.K. Varma, D.E. Holcomb, F.J. Peretz, E.C. Bradley, D. Ilas, A.L. Qualls, and N.M. Zaharia, "AHTR mechanical, structural and neutronic preconceptual design," ORNL/TM-2012/320, 2012.

[38] S.B. Kim, M. Stuart, M. Bredlaw, A. Festarini, and D. Beaton, "HT to HTO conversion and field experiments near Darlington Nuclear Power Generating Station (DNPGS) site," *Journal of Environmental Radioactivity* **132**, pp. 73, 2014.

[39] "Investigation of the environmental fate of tritium in the atmosphere," INFO-0792, Canadian Nuclear Safety Commission (2009).

[40] D.J. Jacobs, "Source of tritium and its behavior upon release to the environment," ORNL/NSIC-39 (1968).

[41] A. Meneghetti, B.E.J. Bodmann, and M.T.M.B. de Vilhena, "Tritium dispersion around the Angra nuclear power plant: boundary simplification by diffeomorph conformal transformations," *Journal of Computational and Theoretical Transport*, pp. 1-13, 2018.

[42] K.Y. Matsuura, S.C. Nakamura, and H. Katagiri, "Levels of tritium concentration in the environmental samples around JAERI Tokai," *Journal of Radioanalytical and Nuclear Chemistry*, **197**(2), pp. 295-307, 1995.

[43] H. Fujita, Y. Kokubun, and J. Koarashi, "Environmental tritium in the vicinity of Tokai reprocessing plant," *Journal of nuclear science and technology*, **44**(11), pp. 1474-1480, 2007.

[44] "Modelling the environmental transport of tritium in the vicinity of long-term atmospheric and sub-surface Sources," International Atomic Energy Agency, 2002.

[45] V.K. Varakhedkar, A. Baburajan, S.V. Vanave, D.D. Rao, P.M. Ravi, and R.M. Tripathi, "Evaluation of tritium dispersion in the atmosphere by Risψ Mesoscale Puff modeling systems using on-site meteorological parameters for the nuclear site Tarapur, India," *Radiation Protection and Environment*, **39**(1), pp. 30, 2016.

[46] A.L. Kock and D.M. Hamby, "Variations in environmental tritium dose estimates due to meteorological data averaging and uncertainties in pathway model parameters," *Environmental monitoring and assessment*, **53**(2), pp. 321-335, 1998.

[47] S. Fukada, Y. Edao, S. Yamaguti, and T. Norimatsu, "Tritium recovery system for Li-Pb loop of inertial fusion reactor," *Fusion Engineering and Design* **83**, pp. 747-751, 2008.

[48] D.W. Green and R.H. Perry, Perry's Chemical Engineers' Handbook (7th ed.), New York: McGraw-Hill, 1997.

[49] R.E. Buxbaum, "The Use of zirconium-palladium windows for the separation of tritium from the liquid metal breeder-blanket of a fusion reactor," *Separation Science and Technology* **18**, pp. 251-1273, 1983.

[50] C. Hsu and R.E. Buxbaum, "Palladium-catalyzed oxidative diffusion for tritium extraction from breeder-blanket fluids at low concentrations," *Journal of Nuclear Materials* **141**, pp.238-243, 1986.

[51] C.W. Forsberg, S. Lam, D.M. Carpenter, D.G. Whyte, R. Scarlat, C. Contescu, L. Wei, J. Stempien, and E. Blandford, "Tritium control and capture in salt-cooled fission and fusion reactors: status, challenges, and path forward," *Nuclear Technology* **197**(2), pp. 119-139, 2017.

[52] S. Zhang, S. Shi, X. Wu, X. Sun, and R. Christensen, "Double-wall natural draft heat exchanger design for tritium control in FHRs," *Proceedings of the 25th International Conference on Nuclear Engineering*, 2017.

[53] X. Wu, "Design of a tritium mitigation and control system for fluoride-salt-cooled high-temperature reactor systems," Master Thesis, The Ohio State University, 2016.

[54] C.W. Forsberg and P.F. Peterson, "FHR, HTGR, and MSR pebble-bed reactors with multiple pebble sizes for fuel management and coolant cleanup," *Nuclear Technology*, pp. 1-7, 2019.

[55] A.Charalampos, A.T. Cisneros, J.K. Choi, A.Y.K. Chong, M. Fratoni, S. Hong, L.R. Huddar, K.D. Huff, J. Kendrick, D.L. Krumwiede, M.R. Laufer, M. Munk, R.O. Scarlat, N. Zweibaum, E. Greenspan, X. Wang, and P. Peterson, "Design summary of the Mark-I pebble-bed, fluoride salt-cooled, high-temperature reactor commercial power plant," *Nuclear Technology* **195**(3), pp. 223-238, 2016.

[56] A.V. Fedorov, A.J. Magielsen, and M.P. Stijkel, "Tritium permeation in EUROFER97 steel in EXOTIC-9/1 irradiation experiment," *Journal of Nuclear Materials* **448**(1-3), pp. 139-143, 2014.

[57] W.G. Luscher, D.J. Senor, K.K. Clayton, and G.R. Longhurst, "In situ measurement of tritium permeation through stainless steel," *Journal of Nuclear Materials* **437**(1-3), pp. 373-379, 2013.

[58] H. Nakamura, W. Shu, T. Hayashi, and M. Nishi, "Tritium permeation study through tungsten and nickel using pure tritium ion beam," *Journal of Nuclear Materials* **313**, pp. 679-684, 2003.

[59] A. Suzuki, T. Terai, and S. Tanaka, "Tritium release behavior from Li_2BeF_4 molten salt by permeation through structural materials," *Fusion Engineering and Design* **51**, pp. 863-868, 2000.

[60] T.F. Kempe, S.B. Russell, K.J. Donnelly, and H.J. Reilly, "International comparison of computer codes for modelling the dispersion and transfer of tritium released to the atmosphere." *Fusion Technology* **8**, pp. 2575-2581, 1985.

[61] S.B. Russell and G.L. Ogram, "ETMOD: a new environmental tritium model," *Fusion Technology* **21**, pp. 645-650, 1992.

[62] R.E. Moore, C.F. Baes III, L.M. McDowell-Boyer, A.P. Watson, F.O. Hoffman, J.C. Pleasant, and C.W. Miller, "AIRDOS-EPA: A computerized methodology for estimating environmental concentrations and dose to man from airborne releases of radionuclides," No. EPA--520/1-79-009, Environmental Protection Agency, 1979.

[63] C. Yu, D. LePoire, E. Gnanapragasam, J. Arnish, S. Kamboj, B.M. Biwer, J.J. Cheng, A. Zielen, S.Y. Chen, and T. Mo, "Development of probabilistic RESRAD 6.0 and RESRAD-BUILD 3.0 computer codes," US Nuclear Regulatory Commission, 2000.

[64] RESRAD Computer Code–Evaluation of Radioactively Contaminated Sites, ANL, 2009.

[65] https://www.energy.gov/ehss/genii, as accessed on April 1, 2019.

[66] B.A. Napier, GENII Version 2 Users' Guide, PNNL-14583, Rev. 3a, 2010.

[67] B.A. Napier, *GENII Version 2 Software Design Document, PNNL*-14584, Rev. 3, 2009.

[68] National Council on Radiation Protection and Measurements, "*Uncertainties in internal radiation dose assessment*," National Council on Radiation Protection and Measurements (NCRP), 2009.

[69] Y. Liu and N. Dinh, "Validation and uncertainty quantification for wall boiling closure relations in multiphase-CFD solver," *Nuclear Science and Engineering* **193**(1-2), pp. 81-99, 2019.

[70] Y. Liu, "Development of a data-driven analysis framework for boiling problems with multiphase-CFD solver," Ph.D. dissertation, North Carolina University, 2018.

[71] G. Briggs, "Diffusion estimation for small emissions ATDL, contribution file No. 97," Air Resources Atmospheric Turbulence and Diffusion Laboratory, NOAA, Oak Ridge, Tennessee, 1973.

[72] L. Bernstein, P. Bosch, O. Canziani, Z. Chen, R. Christ, O. Davidson, and W. Hare, "Climate change 2007: synthesis report: an assessment of the intergovernmental panel on climate change," IPCC, 2008.

[73] M.C. MacCracken, "Prospects for future climate change and the reasons for early action," *Journal of the Air & Waste Management Association*, **58**(6), pp. 735-786, 2008.

[74] E. Coffel and R. Horton, “Climate change and the impact of extreme temperatures on aviation." *Weather, Climate, and Society* **7**(1), pp. 94-102, 2015.

[75] H.-Y. An, Y.-H. Kang, S.-K. Song, and Y.-K. Kim, “Atmospheric dispersion characteristics of radioactive materials according to the local weather and emission conditions,” *Journal of Radiation Protection and Research* **41**(4), pp. 315-327, 2016.

[76] C.W. Kent, C.S.B. Grimmond, D. Gatey, and J.F. Barlow, “Assessing methods to extrapolate the vertical wind-speed profile from surface observations in a city centre during strong winds,” *Journal of Wind Engineering and Industrial Aerodynamics* **173**, pp. 100-111, 2018.

[77] C.W. Forsberg, S. Lam, D.M. Carpenter, D.G. Whyte, R. Scarlat, C. Contescu, L. Wei, J. Stempien, and E. Blandford, “Tritium control and capture in salt-cooled fission and fusion reactors: status, challenges, and path forward,” *Nuclear Technology* **197**(2), pp. 119-139, 2017.

[78] X. Wu, S. Shi, X. Sun, R. Christensen, and P. Sabharwall, “Tritium mitigation/control for advanced reactor system,” UM/THL-18-05, 2018.

[79] P.J. Brown and A.T. DeGaetano, “Trends in US surface humidity, 1930–2010,” *Journal of Applied Meteorology and Climatology* **52**(1), pp. 147-163, 2013.

[80] Y. Liu, N.T. Dinh, R.C. Smith, and X. Sun, “Uncertainty quantification of two-phase flow and boiling heat transfer simulations through a data-driven modular Bayesian approach,” *International Journal of Heat and Mass Transfer* **138**, pp. 1096-1116, 2019.

[81] S. Zhang, X. Wu, S. Shanbin, X. Sun, R. Christensen, and G. Yoder, “A coupled heat transfer and tritium mass transport model for a double-wall heat exchanger design for FHRs,” *Annals of Nuclear Energy* **122**, pp. 328-339, 2018.

[82] M. Taal, I. Bulatov, J. Klemeš, and P. Stehlík, “Cost estimation and energy price forecasts for economic evaluation of retrofit projects,” *Applied Thermal Engineering* **23**(14), pp. 1819-1835, 2003.

[83] http://www.usinflationcalculator.com/inflation/current-inflation-rates/, as accessed on 01/01/2017.

[84] https://www.atimetals.com/businesses/ATIFlatRolledProducts/Tools/Pages/Surcharge-History.aspx, as accessed on 01/01/2017.

[85] https://www.statista.com/statistics/183700/us-average-retail-electricity-price-since-1990/, as accessed on 01/01/2017.

[86] http://www.pcreml.com/rare-earth-pricing, as accessed on 01/01/2017.

[87] V.K. Varma, D.E. Holcomb, F.J. Peretz, E.C. Bradley, D. Ilas, A.L. Qualls, and N.M. Zaharia, "AHTR mechanical, structural, and neutronic preconceptual design," ORNL/TM-2012/320, Oak Ridge National Laboratory, 2012.

[88] R.E. Treybal, Mass transfer operations, New York: McGraw-Hill (1980).

[89] A.P. Sinha and P. De, *Mass transfer: principles and operations*, PHI Learning Pvt. Ltd, 2012.

[90] M. Wang, J. Song, X. Wu, X. Tan, B. Meng, and S. Liu, "Metallic nickel hollow fiber membranes for hydrogen separation at high temperatures," *Journal of Membrane Science* **509**, pp. 156-163, 2016.

[91] T.R. Marrero and E.A. Mason, "Gaseous diffusion coefficient," *Journal of Physics Chemistry Reference Data* **1**(1), 1972.

[92] COMSOL, Separation through dialysis, https://www.comsol.com/model/membrane-dialysis-258, accessed on 01/01/2017.

[93] D. Harvey, *Modern analytical chemistry*, New York: McGraw-Hill, 2000.

[94] Y. Kwon, *Handbook of essential pharmacokinetics, pharmacodynamics and drug metabolism for industrial scientists*, Springer Science & Business Media, 2001.

[95] https://en.wikipedia.org/wiki/Partition_coefficient#cite_note-1, accessed on June 30, 2017.

[96] S.K. Lee, Y.G. Ohn, and S.J. Noh, "Measurement of hydrogen permeation through nickel in the elevated temperature range of 450–850 °C," *Journal of the Korean Physical Society* **10**(63), pp. 1955-1961, 2013.

[97] L.H. Gevantman, "Solubility of selected gases in water," *Nitric Oxide (NO)* **308**(3), 2000.

[98] http://www.engineeringtoolbox.com/gases-solubility-water-d_1148.html, as accessed on 01/01/2019.

[99] B. Jähne, G. Heinz, and W. Dietrich, "Measurement of the diffusion coefficients of sparingly soluble gases in water," *Journal of Geophysical Research: Ocean*s **92**(C10), pp. 10767-10776, 1987.

[100] Q. Lv, H.C. Lin, I.H. Kim, X. Sun, R.N. Christensen, T.E. Blue, G. Yoder, D. Wilson, and P. Sabharwall, "DRACS thermal performance evaluation for FHR," *Annals of Nuclear Energy* **77**, pp. 115-128, 2015.

APPENDICES

Appendix A

LMSPD code

This code is a zero-dimensional (control-volume) black box type mass transfer calculation code. The example shown in this appendix is the modeling of the H_2 permeation experiment through a nickel tube. This experiment is described in Section 4.2.

```
% Method: LMSPD
% This is an example of H2 permeation through Ni
% Wang, M., Song, J., Wu, X., Tan, X., Meng, B., Liu, S., 2016.
%     "Metallic nickel hollow fiber membranes for hydrogen separation at
%     high temperatures," Journal of Membrane Science, 509, pp. 156-163.

p_in = 0.01:.01:3;          % varying H2 inlet partial pressure
for para = 1:length(p_in)
% geometry
d1o = 26.67*10^-3;          % inner wall outer diameter, m
d1i = 20.93*10^-3;          % inner wall inner diameter, m
t = (d1o-d1i)/2;            % inner tube wall thickness, m
height = 18*0.0354;         % mass transfer length, m
A1 = 3.14*d1i^2/4;          % tube side cross section area, m^2
d2i = .01;                  % outer tube inner diameter, m
A2 = pi/4*(d2i^2-d1o^2);    % shell side cross section area, m^2
R = 8.314;                  % ideal gas constant
T = 800+273.15;             % initial value of salt temperature, K
Pw = 1.44*10^(-6)*exp(-51070/(R*T));
% mol/(m*s*Pa^0.5), permeability of H2 of wall, Ni;

% tube side, sweep gas, N2
vfr1 = 30*10^-6/60;      % 30 mL/min
u1 = vfr1/A1;
n1 = 101000/R/T*vfr1;    % mass flow rate in [mol/s]
mfr1 = n1*28*10^-3;      % purging gas is N2
rho1 = mfr1/vfr1;        % tube side gas density
p1i = 0;                 % tube side inlet H2 partial pressure
c1i = 0;                 % tube side inlet H2 concentration
mu1 = 3.1335*10^-5;      % viscosity, Pa-s
Re1 = rho1*u1*d1i/mu1;   % Reynolds number
DN2 = 1.539*10^-6*T^1.548/log(T/3.16/10^-7)^2/exp(1067/T^2-2.8/T)/101000;
% H2 diffusivity in tube side fluid
HN2 = 1/R/T;             % solubility of H2 in tube side fluid
```

```
% shell side, feed gas, H2+CO2
vfr2 = 30*10^(-6)/60;                % volumetric flow rate, 30 mL/min
n2 = p_in(para)*101000/R/T*vfr2;     % number of moles of H2
mfr2 = n2*2*10^-3+n2*44*10^-3;       % kg/s, H2+CO2
rho2 = mfr2/vfr2;                    % shell side fluid density
u2 = vfr2/A2;                        % shell side fluid velocity
p2i = p_in(para)*101000;             % shell side inlet H2 partial pressure
mu2 = .5*(1.49+3)*10^-5;             % viscosity, Pa-s, 50%H2+50%CO2
Diam2 = 4*A2/(pi*d2i+pi*d1o);        % shell side hydraulics diameter
Re2 = rho2*u2*Diam2/mu2;             % shell side Reynolds number
DCO2 = 3.14*10^-5*T^1.75/exp(11.7/T)/(p2i*2);   % H2 diffusivity
HCO2 = 1/R/T;                        % H2 solubility
c2i = p2i*HCO2;                      % H2 inlet concentration

%% Sherwood number calculation
Sc2 = mu2/rho2/DCO2;
if Re2 > 1000 && Re2 < 20000
    C = .4; m = .6;
elseif Re2 > 20000
    C = .022; m = .84;
else
    C = 0; m = 0;
end
Sh2 = C*Re2^m*Sc2^.36;
if Sh2 == 0
    Sh2 = 3.41;
end
Sc1 = mu1/rho1/DN2;
if Re1 > 1000 && Re1 < 20000
    C = .4; m = .6;
elseif Re1 > 20000
    C = .022; m = .84;
else
    C = 0; m = 0;
end
Sh1 = C*Re1^m*Sc1^.36;
if Sh1 == 0
    Sh1 = 3.41;
end

%% mass transfer coefficients calculation
% shell side
R2 = Diam2/(DCO2*Sh2);       % resistance of shell side
h2 = Sh2*DCO2/Diam2;         % mass transfer coefficient
h2p = h2*HCO2;
h2pA = h2p*(d1o*pi*height);
% tube side
R1 = d1o/(DN2*Sh2);          % resistance of 2nd side
h1 = Sh1*DN2/d1i;
h1p = h1*HN2;
h1pA = h1p*(d1i*pi*height);
% Mass transfer area
Amt = 3.14*height*(d1o-d1i)/log(d1o/d1i);

%% iteration
% initialization, assume Q
```

```
Qnew = 10^-10;
err = 1;
i = 0;
while err > 10^-3
    Q = Qnew;
    c1i = 0;
    p1i = c1i/HN2;
    c2o = c2i-Q/vfr2;
    if c2o < 0
        Q = rand*((c2i-c1i*HCO2/HN2)/(1/vfr2+1/vfr1*HCO2/HN2));
        c2o = c2i-Q/vfr2;
    end
    c1o = c1i+Q/vfr1;
    p1o = c1o/HN2;
    p2o = c2o/HCO2;
    dp1 = p2i^.5-p1i^.5;
    dp2 = p2o^.5-p1o^.5;      % cocurrent flow configuration
    while dp2 < 0
        Q = rand*((c2i-c1i)/(1/vfr2+1/vfr1));
        c2o = c2i-Q/vfr2;
        c1o = c1i+Q/vfr1;
        p1o = c1o/HN2;
        p2o = c2o/HCO2;
        dp2 = p2o^.5-p1o^.5;
    end
    LMSPD = (dp1-dp2)/log(dp1/dp2);     % calculate LMSPD
    p2_avg = (p2i+p2o)/2-Q/h2pA;
    p1_avg = p2_avg+Q/h2pA-LMSPD+Q/h1pA;
    h2p = h2*HCO2*((p2_avg+Q/h2pA)^.5+(p2_avg)^.5);
    h2pA = h2p*(d1o*pi*height);
    h1p = h1*HN2*((p1_avg-Q/h1pA)^.5+(p1_avg)^.5);
    h1pA = h1p*(d1i*pi*height);
    hwp = Pw/t/(p1_avg^.5+p2_avg^.5);
    hwpA = hwp*t*(1/log(d1o/d1i))*(2*pi*height);
    hp = 1/(1/h1pA+1/h2pA+1/hwpA)/((d1o-d1i)/log(d1o/d1i));
    % overall mass transfer coefficient
    Qnew = LMSPD*hp/(log(d1o/d1i)/(2*pi*height));     % new mass flux
    err = abs((Qnew-Q)/Qnew);
    i = i+1;
end

%% output
c_IHX = c1o;                          % outlet H2 concentration
delta_c_IHX = c2i-c_IHX;              % amount removed

c1inwrite(para) = c2i;
c1outwrite(para) = c1o;
p1outwrite(para) = p1o;
c2outwrite(para) = c2o;
p2outwrite(para) = p2o;
LMSPDwrite(para) = LMSPD;
hpwrite(para) = hp;
Jwrite(para) = Qnew/Amt;
Qwrite(para) = Qnew;
deltap(para) = (p2_avg/101000)^.5-(p1_avg/101000)^.5;
dp1write(para) = (p2i/101000)^.5-(p1i/101000)^.5;
```

```
h1pwrite(para) = h1p;
h2pwrite(para) = h2p;
hwpwrite(para) = hwp;
end
```

Appendix B

Python code for parametric study in dose assessment

The following code is used to generate hourly meteorological files for GENII input. In this study, it is used in the parametric study of the dose assessment. An original hourly meteorological file (accessible on EPA website) is read into the program, and each meteorological parameter can be adjusted as necessary.

```
from __future__ import division
import numpy as np
import matplotlib.pyplot as plt
import itertools as IT
import re
import csv
import random

def load_data(filename):
      i = 0
      data = []
      day_summary = []
      with open(filename, 'r') as f:
            for line in f:
                  if i%25 != 0:
                        data.append(line.split())
                  else:
                        day_summary.append(line.split())
                  i += 1
      data = np.asarray(data, dtype = 'object')
      # day_summary = np.array(day_summary, dtype = 'object')
      return data, day_summary

def columns(data):
      date = data[:, 0]
      hour = data[:, 1]
      Ra = data[:, 2]
      Ra_normal = data[:, 3]
      Rs = data[:, 4]
      Rs_normal = data[:, 5]
      Ra_diffuse = data[:, 6]
      sky_cover_total = data[:, 7]
      sky_cover_opaque = data[:, 8]
      temp = data[:, 9]
```

```
	dew = data[:, 10]
	humidity_rel = data[:, 11]
	pres = data[:, 12]
	wind_dir = data[:, 13]
	wind_sp = data[:, 14]
	vis = data[:, 15]
	ceiling = data[:, 16]
	obser = data[:, 17]
	weather_pre = data[:, 18]
	preci = data[:, 19]
	aerosol = data[:, 20]
	snow_depth = data[:, 21]
	snow_interval = data[:, 22]
	preci_hourly = data[:, 23]
	# eto = data[:, 24]
	# ep = data[:, 25]
	return date, clean(hour), clean(temp), \
	clean(wind_dir), clean(wind_sp), \
	list(map(lambda x: x*1.94384, clean(wind_sp))), \
	list(map(lambda x: x*3.28, clean(ceiling))), \
	clean(sky_cover_total), clean(humidity_rel), \
	list(map(lambda x: x*10, clean(preci_hourly)))

def clean(parameter):
	new = []
	for entry in parameter:
		new.append(float(re.sub("[AESTUZ]", "", entry)))
	parameter = new
	return parameter

def net_radiation_index(cloud_cover, ceiling, hour, solar, preci):
	if preci < 0:
		preci = 0
	if cloud_cover == 10 and ceiling <= 7000:
		net_ra = 0
	# night time assumed as 18-6
	elif hour < 6 or hour > 18:
		if preci > 0:
			net_ra = 0
		elif cloud_cover < 4:
			net_ra = -2
		else:
			net_ra = -1
	# daytime
	else:
		# solar angle
		if solar <= 15:
			net_ra = 1
		elif solar <= 35:
			net_ra = 2
		elif solar <= 60:
			net_ra = 3
		else:
			net_ra = 4
		# modification
		if cloud_cover > 5 and preci == 0:
```

```
                  if ceiling <= 7000:
                        net_ra -= 2
                  elif ceiling <= 16000:
                        net_ra -= 1

                  if cloud_cover == 10:
                        net_ra -= 1

                  if net_ra < 1:
                        net_ra = 1

            elif preci > 0:
                  net_ra -= 2
                  if net_ra < 0:
                        net_ra = 0
      return net_ra

def solar_angle(latti, hour, day):
# calculate solar angle
      decli_angle = -23.5*np.cos(np.pi*day/173)
      h_a = 180-hour/12*180
      solar= np.arcsin(np.sin(latti) * np.sin(decli_angle) + np.cos(latti) *
np.cos(decli_angle) * np.cos(h_a))
      return solar

def stability(net_ra, wind_sp):
# calculate stability class
      # print(net_ra, wind_sp)
      if net_ra == 4:
            if wind_sp < 5.5: # knots
                  sta_class = 1
            elif wind_sp < 9.5:
                  sta_class = 2
            else:
                  sta_class = 3
      elif net_ra == 3:
            if wind_sp < 1.5: # knots
                  sta_class = 1
            elif wind_sp < 7.5:
                  sta_class = 2
            elif wind_sp < 11.5:
                  sta_class = 3
            else:
                  sta_class = 4
      elif net_ra == 2:
            if wind_sp < 3.5: # knots
                  sta_class = 2
            elif wind_sp < 9.5:
                  sta_class = 3
            else:
                  sta_class = 4
      elif net_ra == 1:
            if wind_sp < 3.5: # knots
                  sta_class = 3
            else:
                  sta_class = 4
```

```
	elif net_ra == 0:
		sta_class = 4
	elif net_ra == -1:
		if wind_sp < 3.5: # knots
			sta_class = 6
		elif wind_sp < 6.5:
			sta_class = 5
		else:
			sta_class = 4
	elif net_ra == -2:
		if wind_sp < 3.5: # knots
			sta_class = 7
		elif wind_sp < 6.5:
			sta_class = 6
		elif wind_sp < 10.5:
			sta_class = 5
		else:
			sta_class = 4
	return sta_class

def plot(dictionary):
	for key, values in dictionary.items():
		plt.plot(values)
		plt.title('{0}'.format(key))
		plt.show()
	return

def variation(parameter):
	year_average = np.average(parameter)
	maximum = np.amax(parameter)
	minimum = np.amin(parameter)
	day_average = []
	for i in range(int(len(parameter)/24)): # number of days
		day_data = parameter[(i*24):((i+1)*24)]
		# print(day_data)
		day_average.append(np.average(day_data))
	return day_average, year_average, maximum, minimum

def change_temp(dry_bulb, RH):
	a = 6.1121 # mb
	b = 18.678
	c = 257.14 # degC
	d = 234.5 # degC
	dew_point = []
	for i in range(len(dry_bulb)):
		gamma = np.log(RH[i]/100)+b*dry_bulb[i]/(c+dry_bulb[i])
		dew_point.append(c*gamma/(b-gamma))
	return dew_point

def write_met_temp(data, day_summary, temperature, RH):
	for i in range(len(temperature)):
		temperature[i] = temperature[i]+2.64
	dew_point = change_temp(temperature, RH)
	with open('add_2.h90', 'w') as f:
		for i in range(len(data)+len(day_summary)):
			if i == 0:
```

```
                        f.write(' 24243 Yakima                          WA  +8
N  46 34  W 120 32   324   2002-07-02 16:28:53\n')
                  elif i%25 == 0:
                        j = int(np.floor(i/25))
                        k = day_summary[j]
                        # f.write(' {0:10s}\n'.format(day_summary[j][0]))
                        f.write('{0:>11s}{1:>3s}{2:>7s}{3:>7s}{4:>7s}
{5:>7s}  {6:>7s}
{7:>4s}{8:>4s}{9:>7s}{10:>7s}{11:>5s}{12:>7s}{13:>5s}{14:>7s}{15:>8s}{16:>8s}
{17:>3s}{18:>11s}{19:>5s}{20:>8s}{21:>6s}{22:>5s}{23:>8s}{24:>9s}{25:>8s}\n'\
                              .format(k[0], k[1], k[2], k[3], k[4], k[5],
k[6], k[7], k[8], k[9], \
                                    k[10], k[11], k[12], k[13], k[14], k[15],
k[16], k[17], k[18], k[19], \
                                    k[20], k[21], k[22], k[23], k[24],
k[25]))
                  else:
                        j = int(i-1-np.floor(i/25))
                        k = data[j]
                        k[9] = temperature[j]
                        k[10] = dew_point[j]

      f.write('{0:>11s}{1:>3s}{2:>7s}{3:>7s}{4:>9s}{5:>9s}{6:>9s}{7:>4s}{8:>4
s}{9:>6.1f}S{10:>6.1f}S{11:>5s}{12:>7s}{13:>5s}{14:>7s}{15:>8s}{16:>8s}{17:>3
s}{18:>11s}{19:>5s}{20:>8s}{21:>6s}{22:>5s}{23:>8s}\n'\
                              .format(k[0], k[1], k[2], k[3], k[4], k[5],
k[6], k[7], k[8], k[9], \
                                    k[10], k[11], k[12], k[13], k[14], k[15],
k[16], k[17], k[18], k[19], \
                                    k[20], k[21], k[22], k[23]))
      return

def write_met_preci(data, day_summary, precipitation):
      no_preci = []
      values = []
      for i in range(len(precipitation)):
            # precipitation[i] = precipitation[i]*5
            if precipitation[i] == 0:
                  no_preci.append(i)
            else:
                  values.append(precipitation[i])
      to_change = random.sample(no_preci, 2*len(values))
      # print(to_change)
      for i in range(len(values)):
            precipitation[to_change[i]] = values[i]
            precipitation[to_change[i+len(values)]] = values[i]

      with open('fake.h90', 'w') as f:
            for i in range(len(data)+len(day_summary)):
                  if i == 0:
                        f.write(' 24243 Yakima                          WA  +8
N  46 34  W 120 32   324   2002-07-02 16:28:53\n')
                  elif i%25 == 0:
                        j = int(np.floor(i/25))
                        k = day_summary[j]
```

```
                        f.write('{0:>11s}{1:>3s}{2:>7s}{3:>7s}{4:>7s}
{5:>7s}  {6:>7s}
{7:>4s}{8:>4s}{9:>7s}{10:>7s}{11:>5s}{12:>7s}{13:>5s}{14:>7s}{15:>8s}{16:>8s}
{17:>3s}{18:>11s}{19:>5s}{20:>8s}{21:>6s}{22:>5s}{23:>8s}{24:>9s}{25:>8s}\n'\
                                .format(k[0], k[1], k[2], k[3], k[4], k[5],
k[6], k[7], k[8], k[9], \
                                        k[10], k[11], k[12], k[13], k[14], k[15],
k[16], k[17], k[18], k[19], \
                                        k[20], k[21], k[22], k[23], k[24],
k[25]))
                  else:
                        j = int(i-1-np.floor(i/25))
                        k = data[j]
                        k[23] = precipitation[j]

      f.write('{0:>11s}{1:>3s}{2:>7s}{3:>7s}{4:>9s}{5:>9s}{6:>9s}{7:>4s}{8:>4
s}{9:>7s}{10:>7s}{11:>5s}{12:>7s}{13:>5s}{14:>7s}{15:>8s}{16:>8s}{17:>3s}{18:
>11s}{19:>5s}{20:>8s}{21:>6s}{22:>5s}{23:>7.2f}S\n'\
                                .format(k[0], k[1], k[2], k[3], k[4], k[5],
k[6], k[7], k[8], k[9], \
                                        k[10], k[11], k[12], k[13], k[14], k[15],
k[16], k[17], k[18], k[19], \
                                        k[20], k[21], k[22], k[23]))
      return

def write_met_windsp(data, day_summary, wind_sp):
      for i in range(len(wind_sp)):
            wind_sp[i] = wind_sp[i]*0.948815
      with open('add_22.h90', 'w') as f:
            for i in range(len(data)+len(day_summary)):
                  if i == 0:
                        f.write(' 24243 Yakima                              WA  +8
N  46 34  W 120 32   324   2002-07-02 16:28:53\n')
                  elif i%25 == 0:
                        j = int(np.floor(i/25))
                        k = day_summary[j]
                        # f.write(' {0:10s}\n'.format(day_summary[j][0]))
                        f.write('{0:>11s}{1:>3s}{2:>7s}{3:>7s}{4:>7s}
{5:>7s}  {6:>7s}
{7:>4s}{8:>4s}{9:>7s}{10:>7s}{11:>5s}{12:>7s}{13:>5s}{14:>7s}{15:>8s}{16:>8s}
{17:>3s}{18:>11s}{19:>5s}{20:>8s}{21:>6s}{22:>5s}{23:>8s}{24:>9s}{25:>8s}\n'\
                                .format(k[0], k[1], k[2], k[3], k[4], k[5],
k[6], k[7], k[8], k[9], \
                                        k[10], k[11], k[12], k[13], k[14], k[15],
k[16], k[17], k[18], k[19], \
                                        k[20], k[21], k[22], k[23], k[24],
k[25]))
                  else:
                        j = int(i-1-np.floor(i/25))
                        k = data[j]
                        k[14] = wind_sp[j]

      f.write('{0:>11s}{1:>3s}{2:>7s}{3:>7s}{4:>9s}{5:>9s}{6:>9s}{7:>4s}{8:>4
s}{9:>7s}{10:>7s}{11:>5s}{12:>7s}{13:>5s}{14:>6.1f}S{15:>8s}{16:>8s}{17:>3s}{
18:>11s}{19:>5s}{20:>8s}{21:>6s}{22:>5s}{23:>8s}\n'\
```

```
                              .format(k[0], k[1], k[2], k[3], k[4], k[5],
k[6], k[7], k[8], k[9], \
                                    k[10], k[11], k[12], k[13], k[14], k[15],
k[16], k[17], k[18], k[19], \
                                    k[20], k[21], k[22], k[23]))
      return

def write_met_wind_dir(data, day_summary, wind_dir):
      for i in range(len(wind_dir)):
            wind_dir[i] = wind_dir[i]+180
            if wind_dir[i] >= 360:
                  wind_dir[i] -= 360
      with open('fake.h90', 'w') as f:
            for i in range(len(data)+len(day_summary)):
                  if i == 0:
                        f.write(' 24243 Yakima                          WA  +8
N  46 34  W 120 32   324   2002-07-02 16:28:53\n')
                  elif i%25 == 0:
                        j = int(np.floor(i/25))
                        k = day_summary[j]
                        # f.write(' {0:10s}\n'.format(day_summary[j][0]))
                        f.write('{0:>11s}{1:>3s}{2:>7s}{3:>7s}{4:>7s}
{5:>7s}  {6:>7s}
{7:>4s}{8:>4s}{9:>7s}{10:>7s}{11:>5s}{12:>7s}{13:>5s}{14:>7s}{15:>8s}{16:>8s}
{17:>3s}{18:>11s}{19:>5s}{20:>8s}{21:>6s}{22:>5s}{23:>8s}{24:>9s}{25:>8s}\n'\
                              .format(k[0], k[1], k[2], k[3], k[4], k[5],
k[6], k[7], k[8], k[9], \
                                    k[10], k[11], k[12], k[13], k[14], k[15],
k[16], k[17], k[18], k[19], \
                                    k[20], k[21], k[22], k[23], k[24],
k[25]))
                  else:
                        j = int(i-1-np.floor(i/25))
                        k = data[j]
                        k[13] = int(wind_dir[j])

      f.write('{0:>11s}{1:>3s}{2:>7s}{3:>7s}{4:>9s}{5:>9s}{6:>9s}{7:>4s}{8:>4
s}{9:>7s}{10:>7s}{11:>5s}{12:>7s}{13:>4d}S{14:>6s}{15:>8s}{16:>8s}{17:>3s}{18
:>11s}{19:>5s}{20:>8s}{21:>6s}{22:>5s}{23:>8s}\n'\
                              .format(k[0], k[1], k[2], k[3], k[4], k[5],
k[6], k[7], k[8], k[9], \
                                    k[10], k[11], k[12], k[13], k[14], k[15],
k[16], k[17], k[18], k[19], \
                                    k[20], k[21], k[22], k[23]))
      return

def write_met_RH(data, day_summary, temperature, RH):
      for i in range(len(RH)):
            RH[i] = int(RH[i]*2)
            if RH[i] > 100:
                  RH[i] = 100
      dew_point = change_temp(temperature, RH)
      with open('fake.h90', 'w') as f:
            for i in range(len(data)+len(day_summary)):
                  if i == 0:
```

```
                        f.write(' 24243 Yakima                          WA  +8
N  46 34  W 120 32   324   2002-07-02 16:28:53\n')
                  elif i%25 == 0:
                        j = int(np.floor(i/25))
                        k = day_summary[j]
                        # f.write(' {0:10s}\n'.format(day_summary[j][0]))
                        f.write('{0:>11s}{1:>3s}{2:>7s}{3:>7s}{4:>7s}
{5:>7s}  {6:>7s}
{7:>4s}{8:>4s}{9:>7s}{10:>7s}{11:>5s}{12:>7s}{13:>5s}{14:>7s}{15:>8s}{16:>8s}
{17:>3s}{18:>11s}{19:>5s}{20:>8s}{21:>6s}{22:>5s}{23:>8s}{24:>9s}{25:>8s}\n'\
                              .format(k[0], k[1], k[2], k[3], k[4], k[5],
k[6], k[7], k[8], k[9], \
                                    k[10], k[11], k[12], k[13], k[14], k[15],
k[16], k[17], k[18], k[19], \
                                    k[20], k[21], k[22], k[23], k[24],
k[25]))
                  else:
                        j = int(i-1-np.floor(i/25))
                        k = data[j]
                        k[11] = RH[j]
                        k[10] = dew_point[j]

      f.write('{0:>11s}{1:>3s}{2:>7s}{3:>7s}{4:>9s}{5:>9s}{6:>9s}{7:>4s}{8:>4
s}{9:>7s}{10:>6.1f}S{11:>4d}S{12:>7s}{13:>5s}{14:>7s}{15:>8s}{16:>8s}{17:>3s}
{18:>11s}{19:>5s}{20:>8s}{21:>6s}{22:>5s}{23:>8s}\n'\
                              .format(k[0], k[1], k[2], k[3], k[4], k[5],
k[6], k[7], k[8], k[9], \
                                    k[10], k[11], k[12], k[13], k[14], k[15],
k[16], k[17], k[18], k[19], \
                                    k[20], k[21], k[22], k[23]))
      return

def GENII(filename, date, hour, sta_class, wind_dir, wind_sp, temperature,
ceiling, preci):
      year = []
      month = []
      day = []
      preci_code = []
      for i in range(len(date)):
            # adjusting parameter
            temperature[i] = (temperature[i]+273.15)*1.068526676
            year.append(int(date[i].split('-')[0])%100)
            month.append(int(date[i].split('-')[1]))
            day.append(int(date[i].split('-')[2]))
            ceiling[i] = int(np.floor(ceiling[i]/3.281))
            if preci[i] <= 1:
                  preci_code.append(0)
            elif preci[i] <= 5:
                  preci_code.append(1)
            elif preci[i] <= 10:
                  preci_code.append(2)
            else:
                  preci_code.append(3)
            # elif preci <=
      f = open(filename, 'w')
      for i in range(len(date)):
```

```
            f.write('{0:5d}{1:3d}{2:3d}{3:3d}{4:2d}{5:5d}.{6:6.1f}
{7:.2f}{8:6d}.{9:2d}{10:7.2f}     1.\n'\
                  .format(year[i], month[i], day[i], int(hour[i]),
int(sta_class[i]), \
                        int(wind_dir[i]), wind_sp[i], temperature[i],
ceiling[i], \
                        preci_code[i], preci[i]))
      f.close()
      return

def main():
      data, day_summary = load_data('add_2.h90')
      # print(day_summary[1][0])
      latti = 46.55 # site lattitude
      # precipitation rate [mm/hr]
      date, hour, temp, wind_dir, wind_sp, wind_sp_knot, \
      ceiling, sky_cover_total, humidity_rel, preci = columns(data)
      # print(sum(preci)/len(preci))
      solar = []
      net_ra = []
      sta_class = []
      for i in range(len(temp)):
            solar.append(solar_angle(latti, hour[i], i+1))
            net_ra.append(net_radiation_index(sky_cover_total[i], ceiling[i],
hour[i], solar[i], preci[i]))
            sta_class.append(stability(net_ra[i], wind_sp_knot[i]))
            i += 1

      dictionary = {
                  "temperature": temp,
                  "temp_day_average": variation(temp),
                  "wind speed": wind_sp,
                  "wind_sp_day_average": variation(wind_sp),
                  "humidity_relative": humidity_rel,
                  "humidity_rel_day_average": variation(humidity_rel),
                  "hourly precipitation": preci,
                  "stability class": sta_class
                  }

      # # change temperature
      # write_met_temp(data, day_summary, temp, humidity_rel)
      # # change precipitation
      # write_met_preci(data, day_summary, preci)
      ## change wind speed
      #write_met_windsp(data, day_summary, wind_sp)
      # # change relative humidity
      # write_met_RH(data, day_summary, temp, humidity_rel)
      # # change wind direction
      # write_met_wind_dir(data, day_summary, wind_dir)

      # write single year data
      # with open('90.csv', 'w') as f:
      #     [f.write('{0}, {1}\n'.format(key, values)) for key, values in
dictionary.items()]

      # # write GENII input file
```

```
      # GENII('try.met', date, hour, sta_class, wind_dir, wind_sp, temp,
ceiling, preci)
      return

if __name__ == '__main__':
      main()
```

Appendix C

Code for uncertainty analysis in dose assessment

This code is used to train the Gaussian Process in the uncertainty analysis. Samples with the corresponding output are read into the program, and a model is trained to predict the output if a set of new input parameters are feed to the model. The methodology is described in Section 2.2.3.

```
hanford = csvread('hanford_2020_110m.csv');
inl = csvread('inl_2020_110m.csv');
ornl = csvread('ornl_2020_110m.csv');

%% Guassian process training, run this part first to generate
% GP_surrogates.mat
% hanford_GP =  fitrgp(hanford(:,1:3),
hanford(:,4),'KernelFunction','matern52',...
%     'FitMethod','exact','PredictMethod','exact','Standardize',1,...
%     'OptimizeHyperparameters','all','HyperparameterOptimizationOptions',...
%     struct('MaxObjectiveEvaluations',25, 'KFold',5));
%
% ornl_GP =  fitrgp(ornl(:,1:3), ornl(:,4),'KernelFunction','matern52',...
%     'FitMethod','exact','PredictMethod','exact','Standardize',1,...
%     'OptimizeHyperparameters','all','HyperparameterOptimizationOptions',...
%     struct('MaxObjectiveEvaluations',25, 'KFold',5));
%
% inl_GP =  fitrgp(inl(:,1:3), inl(:,4),'KernelFunction','matern52',...
%     'FitMethod','exact','PredictMethod','exact','Standardize',1,...
%     'OptimizeHyperparameters','all','HyperparameterOptimizationOptions',...
%     struct('MaxObjectiveEvaluations',25, 'KFold',5));

%% after Gaussian process training
load GP_surrogates.mat

hanford_T = 10.822 + rand(1e5,1)*(13.028 - 10.822);
hanford_W = normrnd(2.696, 0.274, [1e5,1]);
hanford_H = normrnd(60.3125, 2.7237, [1e5,1]);
dose_hanford = predict(hanford_GP,[hanford_T, hanford_W, hanford_H]).*10;
% mSv

inl_T = 8.494 + rand(1e5,1)*(9.535 - 8.494);
inl_W = normrnd(4.537, 0.4086, [1e5,1]);
inl_H = normrnd(57.69, 3.0895, [1e5,1]);
```

```
dose_inl = predict(inl_GP,[inl_T, inl_W, inl_H]).*10; % mSv

ornl_T = 15.437 + rand(1e5,1)*(17.059 - 15.437);
ornl_W = normrnd(3.1289, 0.30534, [1e5,1]);
ornl_H = normrnd(71.53, 2.303, [1e5,1]);
dose_ornl = predict(ornl_GP,[ornl_T, ornl_W, ornl_H]).*10;  % mSv

% figure()
% histogram(dose_hanford,5000,'Normalization','probability');
% % yticklabels(yticks*100)
% xlabel('Max. individual dose [rem]')
% ylabel('Probability')
% % title('Hanford site prediction of 2020')
% % title('hanford, wind speed=3.2')
% hold off

figure('DefaultAxesFontSize',18)
edges=linspace(.2,.7,51);
% pick number of bins, points is 1+ that over your range
N = histcounts(dose_hanford,edges); % get the counts in those bins
N = N./(1e5);
x=filter([0.5 0.5],1,edges);        % midpoint of bins; mean of edges
plot(x(2:end),N, 'LineWidth',2)
% and plot...N.B. start with second x to get number bins wanted
line([.4 .4],[0 0.12], 'Color', 'red', 'LineWidth',2)
xlabel('Max. individual dose [mSv]','FontSize', 18)
ylabel('Probability','FontSize', 18)
title('Hanford site prediction of 2020')
txt = '\leftarrow regulatory limit';
text(.4, 0.115,txt,'FontSize', 18)
hold off
title('hanford, wind speed=3.2')

% figure()
% histogram(dose_inl,50,'Normalization','probability');
% % yticklabels(yticks*100)
% xlabel('Max. individual dose [rem]')
% ylabel('Probability')
% title('INL site prediction of 2020')
% hold off

figure('DefaultAxesFontSize',18)
edges=linspace(.28, .49,51);
% pick number of bins, points is 1+ that over your range
N = histcounts(dose_inl,edges);  % get the counts in those bins
N = N./(1e5);
x=filter([0.5 0.5],1,edges);     % midpoint of bins; mean of edges
plot(x(2:end),N,'LineWidth',2)
% and plot...N.B. start with second x to get number bins wanted
line([0.4 0.4],[0 0.09], 'Color', 'red', 'LineWidth',2)
xlabel('Max. individual dose [mSv]','FontSize', 18)
ylim([0 0.09])
ylabel('Probability','FontSize', 18)
title('Idaho Falls site prediction of 2020')
txt = 'regulatory limit \rightarrow';
```

```
text(0.285, 0.0875,txt,'FontSize', 18)
hold off

% figure()
% histogram(dose_ornl,50,'Normalization','probability');
% % yticklabels(yticks*100)
% xlabel('Max. individual dose [rem]')
% ylabel('Probability')
% title('ORNL site prediction of 2020')
% hold off

figure('DefaultAxesFontSize',18)
edges=linspace(0.21,0.31,51);
% pick number of bins, points is 1+ that over your range
N = histcounts(dose_ornl,edges); % get the counts in those bins
N = N./(1e5);
x=filter([0.5 0.5],1,edges);     % midpoint of bins; mean of edges
plot(x(2:end),N,'LineWidth',2)
% and plot...N.B. start with second x to get number bins wanted
line([0.4 0.4],[0 0.08], 'Color', 'red', 'LineWidth',2)
xlim([0.2 0.42])
xlabel('Max. individual dose [mSv]','FontSize', 18)
ylabel('Probability','FontSize', 18)
title('Oak Ridge site prediction of 2020')
txt = 'regulatory limit \rightarrow';
text(0.3, 0.07,txt,'FontSize', 18)
hold off

%% cdf plots
% figure()
% cdfplot(dose_hanford)
% hold off
% figure()
% cdfplot(dose_inl)
% hold off
% figure()
% cdfplot(dose_ornl)
% hold off
```

Sobol indices

This code is used to perform the sensitivity study of input variables using the Sobol indices method. The methodology is described in Section 2.2.3.

```
%% 1 - INITIALIZE THE UQLAB FRAMEWORK AND CLEAR THE WORKSPACE
%  Clear variables from the workspace and reinitialize the UQLab framework
clearvars;
uqlab;

%% 2 - MODEL
```

```
%  COMPUTATIONAL MODEL
% Create a model object that uses the uq_SimplySupportedBeam9points function:
Model.mFile = 'dose_hanford'; % specify the function name
myModel = uq_createModel(Model);
% create and add the model to UQLab

%% 3 - PROBABILISTIC INPUT MODEL

Input.Marginals(1).Name = 'T';
Input.Marginals(1).Type = 'Uniform';
Input.Marginals(1).Parameters = [10.822, 13.028]; % (m)

Input.Marginals(2).Name = 'wind';
Input.Marginals(2).Type = 'Gaussian';
Input.Marginals(2).Parameters = [2.696, 0.274]; % (m)

Input.Marginals(3).Name = 'humidity';
Input.Marginals(3).Type = 'Gaussian';
Input.Marginals(3).Parameters = [60.726, 2.737]; % (m)

myInput = uq_createInput(Input);
uq_display(myInput);

%% 4 - SENSITIVITY ANALYSIS
% `Sensitivity analysis is performed by calculating the Sobol' indices for
% each of the output components separately.

SobolOpts.Type = 'Sensitivity';
SobolOpts.Method = 'Sobol';
% SobolOpts.Sampling = 'lhs';
SobolOpts.Sobol.Order = 1;
SobolOpts.Sobol.SampleSize = 1e5;
mySobolAnalysisMC = uq_createAnalysis(SobolOpts);
mySobolResultsMC = mySobolAnalysisMC.Results;
```

Appendix D

Publications

Peer-reviewed Journal Articles

X. Wu, Y. Liu, K. Kearfott, and X. Sun, "Study on the health impact of tritium release from FHRs to the public," to be submitted to Science of the Total Environment.

X. Wu, S. Shi, S. Zhang, D. Arcilesi, R. Christensen, P. Sabharwall and X. Sun, "Mass transport analysis for tritium removal in FHRs," *Annals of Nuclear Energy* **121**, pp. 250-259, 2018.

S. Zhang, **X. Wu**, S. Shi, X. Sun, R. Christensen, and G. Yoder, "A coupled heat transfer and tritium mass transport model for a double-wall heat exchanger design for FHRs," *Annals of Nuclear Energy* **122**, pp. 328-339, 2018.

Conference Proceedings

X. Wu, W. Chan, S. Shi, X. Sun and R. Christensen, "Computational simulation of hydrogen permeation experiment," *Proceedings of the 2018 26th International Conference on Nuclear Engineering*, ICONE26, July 22–26, 2018, London, UK.

S. Zhang, S. Shi, **X. Wu**, X. Sun and R. Christensen, "Double-wall natural draft heat exchanger design for tritium control in FHRs," *Proceedings of the 2017 25th International Conference on Nuclear Engineering*, ICONE25, July 2–6, 2017, Shanghai, China.

X. Wu, S. Zhang, S. Shi, X. Sun, R. Christensen and P. Sabharwall, "Tritium release limit of FHRs," *Proceedings of ANS Winter Meeting 2016*, November 5–10, Las Vegas, NV.

X. Wu, D. Arcilesi, X. Sun, R. Christensen and P. Sahharwall, "Conceptual design of tritium removal facility for FHRs," *Proceedings of International Topical Meeting on Nuclear Reactor Thermal Hydraulics (NURETH-16),* August 30–September 4, 2015, Chicago, IL, pp. 4935-4938.

X. Wu, I.H. Kim, D. Arcilesi, X. Sun, R. Christensen and P. Sabharwall, "Computer simulation of tritium removal facility design," *Proceedings of the 10th International Topical Meeting on Nuclear Thermal Hydraulics, Operation and Safety (NUTHOS-10),* Okinawa, Japan, December 14–18, 2014, NUTHOS10-1204.

I.H. Kim, **X. Wu**, D. Arcilesi, X. Sun, R. Christensen and P. Sabharwall, "OSU tritium control and mitigation strategy for FHRs," *Proceedings of the 10th International Topical Meeting on Nuclear Thermal Hydraulics, Operation and Safety (NUTHOS-10),* Okinawa, Japan, December 14–18, 2014, NUTHOS10-1199.

Conference Presentations

X. Wu, D. Arcilesi, X. Sun, R. Christensen and P. Sabharwall, "Preliminary design of a tritium control system for fluoride salt-cooled high-temperature reactors," 11th International Conference on Tritium Science & Technology (Tritium 2016), Charleston, SC, April 17–22, 2016.

X. Wu, S. Zhang, S. Shi, X. Sun, R. Christensen and P. Sabharwall, "Tritium management options in FHRs," 2nd MSR Workshop, October 4–5, Oak Ridge National Laboratory, Oak Ridge, TN, poster presented by Dr. Xiaodong Sun.